Study of ultrashort laser-pulse induced ripples formed at the interface of silicon-dioxide on silicon

STUDY OF ULTRASHORT LASER-PULSE INDUCED RIPPLES FORMED AT THE INTERFACE OF SILICON-DIOXIDE ON SILICON

BY

BING LIU, B. Eng.

A THESIS

SUBMITTED TO THE DEPARTMENT OF ENGINEERING PHYSICS

AND THE SCHOOL OF GRADUATE STUDIES

OF MCMASTER UNIVERSITY

IN PARTIAL FULFILMENT OF THE REQUIREMENTS

FOR THE DEGREE OF

MASTER OF APPLIED SCIENCE

© Copyright by BING LIU, April 2013

All Rights Reserved

Master of Applied Science (2013) McMaster University
(Department of Engineering Physics) Hamilton, Ontario, Canada

TITLE: Study of ultrashort laser-pulse induced ripples formed at the interface of silicon-dioxide on silicon

AUTHOR: BING LIU
B. Eng., Engineering Physics
McMaster University, Hamilton, Ontario, Canada

SUPERVISOR: Professor Harold Haugen

NUMBER OF PAGES: xvi, 145

Abstract

In this thesis, the ripple formation at the interface of SiO_2 and Si were studied in a systematic fashion by irradiating the SiO_2-Si samples with ultrashort laser pulses under a broad variety of experimental conditions. They consist of different irradiating laser wavelengths, incident laser energies, translation speeds, translation directions, spot sizes of the laser beam, as well as oxide thicknesses. The ripples produced by laser irradiation are examined using various microscopy techniques in order to characterize their surface morphology, detailed structures, crystalline properties, and so on.

For the experiments carried out at $\lambda = 800$ nm, the ripples formed on the SiO_2-Si sample with an oxide thickness of 216 nm were first observed under optical microscopy and SEM. After removing the oxide layer with HF solution, the surface features of the ripples on the Si substrate were investigated using SEM and AFM techniques. Subsequently, by means of TEM and EDX analysis, the material composition and crystallinity of the ripples were determined. It is concluded that the ripples are composed of nano-crystalline silicon. In addition to the 216 nm oxide thickness, other oxide samples with different oxide thicknesses, such as 24, 112, 117, 158 and 1013 nm, were also processed under laser irradiation. The ripple formation as a function of the laser energy, the translation direction and the spot size is discussed in detail. Furthermore, the ripples created at the SiO_2-Si interface are compared with

the LIPSS created on pure silicon samples that were processed under similar laser irradiation conditions. The spatial periodicities of the ripples were evaluated to be in the range of between 510 nm and 700 nm, which vary with the oxide thickness and other laser parameters.

For the experiments using the $\lambda = 400$ nm laser pulses, it is found that ripples can also be formed at the SiO_2-Si interface, which have spatial periodicities in the range of between 310 nm and 350 nm depending on the oxide thickness. The ripple formation at this 400 nm wavelength as a function of the laser energy, the translation speed, and translation direction is considered as well. For the case of $\lambda = 400$ nm irradiation, a comparison is also made between the interface ripples on the SiO_2-Si samples and the LIPSS on a pure Si sample. Through FIB-TEM and EDX analysis, it confirmed that the ripples were produced in the substrate while the oxide layer maintained its structural integrity. In addition, the ripples are composed of nano-crystalline silicon whose crystallite sizes are on the order of a few nanometers.

Apart from irradiating oxide samples with femtosecond laser pulses, which applies to the two cases of $\lambda = 800$ and 400 nm mentioned above, oxide samples with an oxide thickness of 112 nm were irradiated with picosecond laser pulses at $\lambda = 800$ nm whose pulse durations are 1 ps and 5 ps, respectively. However, no regular ripples can be produced at the SiO_2-Si interface while maintaining the complete integrity of the oxide layer.

Acknowledgements

First of all, I would like to express my deepest gratitude to my supervisor, Professor Harold Haugen. In the last two years, he always offered me with his insightful guidance and thoughtful support regarding research work and other general aspects. I was tremendously inspired and influenced by his passion and dedication to academic research. I truly believe that his remarkable sense of responsibility toward his students will make everyone feel fortunate to have such a supervisor like him.

I would like to specially thank Dr. Eugene Hsu for teaching me everything that I know about operating the laser systems, using various lab equipment, as well as managing the lab. I was highly motivated by the strength and commitment that he demonstrated toward his work. His open-mindedness to embrace new challenges and willingness to help others had significant impact on my own character for the past two years.

Dr. John Preston and Dr. Andrew Knights are key contributors to my research by providing insightful scientific discussions and stimulating directions. The fellow researchers from their groups, including Dr. Jessica Carvalho, Dr. Edgar Huante Ceron and Dixon Paez also helped me with their technical expertise along the way.

I appreciated the technical training and assistance from the staff members in the Canadian Center for Electron Microscopy (CCEM). In particular, I would like

to thank Steve Koprich, Chris Butcher and Dr. Glynis de Silveira for helping me on optical microscopy and SEM. Moreover, I want to thank Dr. Gianluigi Botton, Julia Huang, Dr. Carmen Andrei and Dr. Andreas Korinek for their important contributions to the FIB-TEM work including sample preparation and subsequent imaging analysis.

When building the heating stages, Jim Garrett from the Department of Physics at McMaster provided me with a great deal of technical guidance from the start to the end. I also would like to thank Dr. Doris Stevanovic from the Centre for Emerging Device Technology for overseeing and training me on the HF etching procedure, as well as Peter Jonasson from the Department of Engineering Physics for growing the oxide samples.

I also would like to show my appreciation to my lab-mates for their valuable support and discussions, including Dr. Ran An, Hao Liu, Kevin Mortimer, as well as Sam Virtue who was a summer student. More importantly, their laughter and friendships made the lab a relaxing and agreeable working place.

Dr. Jörn Bonse who is a well-regarded researcher in the field is greatly appreciated for his constructive scientific discussions and on-going interests in our research.

Contents

Abstract **iii**

Acknowledgements **v**

1 Introduction **1**

1.1 Brief introduction to ultrashort laser pulses 1

1.2 Motivations of the research 3

1.3 Overview of the thesis 4

2 Background **6**

2.1 Brief overview of the physical interaction processes of ultrashort laser pulses with materials 6

2.1.1 Free carrier generation 6

2.1.2 Electronic thermalization 9

2.1.3 Phase transition and structural change from thermal effects . 10

2.2 LIPSS formation on bulk materials after ultrafast laser irradiation . . 12

2.2.1 Sipe and SPP theories for generation of the LSFL 12

2.2.2 SHG theory for generation of the HSFL 15

2.3 Literature review of the ultrashort laser pulse processing of SiO_2-Si samples . . . 17
2.3.1 Nanosecond regime . . . 17
2.3.2 Picosecond regime . . . 18
2.3.3 Femtosecond regime . . . 20

3 Experimental setup **23**
3.1 Ultrashort-pulse laser system . . . 23
3.1.1 Millennia Vs . . . 24
3.1.2 Evolution . . . 25
3.1.3 Tsunami . . . 26
3.1.4 Spitfire LCX . . . 27
3.2 Setup of the optical beam path . . . 29
3.3 Micromachining setup . . . 31
3.4 Diagnostic techniques of ultrafast laser pulses . . . 33
3.4.1 Average power . . . 34
3.4.2 Spatial intensity distribution . . . 35
3.4.3 Spectrum . . . 36
3.4.4 Pulse width . . . 36

4 Sample analysis techniques and parameter extraction **39**
4.1 Sample information and preparation . . . 39
4.1.1 Si samples . . . 39
4.1.2 SiO_2-Si samples and their growth conditions . . . 40
4.1.3 Inspection of sample surface . . . 42

4.2 Sample analysis techniques . . . 44
4.2.1 Ellipsometry . . . 44
4.2.2 Atomic force microscope (AFM) . . . 46
4.2.3 Optical microscope (OM) . . . 48
4.2.4 Scanning electron microscope (SEM) . . . 49
4.2.5 Transmission electron microscopy (TEM) and focused ion beam (FIB) technique . . . 50
4.3 Parameter extraction . . . 51
4.3.1 Extraction of incident laser spot size . . . 51
4.3.2 Extraction of the effective number of laser pulses in translational motion . . . 54

5 Results and discussion **55**
5.1 Laser irradiation using femtosecond pulses at 800 nm wavelength . . . 55
5.1.1 Experimental details . . . 55
5.1.2 Ripples formed at the SiO_2-Si interface . . . 56
5.1.3 Effects of oxide thickness . . . 72
5.1.4 Effects of laser energy . . . 76
5.1.5 Effects of cutting direction . . . 78
5.1.6 Effects of different spot size . . . 81
5.1.7 Comparative results of the ripples between the SiO_2-Si and Si samples at $\lambda = 800$ nm . . . 83
5.1.8 Additional results . . . 87
5.2 Laser irradiation using femtosecond pulses at 400 nm wavelength . . . 95
5.2.1 Experimental details . . . 95

5.2.2 The most well-structured ripples formed at the SiO_2-Si interface at $\lambda = 400$ nm . . . 97
5.2.3 Effects of incident laser energy . . . 107
5.2.4 Effects of translation speed . . . 109
5.2.5 Effects of cutting direction . . . 111
5.2.6 Comparative results of the ripples between the SiO_2-Si and Si samples at $\lambda = 400$ nm . . . 113
5.3 Laser irradiation using picosecond pulses at 800 nm wavelength . . . 116
5.3.1 Experimental details . . . 116
5.3.2 Results and discussion . . . 117

6 Summary and future work 121
6.1 Summary . . . 121
6.1.1 Laser irradiation conditions . . . 121
6.1.2 General material characterization of the ripples . . . 122
6.1.3 Effects of different irradiation conditions on the ripple formation 124
6.2 Suggestions for future work . . . 126
6.2.1 Extensive work on post-analysis of the irradiated oxide samples 126
6.2.2 Further exploration on the laser irradiation conditions . . . 126
6.2.3 Applications to various layered samples . . . 128
6.2.4 Theoretical study of the ripple formation for layered structures 128

A Academic contributions 130

List of Tables

1 Normal operating conditions of each laser system. 25

2 Growth conditions for the SiO_2-Si samples with different oxide thicknesses used in the experiments. 41

3 Thickness measurements of the SiO_2-Si samples based on the ellipsometry technique and the cross-sectional TEM images. 43

4 Summary of laser irradiation conditions for the SiO_2-Si samples with different oxide thicknesses. 72

5 Comparison of the spatial periodicity of the ripples for the SiO_2-Si samples with different oxide thicknesses. 75

6 Summary of the fixed experimental parameters employed in the laser experiments 122

7 Summary of the varying experimental parameters applied in the laser experiments to study their effects on the ripple formation. 123

List of Figures

1 Schematic representation of the physical interaction processes of ultra-short laser pulses with solid materials, and subsequent material response. 11

2 Schematic overview of the laser system used in the research. 24

3 Schematic diagram of the setup of the optical beam path. 30

4 Schematic diagram of the second-order non-collinear autocorrelator used to measure the pulse width of the ultrashort pulses laser in the experiments. 37

5 OM and SEM images of Si and SiO_2-Si samples taken prior to laser irradiation. 45

6 Plot of D^2 against the $\ln(E)$ for a typical single-shot D^2 measurement 53

7 Observation of the ripples on the SiO_2-Si sample with an intact 216 nm oxide layer. 57

8 SEM image of the ripples on the Si substrate after the oxide layer was removed using HF solution. 59

9 Height profiles of the flat regions near the ripples on the SiO_2-Si sample. 61

10 AFM measurements of the SiO_2-Si samples with a 216 nm thick oxide layer. 62

11 3-D representation of the AFM topographic images. 63

12 AFM measurements of the pits along the ripples on the etched SiO_2-Si sample. 64

13 Cross-sectional bright-field TEM images of the FIB-prepared SiO_2-Si specimen with an intact 216 nm oxide layer. 66

14 Bright-field high-resolution TEM micrograph (HRTEM) of the central regions of the ripples in the SiO_2-Si sample with an intact 216 nm thick oxide layer. 68

15 Dark-field TEM and HRTEM results of the same specimen shown in Figure 13 and 14. 69

16 EDX spectra of the same specimen as shown in Figure 15. The sampled locations on one of the ripples are indicated in the TEM image in (a). 71

17 SEM images of the ripples formed on the SiO_2-Si samples with different oxide thicknesses. 74

18 Observation of the ripples for the SiO_2-Si sample having an oxide layer of 1013 nm. 75

19 SEM images of the ripples formation as a function of the laser energy for the 1013 nm thick oxide sample after HF etching. 77

20 SEM images of the ripples formation at different laser energies for the oxide sample with an intact oxide layer of 112 nm. 79

21 SEM images of the ripples for the 112 nm oxide sample that was translated at a speed of 2000 μm/s in the y-direction perpendicular to the polarization of the E-fields. 80

22 SEM images of the patterns created on the SiO_2-Si samples when being irradiated using a 5X objective lens. 83

23 SEM images of LIPSS formed on a pure Si sample translating in the y-direction with a translation speed of 2000 μm/s. 85
24 Plot of the ripple periods as a function of peak laser fluence, for both the pure Si samples and the SiO_2-Si samples with an oxide thickness of 117 nm. 86
25 SEM images of the LIPSS formed at the SiO_2-Si interface when the translation speed is reduced to 100 μm/s. 88
26 AFM measurements for the LIPSS formed at the SiO_2-Si interface when the translation speed is reduced to 100 μm/s. 89
27 Change in the slope of the LSFL on a pure Si sample as a function of incident laser energy. 91
28 Change in the slope of the LSFL on a pure Si sample as a function of translating speed. 92
29 SEM image of the "sub-threshold" ripples on a bulk Si sample. 93
30 SEM image of the well-behaved ripples on a SiO_2-Si sample with an oxide thickness of 158 nm after being irradiated with $\lambda = 400$ nm laser pulses. 98
31 Cross-sectional bright-field TEM image of the FIB-prepared SiO_2-Si specimen with an intact oxide layer of 158 nm, showing the ripples produced at the SiO_2-Si interface after the sample was irradiated with laser pulses at $\lambda = 400$ nm. 100
32 Bright-field HRTEM micrographs of the same FIB specimen as shown in Figure 31. 102

33 HRTEM micrographs of the same ripple taken under different imaging modes. 103
34 Electron diffraction patterns (EDPs) of different sampling spots around the ripple produced with laser pulses at $\lambda = 400$ nm. 104
35 EDX spectra of different regions near one of the ripples on the same FIB specimen shown in Figure 31. 106
36 SEM images demonstrating the ripple evolution as a function of the incident laser energy at $\lambda = 400$ nm. 108
37 SEM images demonstrating the ripple evolution as a function of the translation speed at $\lambda = 400$ nm. 110
38 SEM images demonstrating the ripple evolution with variations in both the translation speed and the laser power when the 112 nm thick SiO_2-Si sample was irradiated at $\lambda = 400$ nm and translated along the y-direction. 112
39 SEM images demonstrating the LIPSS evolution as functions of both the translation speed and laser power for a pure Si sample that was irradiated at $\lambda = 400$ nm and translated along the x-direction. 114
40 SEM images demonstrating the LIPSS evolution as a function of the laser power when a pure Si sample was translated at a speed of 500 μm/s along the y-direction. 115
41 SEM images of typical results for the 112 nm thick oxide sample after being irradiated with 1 ps laser pulses, and at a translation speed of 2000 μm/s. 118

42 SEM images of typical results for the 112 nm thick oxide sample after being irradiated with 5 ps laser pulses, and at a translation speed of 2000 μm/s. 119

Chapter 1

Introduction

1.1 Brief introduction to ultrashort laser pulses

The notion of ultrashort laser pulses generally refers to electromagnetic waves produced by a laser in the form of wave packets whose time duration is between the range of pico- (10^{-12}) and femto- (10^{-15}) second [1]. The key advantage of ultrashort laser pulses is that a high optical peak power on the order of gigawatts (GW, 10^9 W), even terawatts (TW, 10^{12} W) can be readily attained by reducing the pulse duration and/or increasing the pulse energy of the laser pulses. Following by focusing high-power laser pulses, a peak intensity on the order of 10^{12} - 10^{16} W/cm^2 can be obtained [2].

The generation of such short laser pulses critically relies on the physics of mode-locking and practical techniques to achieve the mode-locking operation in a laser. The mode-locking mechanism can be described as imposing a fixed phase on all the longitudinal modes simultaneously oscillating in the laser cavity. The "locked" phases lead to the periodically constructive interferences among the equal-spaced modes,

thus producing a series of pulse trains with enhanced amplitudes in the frequency domain. By the argument of Fourier transformation, such a frequency spectrum can be, equivalently, viewed as a series of pulse trains that are also equally spaced in the time domain [1]. However, for most practical applications, the mode-locked pulses must be subsequently amplified through different amplification techniques. Among them, the most commonly applied technique is chirped-pulse amplification (CPA) that will be described in detail in Chapter 3.

The applications of ultrashort laser pulses have been extensively realized in many technological disciplines, such as material modifications in terms of welding and drilling [3], fabrication of waveguide and micro-fluid devices [4], direct patterning of laser-induced micro/nano structures used for biological purposes and in microelectromechanical systems (MEMS) [5], and so on. One of the most unique advantages of applying ultrashort laser pulses when processing materials is that it offers precise spatial modifications of the targets with minimum heat-affected volume upon laser irradiation [3]. It is brought about by the fact the ultrashort pulse durations are generally shorter than the electron-phonon interaction time that is on the order of 1 ps [6]. The cooling process of excited electrons after absorbing incident laser energy can be rapidly achieved by a direct solid-plasma transition whose time response is also generally shorter than 1 ps. Therefore, thermal conduction to the lattice via electron-phonon coupling can be negligible, and the resulting material modifications in terms of melting and vaporization can, thus, be localized and minimized [7].

1.2 Motivations of the research

The practical significance of the SiO_2-Si structure can not be overstated in the current technology. In the conventional CMOS-based devices, the SiO_2-Si structure acts as gate oxides to form a controllable current channel between the source and the drain in transistors [8]. With regard to the MEMS applications, the superior flexibility of manipulating and fabricating the microstructures that are made of the SiO_2-Si system provides the basic mechanical functions for many MEMS devices [9]. To obtain high-efficiency Si-based solar cells, thermally grown SiO_2 on Si substrates has been widely implemented as a simple technique to enhance the external quantum efficiency of the cells in the form of a surface passivation layer [10, 11].

The experiments in this research were first initiated by a former Ph.D student Eugene Hsu when he worked on one of his projects that was on the topic of single-shot and translated laser beam ablation of SiO_2-Si samples [12]. When analyzing the results from one of the translational ablation experiments, he discovered that there were some very subtle ripples produced on the SiO_2-Si sample. More strikingly, the oxide layer seemed to be intact, indicating that the ripples may form at the SiO_2-Si interface, rather than on the sample surface. His initial findings of the ripples and experimental frameworks established the foundation for this research.

Laser-induced periodic structures (LIPSS or often ripples) formed on the bulk materials have been considered as "universal phenomena" [13]. However, to my knowledge up to the time when this thesis is completed, the subject of systematically studying the ripple formation at the interface of a layered system is a relatively unexplored research domain. In the literature, there have been observations of the ripples formed at the SiO_2-Si interface [14–17]. Yet, no further detailed research has

been done on the ripple formation in terms of the effects of different laser conditions and material characterizations of the ripples.

From a purely scientific point of view, the investigation of the ripple formation at the SiO_2-Si interface will provide a novel prospect to help understand the physical mechanisms of the LIPSS formation and ultrashort laser ablation processes. From a technological point of view, one of the ultimate goals as a driving force for this research is to potentially apply the well-behaved ripples at the SiO_2-Si interface to function as on-chip optical gratings in a photonics-integrated circuit. Additionally, the theoretical and experimental framework of laser-processing SiO_2-Si samples can be extended to other layered systems consisting of different dielectric materials and semiconductors, such as Si_xN_y, Al_2O_3, InP, silicon-on-insulator (SOI) system, and so forth.

1.3 Overview of the thesis

The primary subject of this thesis is composed of experimental investigations of the ripples formed at the SiO_2-Si interface after the oxide samples are irradiated with ultrashort laser pulses, as well as subsequent characterization of the ripples using different microscopy techniques, such as optical microscopy (OM), scanning electron microscopy (SEM), etc.

Chapter 2 starts with introductory discussions focusing on the theoretical background of the physical interactions of ultrashort laser pulses with solid materials, mainly concerning dielectric materials and semiconductors. In addition, several widely accepted theories for elucidating the LIPPS formation mechanisms are also discussed. In order to demonstrate the originality of the research presented in this thesis, a

brief literature review regarding the current research status on the laser processing of SiO_2-Si samples is provided. Chapter 3 gives detailed descriptions on the general experimental setup concentrating on the laser system and micromachining setup. A variety of diagnostic techniques for characterizing the ultrashort laser pulses, which were implemented both before and during experiments are also mentioned in brief. Because the actual conditions of the samples under irradiation are considered to be a vital factor in determining overall experimental outcomes, Chapter 4 is entirely dedicated to providing specific information regarding sample preparations and various techniques that were used to analyze and characterize the samples, both before and after laser irradiation. The core of this thesis are the experimental results and their associated discussions which are presented in Chapter 5. The chapter is divided into three main sections by organizing the acquired findings under distinct laser irradiation conditions, particularly in terms of the ripple formation at the SiO_2-Si interface. Finally, Chapter 6 summarizes the key experimental results presented in Chapter 5. Furthermore, several potential research directions regarding both experimental and theoretical aspects are proposed and discussed.

Chapter 2

Background

In this chapter, a concise introduction to the physical processes of laser-matter interactions is first provided. The discussion is restricted to the interactions with dielectrics and semiconductors. Several prevailing theories that reveal the LIPSS formation mechanisms on bulk materials after ultrafast laser irradiation are discussed as well. The last part of this chapter is to provide a thorough historical overview and literature review focusing on the topic of laser processing of SiO_2-Si samples in different pulse duration domains covering from nanoseconds (ns) to femtoseconds (fs).

2.1 Brief overview of the physical interaction processes of ultrashort laser pulses with materials

2.1.1 Free carrier generation

The interactions begin with absorption of incoming photons by the materials in such a way that the photon energy will be transferred through various mechanisms to

excite free carriers in the materials. For dielectrics and semiconductors, there are generally four types of excitation mechanisms that are one-photon absorption, free carrier absorption, photoionization, and impact ionization [18, 19]. The last two types are classified to be non-linear processes as their effects are highly dependent on the laser intensity. Because of high intensity of the ultrashort laser pulses, photoionization and impact ionization play a more dominant role over other mechanisms in generating free carriers for dielectrics and semiconductors [20].

The one-photon absorption, often called linear absorption, is simply governed by the Beer-Lambert law. It states that the ability for a material to absorb photons with a specific wavelength only depends on its linear absorption coefficient at that wavelength, and is independent of the intensity [21]. As long as the photon energy is greater than the bandgap energy of the material, electron-hole pairs can be created through single-photon absorption. However, for photons having the wavelength within the visible and infra-red (IR) range, the linear absorption become negligible for wide-bandgap dielectrics with a bandgap larger than 3 eV, such as SiO_2 (9.0 eV) [22]. Still, for the SiO_2, a certain amount of linear absorption can occur through trapping states within the bandgap, which are mostly caused by lattice defects and impurities, such as silicon-oxygen weak bond, oxygen vacancy [21, 23].

Free carrier absorption, often referred to the inverse Bremsstrahlung, is a process whereby the existing or excited electrons in the conduction band (CB) can further absorb incident photon energies by interacting with phonons, thus promoting themselves into higher energy states within the CB. The free carrier absorption coefficient is related to the imaginary part of the refractive index that can be determined by evaluating the complex dielectric function for a known material [24, 25].

According to Keldysh [26] who first developed the theoretical framework, photoionization has two distinct regimes that are the multiphoton ionization (MPI) regime and the tunnelling ionization regime, in addition to an intermediate regime where both are coexisting. The dimensionless Keldysh parameter (γ) [26] determines which regime dominates the photoionization mechanism.

MPI involves a process of simultaneous absorption of multiple photons that leads to electron-hole creations when the accumulated photon energy upon absorption is larger than the bandgap energy of the material. For dielectrics and semiconductors, such as SiO_2 [27] and Si [28], it has been shown that the MPI plays a crucial role in the carrier generation and subsequent ablation processes when the laser intensity is within the range of 10^{13} - 10^{14} W/cm^2 in addition to when the laser wavelength is in the visible and IR ranges.

The tunnelling ionization can be generally described as a process of promoting a valence electron by allowing it to tunnel through the Coulomb potential well to the conduction band. It is achieved by suppressing the potential barrier with application of an extremely high laser field. The effects of the tunnelling ionization only become significant when γ is much less than 1, which is when the laser intensity is extremely high (larger than 10^{15} W/cm^2) and the laser frequency is low (e.g. in the UV range) [29].

Through the free carrier absorption or the photoionization, a portion of electrons can be excited to much higher energy states in the CB. Once the excited electrons have enough kinetic energy that can overcome the ionization potential of the bound electron, additional free electrons will be created in such a way that the excited electrons make collisional impacts with the valence electrons. The newly generated free

electrons can absorb more photon energy and trigger a sequence of impact ionization, resulting in an exponential increase in the carrier density [3, 18]. This process is referred to as the avalanche ionization whose effect is highly sensitive to the initial free electron density and often assumed to have a linear dependence on the laser intensity. The avalanche ionization ultimately causes the electron density to saturate at a critical density (N_c) where formation of a plasma state is reached [30].

2.1.2 Electronic thermalization

Followed by the carrier excitation, the lattice structure is at a highly unstable and non-equilibrium state owing to the high density of free carriers. To restore thermal equilibrium for the system, the free carriers must be redistributed in the band structure through two main relaxation mechanisms: carrier-carrier scattering and carrier-phonon scattering [19].

The carrier-carrier scattering involves an electrostatic interaction between two carriers, for instance, electron-electron coupling or electron-hole coupling [6]. While maintaining both the total energy and the number of the excited carriers to be constant, a quasi-equilibrium described by the Fermi-Dirac distribution is established among the carriers after a few hundred femtoseconds. The hot electron gas is characterized by an electron temperature (T_e) [31].

Regarding the carrier-phonon scattering, it is a process where free carriers interact with phonons via both absorbing and emitting them, thus resulting in energy transfer to the lattice. Meanwhile, this process also helps cool down the carriers in the quasi-equilibrium on a time scale of 0.1 to 1.0 ps [19]. Eventually, after the complete relaxation of free carriers, the emitted phonons will be redistributed in the lattice.

As a result, thermal equilibrium characterized by a lattice temperature (T_i) according to the Bose-Einstein distribution is reached within a few picoseconds [6, 32]. The time scales for each scattering mechanism are shown in Figure 1.

2.1.3 Phase transition and structural change from thermal effects

Once the electron-lattice comes to the state of thermal equilibrium, the deposited thermal energies via absorption of the laser energy give rise to various phase transitions of the materials and, ultimately, materials removal. It largely depends on the material properties and laser parameters. However, for laser pulse durations longer than 10 ps, the electron-lattice thermal equilibrium is achieved during the pulse duration. In this case, the thermal diffusion dominates the process of heat transfer, which leads to the heterogeneous melting of materials. Limited by the melting front velocity, it usually takes on the timescale of a few microsconds for the materials to resolidify and return to initial lattice temperature before laser irradiation [33].

There are four major phenomena occurring when materials undergo phase transitions. They consist of thermal melting (mainly homogeneous melting), expansion (including formation of either superheated fluid, overcritical fluid, solid-plasma), material removal (including either direct ablation or vaporization), and finally resolidification. Determined by the relationship between the incident laser fluence and the ablation threshold fluence of a targeted material, the exact material phase evolution and ablation mechanisms are schematically illustrated in Figure 1. As the ablation is a highly dynamic and non-equilibrium process, its underlying physical mechanisms have been extensively investigated and modelled based on molecular dynamics by

numerous research works [25, 34–36]. The details of each ablation mechanism will not be explicitly mentioned here, but are further described in the relevant references provided.

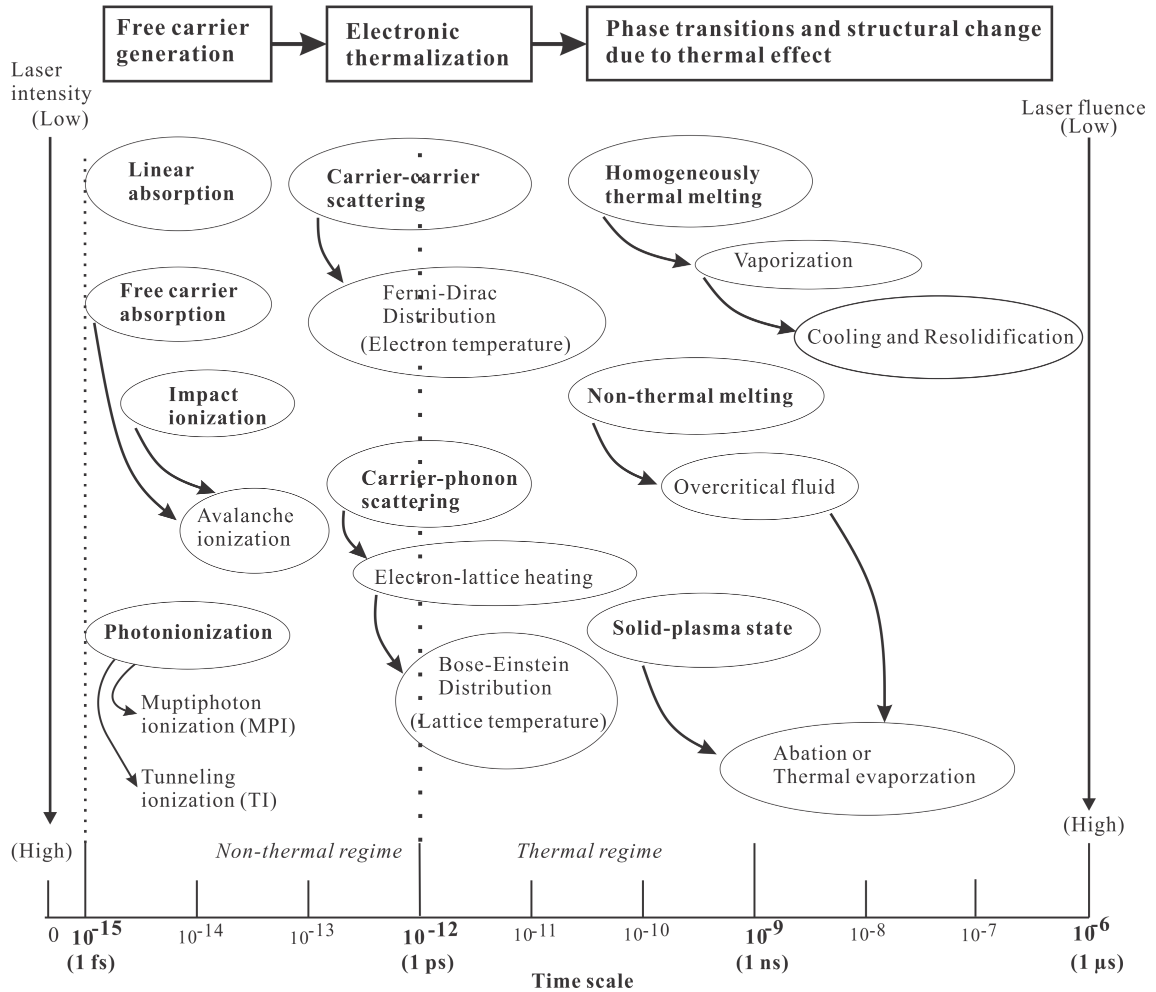

Figure 1: Schematic representation of the physical interaction processes of ultrashort laser pulses with solid materials, and subsequent material response. It is adopted and modified based on the references of [19, 37].

2.2 LIPSS formation on bulk materials after ultra-fast laser irradiation

Since Birnbaum first reported the laser-induced periodic surface structures (LIPSS) in 1965 [38], the formation of LIPSS has been studied extensively on all kinds of solid materials, including metals, semiconductors, dielectrics. The "classical" LIPSS concern periodic structures aligning along the direction that is perpendicular to the polarization of the incident laser electric-fields (E-fields) [39]. Based on the difference in the spatial periodicity, the LIPSS can be generally classified into two main sorts that are the low spatial frequency LIPSS (LSFL) and high spatial frequency LIPSSs (HSFL). The LSFL refers to the LIPSS with spatial periodicity close to the incident laser wavelength, whereas the HSFL concerns the LIPSS with spatial periodicity that is substantially lower than the laser wavelength [40]. To date, there is no a single theory that can provide an universal explanation for the LIPSS formation combining both LSFL and HSFL. For clarity, two separate sections are dedicated to describing theoretical frameworks for elucidating the formation mechanisms for LSFL and HSFL, respectively. Nevertheless, the underlying physical mechanisms of forming both features are closely interrelated.

2.2.1 Sipe and SPP theories for generation of the LSFL

Sipe theory

Developed and formalized by Emmony [41] and Sipe et al. [39, 42, 43], the well-established Sipe theory has been accepted as the most reliable theoretical model in explaining the physical mechanisms of the LSFL formation on most materials. The

Sipe theory suggests that LSFL results from the interference of the incident laser fields with surface-scattered electromagnetic waves that are produced at the rough surfaces during the laser pulse durations [39]. The sources of surface scattering can originate from local defects, intrinsic microscopic roughness of the surface, spatial variations of the assumed dielectric function, and so on [44]. It is the optical interference that causes a series of "chain reactions" leading to the formation of LSFL. In short, the main events occur in such a sequence of creation of fringe patterns, inhomogeneous redistributions of the laser energy, then the subsequent deposition into the materials, and eventually periodically modulated ablation of materials [45].

Based on the Sipe theory, the amount of inhomogeneous energy deposition into the materials can be described by a combined expression of $\eta(\mathbf{k}, \mathbf{k_i}) \times \|b(\mathrm{k})\|$, where η is defined as a dimensionless efficacy factor that quantitatively accounts for how much the inhomogeneous energy can be absorbed at a value of the wave vector $\mathbf{k}$. The factor of $\|b(\mathrm{k})\|$ is the Fourier component of the roughness function that can be modelled by two numerical factors: shape factors (s) and filling factor (f), in order to describe the homogeneously rough surfaces with small varying amplitudes [39]. The details of theoretical derivations and implementation of the numerical modelling for different bulk materials can be found in the references [39, 42, 46–49]. The spatial periodicity (Λ) of the LSFL can be related to the incident laser wavelength (λ) and angle of incidence (θ) via the following equation for s-polarized light:

$$\Lambda = \frac{\lambda}{1 \pm sin(\theta)} \tag{1}$$

Surface plasmon polaritons (SPPs) theory

Because the Sipe theory does not take into account the transient changes in the dielectric constant of a material during the laser pulse duration, the assisting role of generation of surface plasmon polaritons (SPPs) on the LSFL formation has been proposed, investigated and confirmed by many authors [49–51]. Surface plasmons are regarded as a collection of excited electrons that oscillate longitudinally and propagate along a metal-dielectric interface within optical frequencies [52]. When the dimension of surface roughness is much smaller than the incident wavelength, a local field can be generated by the simultaneous oscillation of surface charges coherently resonating with the incident laser fields, thus resulting in the excitation of SPPs [53]. Furthermore, the following dispersion relation between the wave vectors of the SPP and the incident light must be met in order to excite the SPPs [52]:

$$k_{sp} = k_0 (\frac{\epsilon_1 \epsilon_2}{\epsilon_1 + \epsilon_2})^{1/2} \quad (2)$$

where k_{sp} and k_0 stand for the wave vectors of the SPP and the incident light in vacuum. ϵ_1 and ϵ_2 are the relative dielectric constants of two different mediums whose interface contains the SPPs. Owing to the high concentration of free electrons in its band structure before laser irradiation, generation of the SPPs on a metal surface can be much more readily achieved [50]. For dielectrics and semiconductors under intense femtosecond laser radiation, it has been proven that high carrier density in a non-equilibrium state, which are achieved by the non-linear absorption processes will change the sign of the dielectric permittivity, thus leading to the excitation of SPPs [54].

It is believed that the interference between the SPPs and the incident laser radiation enhances the localization of the absorbed laser energy. It plays a critical role in initiating the formation of LSFL [55]. According to Huang, et al. [50], the orientation of the LSFL is determined by the transverse magnetic (TM) characteristic of the SPPs. In addition, the spatial period of the LSFL is related to incident laser wavelength, which is given by the following equation [50]:

$$\Lambda = \frac{\lambda}{\frac{\lambda}{\lambda_s} \pm \sin\theta} \tag{3}$$

where Λ is the ripple periodicity, λ is the incident laser wavelength, and θ is the incidence angle of the laser beam on the sample surface. The sign of $\pm$ indicates that the surface waves propagate in both forward and backward directions. The symbol λ_s denotes to the plasmon wavelength at a metal-dielectric interface, which can be found as [50]:

$$\lambda_s = \lambda\sqrt{\frac{\epsilon' + \epsilon_d}{\epsilon' \epsilon_d}} \tag{4}$$

where ϵ' is the complex dielectric constant of a metal or metal-like material; ϵ_d refers to the dielectric constant of a dielectric medium. For air, ϵ_d is approximately equal to 1. For normal incidence when $\theta = 0$, the equation 3 can be simplified to $\Lambda = \lambda_s$.

2.2.2 SHG theory for generation of the HSFL

In recent years, the formation of HSFL has exclusively been observed in the experiments conducted under ultrashort laser irradiation. They are discovered on a variety of materials, including metals, dielectrics, and semiconductors, such as stainless steel

[56, 57], alloy [58], ZnSe [59], ZnO [60], Si [61], InP [40, 48, 62], GaP and GaAs [40]. Nevertheless, there has not been a broadly accepted theory, like the Sipe-SPPs theory for the LSFL formation, in the literature when it comes to elucidating the physical mechanisms of the HSFL formation. Based on their experimental results, many authors have proposed plausible formation mechanisms that are second harmonic generation (SHG) [40, 59, 61], self-organization [63], excitation of SPPs [53, 64, 65]. Among them, the significant role of the SHG mechanism in producing the HSFL on Si, Ge and compound semiconductors has been particularly recognized [40, 66].

According to the SHG theory, laser pulses with a sufficient peak fluence can enable materials to efficiently generate light with a wavelength that is half of the incident laser wavelength via a SHG process. Then the interference between the generated SHG light and the surface-scattered EM waves will lead to the formation of the HSFL whose spatial periodicity is substantially smaller than the fundamental laser wavelength. Regarding the spatial periodicity, physical structures, and ablation depth, the development of HSFL mainly depends on the laser fluence, the number of laser pulses and the angle of incidence [67]. Predicted by the SHG mechanism, it is expected that the spatial periodicity (Λ) of HSFL obeys the following equation [59]:

$$\Lambda = \frac{\lambda}{2n_{\lambda}}; \tag{5}$$

where n_{λ} is the refractive index of a material irradiated at a wavelength of λ. However, in order to account for the observed deviation between the experimentally measured periods and the theoretical predictions, the transient change in the refractive index caused by the non-linear effects occurring during the pulse duration, such as the Kerr effect and generation of free carriers, must be numerically modelled and solved based

on the Drude model [61, 67].

2.3 Literature review of the ultrashort laser pulse processing of SiO_2-Si samples

As mentioned above, numerous experimental and theoretical studies have been conducted on the LIPSS formation under ultrashort laser irradiation on bulk materials. In contrast, it is still an unexplored domain when it comes to investigating the periodic structures formed at the interface of a layered system, such as the SiO_2-Si structure. Based on my literature research so far, there is no similar study or experimental finding specifying the ripple formation at the SiO_2-Si interface under femtosecond laser pulse irradiation that has yet been reported in the literature. The thesis will be the first published documentation that focuses on this particular area of producing ripples at the interface of a layered structure using ultrashort laser pulses, in addition to the subsequent characterizations of the ripples. Nevertheless, there have been quite a few reported research works done on the topic of laser-processing the SiO_2-Si samples. The following sections summarize the main findings from those investigations.

2.3.1 Nanosecond regime

The earliest study on the ripple structures formed at the interfaces of SiO_2-Si was conducted by Yong F. Lu, et al. in 1996 [16]. But their experimental work was limited in the nanoscale domain in terms of pulse duration as the laser source used was a KrF excimer laser operating at $\lambda = 248$ nm and a pulse duration of 23 ns. The oxide samples were prepared in two different oxidation conditions that are dry oxygen gas

(dry) and water vapour (wet). The oxide thicknesses covered the range from 24 nm up to 440 nm. The samples were processed under stationary laser-irradiation with varying numbers of laser pulses on a given spot [16].

Y.F. Lu, et al. suggested that the primary mechanisms of ripple formation at the SiO_2-Si interface were likely due to surface waves, freezing of capillary waves, and generation of transient periodic heating patterns [68]. As the SiO_2 is transparent to $\lambda = 248$ nm light, the majority of the incident laser energy is absorbed by the Si substrate whose surface, in turn, melts. In the meantime, the SiO_2 layer remains solid and acts as an elastic film that exerts restoring forces to the surface wave in the form of simultaneous oscillations. Based on this reasoning, a linear dependence of the periodicity of the ripple structures on the SiO_2 layer thickness was derived in the reference of [68] and verified by experimental results in [16]. In addition, Y. F. Lu, et al. found that the preparation method of the SiO_2 has no effect on the ripple formation with respect to their structures and threshold laser fluence [16].

2.3.2 Picosecond regime

S. Hermann, et al. [14] investigated laser ablation of SiO_2-Si layers from Si substrates using 8 - 9 ps pulses for the purpose of forming electric contact openings in the oxide layer for Si-based solar cells. Stationary single-shot laser irradiations were carried out on SiO_2-Si samples whose oxide thicknesses are in the range of 110 to 320 nm. Laser beams with a Gaussian profile and of three different wavelengths (1064 nm, 532 nm, and 355 nm) were utilized. By correlating the observations of the ablation spots with the "D^2" technique [69] when measuring the spot size for a Gaussian beam, S. Hermann, et al. defined two empirical threshold fluences: melting threshold

fluence and breaking threshold fluence. The first threshold is defined as the minimum fluence that can cause a colour change on the material surface indicating a change of reflectivity of the material. The latter one is considered as the minimum local fluence required to break and remove the SiO_2 layer from the Si substrate [14].

The experimental results presented in the reference [14] strongly supported that the removal of the SiO_2 layer was mainly caused by the vapour pressure originating from the melting and subsequent vaporization of the Si substrate upon laser irradiation. This finding provides strong evidence to support that lifting-off of the SiO_2 layer is a thermal-assisted mechanical deformation process, rather than a direct laser ablation process. It then can be concluded that the non-linear absorption of laser energy in the SiO_2 layer has very little effect on the delamination process, even at laser fluences greater than the breakdown threshold of the SiO_2 [14].

After taking into account of the variations in the reflectivity of the SiO_2-Si samples due to different SiO_2 thicknesses and laser wavelengths, the melting threshold fluence (for oxide thicknesses within 110 - 320 nm) was determined to be roughly around 0.47 J/cm^2 for $\lambda = 1064$ nm, and 0.1 J/cm^2 for $\lambda = 532$ nm and 355 nm [14]. These values are nearly independent of the SiO_2 thickness, which can, in turn, justify that the SiO_2 layer has very little impact on the delamination process. Regarding the breaking threshold fluence, it varied with both the oxide thickness and the laser wavelength. Its proportional dependence on the oxide thickness can be easily explained by the fact that the increasing mechanical strength with increasing oxide thickness makes it more difficult for the SiO_2 layer to be removed [14].

Moreover, S. Hermann, et al. pointed out that the dependence of threshold fluences, including for both melting and breaking, on the laser wavelength can be largely

accounted for the variation of the heat affected volume in the substrate at different laser wavelengths. There are two key material parameters that determine the heat affected volume, which are the optical penetration depth (α^{-1}) and thermal diffusion length (l) [3]. As the optical penetration depth decreases dramatically with decreasing wavelengths, it leads to much shallower heat affected zones in the substrate, thus resulting in a greater melting threshold fluence for the 1064 nm wavelength than those for the 532 nm and 355 nm wavelengths [14].

2.3.3 Femtosecond regime

With the research interest of producing contact openings in passivating dielectric layers on Si-based solar cells, T. Rublack, et al. [70–73] conducted a very thorough and systematic study on the delimitation of thin SiO_2 layers from a Si substrate using pico- and femtosecond laser pulses. Apart from focusing on the SiO_2, other common dielectrics used for solar cells, such as Si_xN_y and Al_2O_3, were also briefly examined [72].

In the reference [71], the laser irradiation conditions were maintained in a single-shot scenario at λ = 800 nm, but with four different pulse durations that were 50, 700, 1000, and 2000 fs. SiO_2-Si samples with a fixed oxide thickness of 110 nm were used for all the experiments. For the 110 nm thick oxide, it is found that its melting threshold fluence was in the range of 190 to 320 mJ/cm^2, and its breaking threshold fluence was between 270 and 380 mJ/cm^2. Both threshold fluences increase as the pulse durations get broadened from 50 fs to 2 ps. According to T. Rublack, et al, this monotonic relationship can be explained by considering the ablation process under different pulse durations [71]. It is known that the characteristic time for

electron-phonon interaction is on the order of 1 ps [15]. Therefore, for pulse durations much shorter than this, such as 50 fs, the high density of electron-hole plasma is quickly achieved via MPI absorption and subsequent quasi-metallic absorption. As a result, only a small portion of incident photons can penetrate into silicon bulk during the pulse duration. At the SiO_2-Si interface, a shallow layer of Si approximately a few nanometers in depth absorbs most of the laser energy and undergoes a phase-transition from melting to vaporization. It then causes the removal of SiO_2 layer. In contrast, for longer pulse durations close to 1 ps, part of the excited electrons has the chance to interact with the lattice during the pulse duration, thus in turn leading to a lower density of electron-hole plasma. The final outcome is an increase in the penetration depth and a reduction in the temperature at the SiO_2-Si interface.

In order to extend the experimental results presented in [71], T. Rublack, et al. further explored the dependence of the threshold fluence on the laser wavelength in the reference [72]. Besides the standard 800 nm wavelength used in [71], four different wavelengths including 400, 515 and 1030 nm were added to the irradiation conditions. The oxide thickness of SiO_2-Si samples remained at 110 nm. It was found that, for the SiO_2-Si samples, the breaking threshold fluence dropped by roughly a factor of two as the laser wavelength decreased from 1030 nm to 400 nm. Meanwhile, the melting threshold fluence decreased by roughly a factor of four with the same decreasing trend in the wavelength. T. Rublack, et al. provided explanations for this finding by considering that the linear absorption coefficient of Si varies significantly as the laser wavelength changes. For example, the linear absorption coefficient of Si is 30.2 cm^{-1} at $\lambda = 1030$ nm, compared with the value of 9.52×10^4 cm^{-1} at $\lambda = 400$ nm [74]. Because the larger coefficient facilitates generation of the charge carriers, it then

expedites the process of reaching a high density of the electron-hole plasma within the pulse duration. Consequently, similar to the case of reducing pulse duration, reduction in the laser wavelength also lowers the threshold fluences [72].

Chapter 3

Experimental setup

The chapter will provide key information about the common instruments and their configurations that were employed to conduct the laser-irradiation experimental work for this research. The discussion will follow a sequence of first introducing the laser systems that produce ultrashort laser pulses, then moving on to describing the setup of optical beam path guiding the laser beam to the final stage. It is the micromachining setup where the actual laser processing is performed. Various experimental techniques that were implemented to characterize and monitor the ultrashort laser pulses will be also mentioned at last.

3.1 Ultrashort-pulse laser system

The ultrafast laser system used in the research is a commercial kilohertz pulsed Titanium-doped sapphire (Ti:Sapphire) laser amplifier system purchased from Spectra-Physics, a division of Newport Corporation. It is composed of four main modules that are a mode-locked Ti:Sapphire laser (Tsunami) along with its pump laser (Millennia

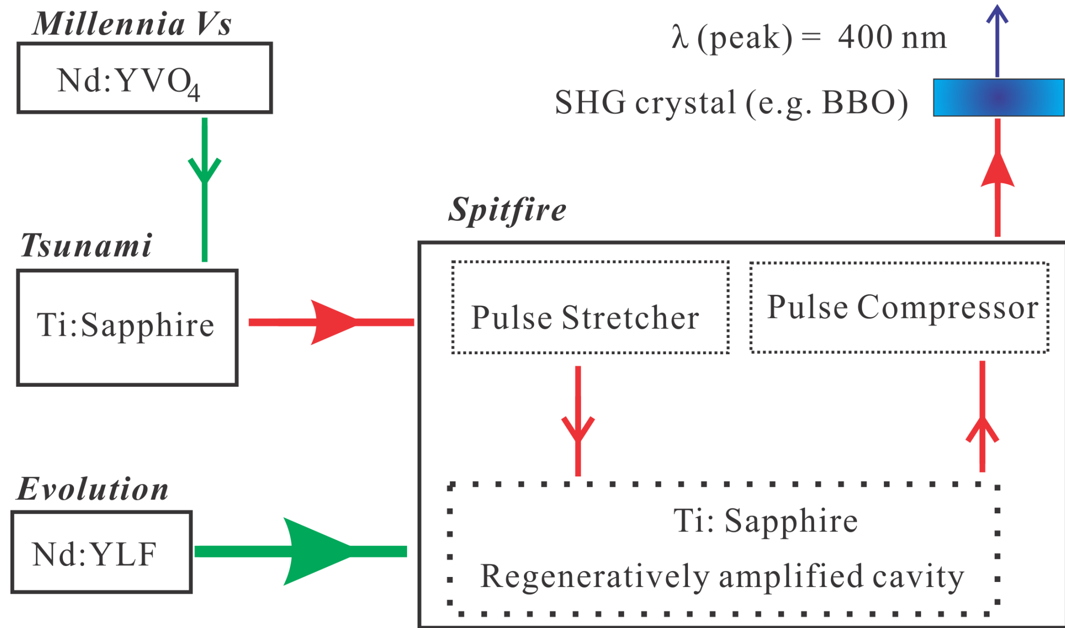

Figure 2: Schematic overview of the laser system used in the research. Specific operating conditions for each laser system can be found in Table 1.

Vs), as well as a multi-kilohertz pulsed Ti:sapphire regenerative amplifier (Spitfire LCX) along with its pump laser (Evolution). The schematic overview of the laser amplifier system is shown in Figure 2.

3.1.1 Millennia Vs

The Millennia Vs is a diode-pumped solid state (DPSS) laser whose gain medium is a neodymium-doped yttrium vanadate ($Nd:YVO_4$) rod. Two arrays of GaAs-based laser diodes produce light with a wavelength of 809 nm, which in turn optically pump the $Nd:YVO_4$ crystal via fiber optics bundles. The resulting emission of 1064 nm wavelength light from the $Nd:YVO_4$ gets frequency-doubled after going through a lithium triborate (LBO) crystal within the cavity. The final output from the Millennia Vs is 532 nm continuous-wave (CW) light, and its output power is typically operating

Laser system	Millennia Vs	Evolution	Tsunami	Spitfire LCX
Laser modes	CW	Pulsed	Pulsed	Pulsed
Center wavelength	532 nm	527 nm	800 nm	800 nm
Linewidth at FWHM	-	-	13 nm	10 nm
Output power	4.2 W	-	-	-
Output pulse energy	-	3.2-3.5 mJ	9 nJ	0.42-0.46 mJ
Pulse duration	-	tens of ns	90 fs	127 - 198 fs
Repetition rate	-	1 kHz	82 MHz	1 kHz

Table 1: Normal operating conditions of each laser system. Note: Details of each laser system can be referred to in its own manufacture manual.

at 4.2 W.

3.1.2 Evolution

The Evolution is also a DPSS laser containing a neodymium-doped yttrium lithium-fluoride ($Nd:LiYF_4$) rod as its gain material in the cavity, which is pumped by four arrays of AlGaAs diode lasers. The emission wavelength from the $Nd:LiYF_4$ crystal peaks at 1054 nm. Then, a LBO crystal converts the 1054 nm light into 527 nm light via SHG. The Q-switched laser pulses with a repetition rate of 1 kHz are attained by inserting an acoustic-optical modulator (AOM) in the cavity. However, the repetition rate can be varied from 1 kHz to 10 kHz by manually changing the setting of the AOM. Because the Evolution pulses optically pump the Ti:Sapphire crystal in the regenerative amplifier cavity, which in turn amplifies the Tsunami pulses, the repetition rate of the Evolution pulses determines the repetition rate of the Spitfire output pulse. Under normal operations, the pulse energy from the Evolution is within the range of 3.2 - 3.5 mJ.

3.1.3 Tsunami

The Tsunami produces linearly-polarized pulses with a pulse width of approximately 90 fs at a repetition rate of 82 MHz. The fixed repetition rate is determined by the cavity length that determines how long it takes for the mode-locked pulse to make a full round trip in the cavity. The central peak wavelength from the Tsunami output was purposely maintained at 800 $\pm$ 3 nm. Its linewidth at the full-width half maxima (FWHM) was also fixed at 13 nm to ensure that there was adequate spectral bandwidth in the seeding pulses for subsequent amplification in the Spitfire. The pulse energy from the Tsunami is generally in the neighbourhood of 9 nJ. As this pulse energy is too low for most material processing and micromachining purposes, it is necessary to amplify the pulses without compromising their pulse width very much. Owing to the losses caused by going through the optics, such as gratings, mirrors in the stretcher part of the Spitfire, roughly 58% of the Tsunami output power is seeded into the regenerative amplifier cavity.

The production of ultrashort pulses in the Tsunami is achieved based on two key mode-locking mechanisms. One is the active mode locking using an amplitude modulator that is to initiate the mode-locking process from a CW running mode. The other is called Kerr-lens modelocking (KLM) that is to sustain the mode-locking. An AOM used as the amplitude modulator is inserted at the output end of the Tsunami cavity. The key components of the AOM include a high-quality polished quartz facing parallel to the direction of light propagation and a piezoelectric transducer producing a radio-frequency (RF) signal through a driving circuitry. When the AOM is turned off, the CW light inside the cavity passes through the quartz crystal without any loss.

However, when the AOM is turned on, the RF signal from the transducer generates

an acoustic wave in the quartz crystal, it in turn creates time-dependent variation in the refractive index of the quartz. While propagating through the crystal, part of the light gets diffracted and frequency-shifted due to the existing grating in the quartz. Part of the light remains undisturbed and gets reflected back through the modulator. As long as the modulation frequency of the RF signal matches perfectly the laser repetition rate that is determined by the round-trip time of the Tsunami cavity, the induced time-dependent periodic loss triggers "locking" of the phase relationship between the modes of the laser cavity, thus resulting in a train of pulses in the cavity. Once the pulse train is created, the AOM is turned off.

But, the mode-locking is still preserved through the KLM. The Ti:Sapphire crystal not only acts as a gain medium, but it also functions as a Kerr medium with its nonlinear refractive index. Owing to this nonlinear refractive index, the mode-locked pulses simultaneously undergo self-focusing and self-phase modulation (SPM) while propagating through the crystal. The shorter pulses have higher peak intensities than those of the longer pulses. Thus, they get focused more tightly in the crystal and undergo less total loss [1]. To produce the shortest pulse, two pairs of prisms are placed in the Tsunami cavity to compensate the pulse broadening caused by the SPM from the crystals and positive group-velocity dispersion (GVD) from the optics. The ultimate outcome is that self-sustained mode-locked ultrashort pulses are produced in the Tsunami.

3.1.4 Spitfire LCX

The three major modules in the Spitfire are a pulse stretcher, a Ti:sapphire regeneratively amplification system, and a pulse compressor. The attainment of ultrashort

pulses with high pulse energy in the Spitfire while avoiding to cause detrimental effects on the pulses themselves and the applied optics is based on the technique of chirped-pulse amplification (CPA). As the pulse duration shrinks from the nanosecond domain to picosecond and femtosecond regimes, the peak fluence of the pulse can be easily on the order of GW/cm^2 [75], even TW/cm^2 [76]. This value is close to the optical damage threshold for the Ti:Sapphire crystal, which is on the order of tens of GW/cm^2 [77].

Furthermore, due to the nonlinear refractive index of the crystal, the Kerr effect and SPM effect will become significant as the high intensity pulses approach the respective threshold levels. In the spatial domain, the Kerr effect largely results in a spatial variation of the laser beam intensity. Once the laser power exceeds the critical power, the self-focusing effect will induce regional breakdowns of the laser beam. In the time domain, as the intensity is also time-dependent, the Kerr effect will bring about wavefront distortion to the laser beam while it is propagating through the crystal. This distortion can be considered as SPM indicating that there exists phase differences between the weaker edge and the more intense part of the beam, thus resulting in creation of new frequency components. The amount of accumulated distortion is described by the B-integral equation that can be found in the reference [29].

To overcome all the issues caused by the high peak intensity, the CPA technique was first introduced by D. Strickland and G. Mourou in 1985 [78]. The essence of CPA is to expand a pulse in the time domain by introducing a specific amount of dispersion that causes a frequency-dependent delay in the pulse spectrum, termed as "chirping" of the pulse. When the sign of dispersion is positive, the chirp is regarded

as positive meaning that light with lower frequency (red part) travel ahead of light with higher frequency (blue part). The opposite effect occurs for negative chirp. Then, the chirped pulse gets amplified by passing through an amplifying medium. Finally, the amplified pulse is compressed close to its original pulse duration.

3.2 Setup of the optical beam path

The Spitfire output beam is guided to the micromachining setup where all the experiments are actually carried out. Because the laser power is quite excessive for most of experiments occurring in the lab, as well as for the sake of safety reasons, an optical attenuation line is utilized in order to reduce the power in a controllable fashion. The schematic overview of the setup containing optical and mechanical components is illustrated in Figure 3.

For experiments undertaken at $\lambda = 800$ nm, an ultrafast beam splitter with 20% reflection was placed at the position of M1 with a 45°angle of incidence. The beam splitter is specially designed to minimize the pulse dispersion and wavefront distortion of the ultrashort pulse upon reflection and transmission. While ensuring that the input power is sufficiently high for conducting experiments after the beam propagates through subsequent optics, it is also imperative to reduce the laser power enough in order to prevent nonlinear effects, such as SPM and Kerr effect from significantly altering the pulse characteristics. A telescope consisting of a positive and a negative lens is positioned right after the beam splitter. It focuses the beam from a diameter of originally 10 mm down to roughly 4 mm in order to avoid any spatial clipping on edges of the downstream optics.

With the combination of a thin film polarizer (TFP, Newport 11B00UP.26) and a

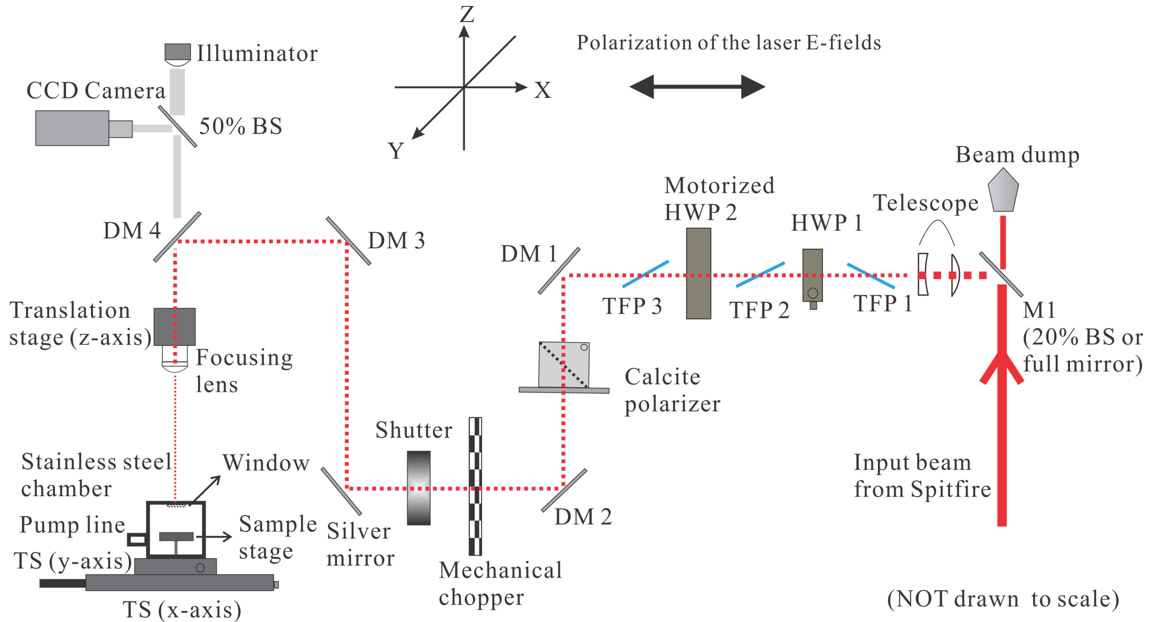

Figure 3: Schematic diagram of the setup of the optical beam path. Abbreviations in the diagram: beam splitter (BS); dielectric mirror (DM); thin-film polarizer (TFP); half-wave plate (HWP); translation stage (TS).

zero-order half-wave plate (HWP) that is mounted in a rotation stage, the intensity of the laser beam can be continuously adjusted by manually rotating the HWP. The use of another thin film polarizer just before the HWP is to enhance the purity in polarization of the input pulse by eliminating the residual s-polarized components that are perpendicular to p-polarized ones in the main pulse. Over a very narrow bandwidth of 785 - 815 nm, the extinction ratio for the TFP is 95:1 that is relatively low compared to a regular calcite polarizer. However, due to the fact that the TFP is very thin, it has an advantage in having much less dispersive material inserted in the beam path for the ultrashort pulse to travel through. Thus, the wavefront distortion can be kept to a minimum level.

In the meanwhile, the nonlinear effect can be reduced as well. In order to be able to vary the optical power in a precise and automated manner, another set of optics

comprised of a TFP and a zero-order HWP is employed. The HWP is mounted on a motorized rotation stage (Newport SR50CC) controlled by a motion driver (Newport ESP300) using a in-house computer program. At the end of the optical path, there is a Glen-laser prism polarizer (CVI CPAS-670-1064) in place, which is made of two calcite prisms with an air gap. Thanks to its high extinction ratio of 50,000:1, the calcite polarizer acts as the final component to purify the polarization of the pulse. As the incident laser power has been reduced significantly before entering, the nonlinear effects in the calcite polarizer should be negligible. When carrying out the experiment at $\lambda = 400$ nm irradiation, however, the calcite polarizer must be removed from the beam path as it is AR-coated within the range of 670 - 1064 nm wavelength, thus is not suitable for $\lambda = 400$ nm light.

3.3 Micromachining setup

After passing through the optical setup, the laser beam is directed into a stainless steel chamber by using four folding mirrors (DM2, silver mirror, DM3 and DM4 seen in Figure 3). Inside the chamber, a flat sample stage is screwed down to its bottom and used to secure a sample under irradiation. The chamber is covered by a stainless steel lid with an opening in its centre for placing a transparent window that allows the beam to go through. It is well documented that the laser-induced plasma created during the interaction of the intense ultrashort laser pulse with solid materials can result in X-ray emission [79–81]. Therefore, as a safety measure for the operator and others, the thickness of the stainless steel chamber and lid was designed to be about 1/4 inch. Thus, it can completely contain the small amount of X-rays generated during micromachining process.

In most experiments, a 1 mm-thick fused silica window (CVI PW1-1004-UV) with a diameter of 1 inch is used. In some cases, for example, to irradiate a large area on a sample, a 6.4 mm-thick fused silica window (CVI PW1-2025-UV) with a diameter of 2 inches can be used. To prevent any leaking emission of X-rays that may penetrate through the window, a 3 mm-thick C-shaped copper shield is positioned on the lid and surrounded the window. A hand-held radiation detector (Eberline RO-20 ion chamber) is frequently employed to confirm that there is actually no measurable emission of X-rays from both the chamber and the window while irradiating samples. As an additional safeguard, a transparent acrylic-based shield that can withstand high-energy X-rays up to 25 keV is installed onto the optical table between the chamber and the operator. In any case, when conducting micromachining experiements, the maximum average laser power used is around a few milliWatts under normal operating conditions. Thus, it is extremely unlikely to produce any measurable penetrating X-rays, even if there were no shielding at all.

During the process of micromachining and material ablation, there will be debris created from the interactions even though the actual quantities are infinitesimal for most experiments. For the sake of safety, irradiating samples is performed under a rough vacuum environment in which the condition is achieved by continuously evacuating the chamber using a rotary vane pump (BOC Edwards RV8). The exhaust of the pump is filtered and sent to a fume hood line. For most of the experiments in this thesis, the pressure in the chamber maintained by the pump was within the range of 40 - 60 mTorr. The value was measured and monitored by using a Pirani vacuum gauge (KJL912001) with a pressure display (KJL2000D) from Kurt J. Lesker Company. The pressure gauge was calibrated on another ultra-high vacuum pump by

Paul Dube in the summer of 2012. It was verified that the gauge provided accurate measurement at a very low pressure down to 10^{-6} mTorr.

A likely cause limiting the residual pressure to around 40 mTorr is because the connecting tube between the pump and the chamber is very long and attached to extra valves to control the air flow. In addition, the wear and tear of the o-rings in the chamber may lead to long-term increase in the pressure. In order to gain precise control in the movement of samples, the micromachining chamber is secured on two motorized translation stages (Newport UTM100PP.1) that can translate the sample within a x-y plane. Furthermore, a focusing lens was mounted to a micrometer whose base is also attached to a motorized translation stage (Newport MFN25PP) that can move along the z-axis. Three translation stages were controlled by a motion driver (Newport ESP300) connecting to the computer program through a GPIB interface. The maximum traveling speed for the x-y stages is 2000 μm/s that is limited by their internal motors.

Regarding the focusing elements, a BK7 plano-convex lens (Thorlabs LA1986-B) with a focal length of 125 mm is used in most experiments. In addition, a 5X microscope objective (Newport M-5X) with a focal length of 25.4 mm is sometimes used so as to vary the laser spot size at the focus. To minimize the spherical aberration due to the lens, the laser beam must first enter the lens from curved surface, rather than from the flat one.

3.4 Diagnostic techniques of ultrafast laser pulses

It is known that for an ultrashort pulse, its pulse duration is inversely proportional to its spectral bandwidth. This relationship between the temporal and spectral domains

is fundamentally imposed by the uncertainty principle. That is to say, to obtain a shortest pulse duration for a given pulse shape, the spectrum bandwidth must be broad enough to satisfy the minimum duration-bandwidth product for that pulse shape. However, due to this broad spectrum containing wide range of frequency components, the ultrashort pulse becomes more susceptible to its propagating medium [1]. As demonstrated in Figure 3, the ultrashort laser pulses are delivered from the Spitfire output to the micromachining chamber after going through a relatively long beam path. After propagating through air and a few optics, such as lenses, mirrors, windows, the physical characteristics of the ultrashort laser pulses are likely to be altered, which in turn diminishes the reliability of the experiment [82]. Therefore, various effective techniques were employed to characterize and monitor the key properties of laser pulses before and during each experiment. They mainly consists of average power, spatial intensity distribution, spectrum, pulse width, etc..

3.4.1 Average power

To directly measure the average powers of the laser beam from both the Tsunami and the Spitfire, a thermal sensor (Ophir Optronics 1Z202146) was put to use because it can handle very high average power density (25 kW/cm^2 at maximum) without damaging the sensor. However, according to its specification, the noise level of the thermal sensor is relatively high, that is roughly 50 μW, so it is not suitable for measuring the attenuated laser pulse at low intensity under which most of the experiments are carried out.

Therefore, a power meter from Ophir Optronics was used to measure the average laser power after the Spitfire output beam passes through the attenuation line. It

consists of a silicon-based photodiode sensor (PD300-3W) and a NOVA universal power meter display. The sensor head is connected to the display through a plug-in RS232 adapter. To conduct the power calibration as well as monitoring the power fluctuation throughout each experiment, the power meter is also connected to an in-house computer program via the RS232 interface.

As an alternative approach for monitoring the laser power without repeatedly inserting the power meter, readings of the voltage corresponding to specific power levels were acquired by a multimeter that is linked to the computer program and a boxcar integrator. The computer program records both the power and voltage measurements while performing the power calibration.

3.4.2 Spatial intensity distribution

The spatial intensity distribution of the laser beam is often referred to the beam profile. For all experiments presented in this thesis, the beam profile was characterized by using a CCD-based beam profiler (Ophir Optronics, BeamStar). For the purpose of aligning the beam straight down to the sample chamber, the beam profiler was placed after the entire beam path and just above the chamber. By adjusting the optics along the beam path, one can confirm that the beam is not being clipped along the path. Apart from use for the alignment, the acquired 2-D images from the beam profiler can be recorded during each experiment. It provides a way to monitor the possible change in the spatial intensity distribution of the laser beam over a period of time.

3.4.3 Spectrum

In order to acquire the spectrum of the laser beam, a PC2000 PC plug-in spectrometers from Ocean Optics was routinely put to use. To confirm that there is adequate bandwidth in the seeding pulse from the Tsunami, the spectrum of the Tsunami output beam was measured using this spectrometer. The FWHM of the Tsunami beam is normally kept at 13 nm. The spectrum of the Spitfire output beam is also measured with the same spectrometer. A USB2000 spectrometer from Ocean Optics was particularly employed to obtain the spectrum of the 400 nm light after converting the 800 nm light via SHG using a BBO crystal. The reason for switching to the USB2000 spectrometer is because its detectable wavelength range covers from 200 nm to 1100 nm, whereas the PC 2000 can not measure the 400 nm wavelength.

3.4.4 Pulse width

The temporal profile is one of the most significant characterizations of the ultrashort laser pulses and plays a critical role in determining the laser interaction with the materials under irradiation. Thus, it must be experimentally verified with relatively high precision. However, because the typical rise time of a photodiode is in the range of 0.1 ns to 1 ns, that is far longer than the ps and fs laser pulses used in the experiments, the autocorrelation technique must be implemented so as to accurately determine the pulse width. In all the work presented in this thesis, the primary means to measure the pulse width is to use a second-order non-collinear autocorrelator. The setup of the autocorrelator is schematically shown in Figure 4.

The setup resembles closely to a typical setup of a Michelson interferometer. A 50/50 beam splitter divides the Spitfire output beam into two orthogonal beams with

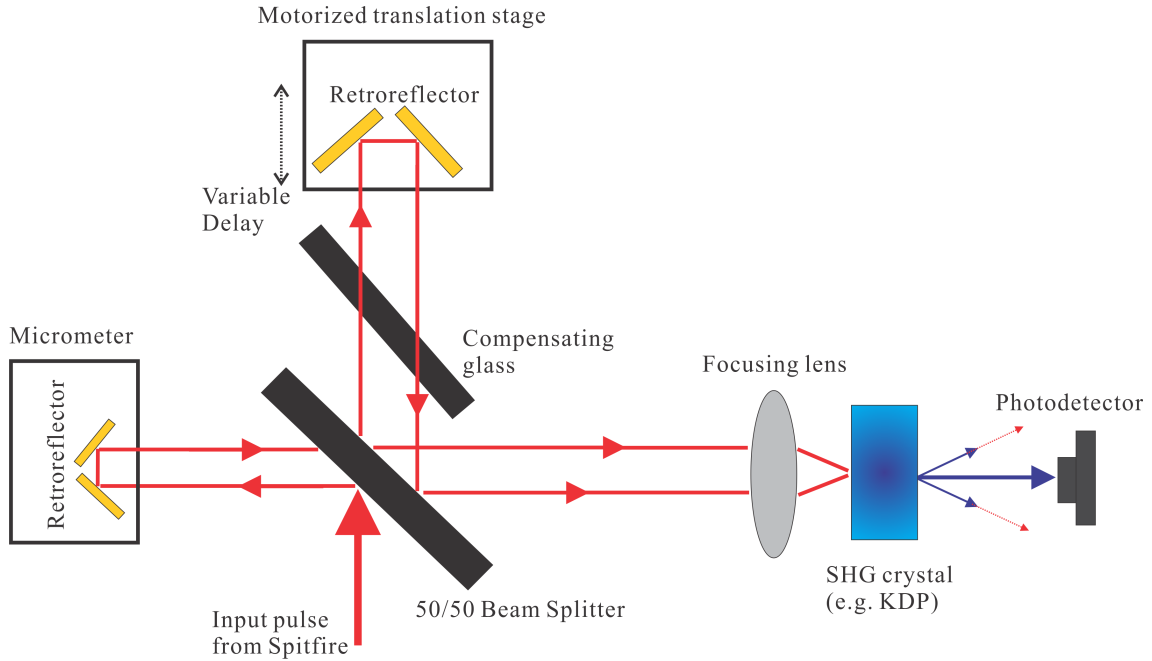

Figure 4: Schematic diagram of the second-order non-collinear autocorrelator used to measure the pulse width of the ultrashort laser pulses in the experiments.

equal optical powers. The reflected beam is directed to a retroreflector that is mounted on a micrometer. Due to the limited moving range on the micrometer, the optical path of this reflected beam can be considered fixed. The transmitted beam is then sent to another retroreflector that is secured on a motorized 1-D translation stage (Newport UTM100CC1HL). As the stage travels, it results in a difference in optical path length between the reflected and the transmitted beams, which in turn leads to a temporal delay between two beams. Each retroreflector is made of two gold mirrors that are also positioned orthogonally to each other. The use of retroreflectors is to ensure the two beams can get reflected in parallel, thereby facilitating the alignment procedure. After going through the beam splitter again, the two beams are focused through a converging lens onto a KDP crystal with a thickness of 500 μm. Blue light of $\lambda = 400$ nm is generated via SHG in the crystal [83].

The intensity of the central beam that contains the second-order interferometric correlation signal is detected and measured by an InGaAs photodiode. Then, the power readings from the photodiode are recorded by the computer as the motorized stage is moving within a preset scanning range. Based on the collected data on the laser intensity after one full scanning range, an autocorrelation trace can be obtained, and the pulse duration can then be calculated from this trace [84]. However, the exact value of the calculated pulse duration highly relies on the assumed input pulse shape [1, 85]. For all the experiments in this research, a Gaussian pulse shape was assumed and used as the input pulse shape.

Chapter 4

Sample analysis techniques and parameter extraction

4.1 Sample information and preparation

4.1.1 Si samples

The Si wafers used in the research were kindly provided by Professor Andrew Knights from the Department of Engineering Physics. They were purchased from Silicon Inc.. According to the manufacture specification, the Si wafers are p-type with (100) crystalline orientation. In addition, the wafer thickness is 550 $\pm$ 25 μm, and the electrical resistivity is in the range of 1 - 10 $\Omega\cdot$cm. A pristine piece of Si wafer was cleaved into many small fragments and served as actual Si samples for the experiments. The sample sizes were generally kept around 1 cm by 1 cm to fit into sample containers. Cleaving of Si samples was conducted on a lab table, and handling of the samples was performed in a regular lab environment. To remove any noticeable debris from the

cleaving process and dust from ambient environment, a high-pressure N_2 gas gun was employed to blow each sample a few times before putting the sample into a well-sealed sample container.

4.1.2 SiO_2-Si samples and their growth conditions

The SiO_2-Si samples used in the Eugene Hsu's experiments were prepared by Peter Jonasson who is a Laboratory Coordinator at the Department of Engineering Physics, and Thomas Jacob who was then a M.A.Sc. student of Dr. Andrew Knights. The targeted oxide thicknesses for the SiO_2-Si samples were 137 nm and 274 nm. The oxides were thermally grown in a furnace at Peter Jonasson's lab. The growth conditions for the samples are summarized below in Table 2.

With regard to handling and preparation for the SiO_2-Si samples used in my experiments, I strictly complied with the following precautions and procedures for each individual sample grown in a furnace, in order to ensure a good quality of oxide. Except for the SiO_2-Si samples with a targeted thickness of 25 nm, all the oxide samples were thermally grown in the furnace at Peter Jonasson's lab. First, I cleaved a piece of Si sample from a pristine Si wafer, which acted as the substrate for growing the oxide layer. The sample size was kept around roughly 5 cm by 5 cm, so that it can well fit into the furnace. Before oxide growth, the sample was cleaned by dipping it in buffered HF solution (a ratio of 10:1) for approximately 60 seconds to remove any surface contaminations which resulted from the handling procedures and other sources. Immediately following by the HF dipping, the sample was placed into the furnace whose temperature was already operating at 1000 °C in a wet environment. As listed in Table 2 below, the growth conditions for different oxide thicknesses were

evaluated and acquired through an oxide growth calculator that is based on the standard Deal-Grove model [8].

Oxide thicknesses (nm)	24	117	150	216	1000
Temperature (°C)	1100	1000	1000	1000	1000
Environment	Dry	Wet	Wet	Wet	Wet
Assumed native oxide thickness (nm)	2.0	2.0	2.0	2.0	2.0
Growth duration (hrs-mins-sec)	0-0-90	0-14-45	0-36-40	0-16-20	4-32-0
Equipment	RTA	Furnace	Furnace	Furnace	Furnace

Table 2: Growth conditions for the SiO_2-Si samples with different oxide thicknesses used in the experiments.

It is known that the Deal-Grove model fails to forecast reliable growth conditions for growing thin oxides that have a thickness less than approximately 20 nm - 30 nm because the grow rate in that regime follows a non-linear curve, rather than a linear-parabolic one [8, 86]. Initially proposed by Dr. Edgar Huante Ceron who is a post-doctorate from Professor Andrew Knights' group, the technique of rapid thermal annealing (RTA) was applied to grow the SiO_2-Si samples with a desired thickness of 25 nm. Compared to conventional thermal growth processing in a furnace, the RTA possesses advantages in more precise controls in processing time, as well as in uniformities of both temperature and oxide thickness [87]. The RTA equipment used for the oxide growth is a RTA furnace (Jetfirst 100, from Jipelec, Quanliflow Therm), courtesy of Dr. Andrew Knights. The growth procedure was fully automated and controlled by a computer software.

However, because there is no well-established theoretical model to predict accurate growth conditions for growing thin oxides using RTA, a proper growth condition for

growing the 25 nm thickness had to be experimentally explored, attained and verified through repeated growths in a trial-and-error fashion. The final growth conditions for this thickness are also summarized in Table 2. They may not be the optimal conditions for growing this thickness in the RTA furnace, but could consistently produce an oxide layer that has a thickness of approximately 25 nm with a reasonably slight fluctuation.

Because the oxide thickness is a very important sample parameter, it is necessary to determine the actual thickness of each oxide sample through different experimental techniques. In this research, the primary approach to measure the oxide thickness was the ellipsometry technique. The details of measurement procedures using an ellipsometer can be found in the Section of 4.2.1. The measured thicknesses and their experimental uncertainties for the oxide samples are summarized in Table 3.

Furthermore, direct measurements on the oxide thickness can be made through examining the cross-sectional TEM images of the sample. However, as it is not a trivial task to prepare TEM samples and acquire TEM images for all the oxide samples, this direct technique was only considered as an alternative means to verify the measurements obtained from the ellipsometry. The measured results based on the TEM images for the oxide samples with targeted thicknesses of 150 nm and 274 nm are also listed in Table 3. For the subsequent parts of the thesis, the measured oxide thicknesses will be explicitly referred as their true thicknesses, instead of the targeted thicknesses.

4.1.3 Inspection of sample surface

Prior to laser processing, sample surfaces of all the Si and SiO_2-Si samples were examined under either OM or SEM to check surface contaminations for any discernible

Targeted thickness (nm)	Measured thickness based on ellipsometry (nm)	Measured thickness based on TEM images (nm)
25	24 ± 5	-
117	116 ± 3	-
150	112 ± 4	-
150	158 ± 4	155 ± 3
274	216 ± 3	218 ± 4
1000	1013 ± 9	-

Table 3: Thickness measurements of the SiO_2-Si samples based on the ellipsometry technique and the cross-sectional TEM images. The uncertainties are the standard deviations of multiple measurements for the same sample that are taken at different locations on the sample.

artifacts existing on the surface, especially for the oxide samples. While observing each sample under OM and SEM, I scrutinized through the entire sample from one edge to the other at a relatively low magnification, in order to find the most seemingly contaminated regions on the sample. Then, I zoomed in on those regions and subsequently took images of several locations to assess dimensions and appearances of the contaminants. It may help to identify what they might be and their origins.

As an example, typical OM and SEM images of the sample surfaces for different oxide thicknesses are shown in Figure 5. The OM images in Figure 5 (a - c) show that the samples under observation are generally clean despite the fact that there are some black dots, possibly dust, at some locations. The yellow colour of these images are due to configuration of the optical filters on the OM and RGB setting of the image acquisition software. The SEM images in Figure 5 (d - f) clearly reveal more details of the surface.

Regarding to the 24 nm thick SiO_2 sample, the black dots appears to be much larger and more concentrated over entire surface. In addition, there are also some

black rod-like particulates on the sample. For the SiO_2-Si samples with oxide thicknesses of 112 nm and 150 nm, there are some subtle, but visible black dots dispersed on the surfaces. Considering that the major difference among the three samples is their growth equipment, one likely reason to cause the distinct surface contamination is that the 24 nm thick SiO_2-Si sample was grown in the RTA furnace, whereas the other two samples were grown in the regular furnace. As the RTA furnace is completely exposed to its surrounding environment, it is probable that the RTA chamber have accumulated substantial amount of contaminants that were transferred to the 24 nm thick oxide sample during the growth. By comparison, the furnace is a well-sealed container that is isolated from the surroundings. The oxide samples grown in the furnace are consistently free of sizeable contaminants, unlike the 24 nm thick sample.

4.2 Sample analysis techniques

4.2.1 Ellipsometry

A fixed-wavelength ellipsometer (Philips PZ2000) in the Center for Emerging Device Technologies (CEDT) at McMaster University was extensively used for measuring the oxide thicknesses of SiO_2-Si samples. The light source in the ellipsometer is a HeNe laser with a fixed wavelength of 632.8 nm. According to its specifications, the ellipsometer is not sensitive enough to yield a reliable measurement for a single-layer film with a thickness less than 20 nm. The refractive indices of SiO_2 and Si at the $\lambda =$ 632.8 nm were taken as 1.465 and 3.865, respectively, as initial input parameters for the data acquisition software. Because the software uses the negative-sign convention

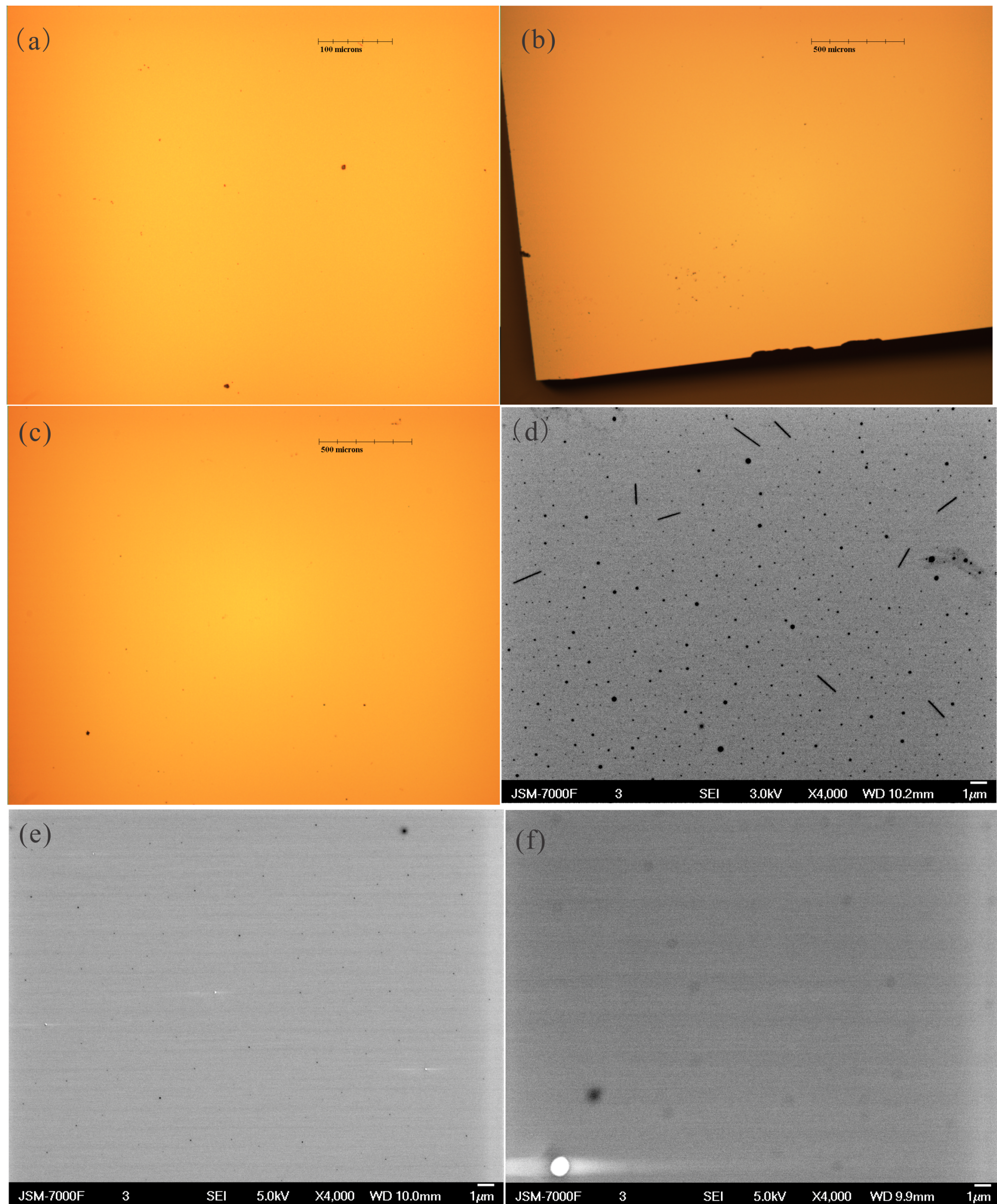

Figure 5: OM and SEM images of Si and SiO_2-Si samples taken prior to laser irradiation. (a) OM image of the bulk Si sample; (b) OM-image of the 24 nm thick SiO_2-Si sample; (c) OM-image of the 1013 nm thick SiO_2-Si sample. (d) SEM image of the same 24 nm thick SiO_2-Si sample; (e) SEM image of the 112 nm thick SiO_2-Si sample; (f) SEM image of the 150 nm thick SiO_2-Si sample.

for extinction coefficients, the extinction coefficients of SiO_2 and Si at the $\lambda = 632.8$ nm were set at 0 and - 0.02, respectively.

Before taking actual measurements on my oxide samples, I always first measured a calibration SiO_2-Si wafer that has a specific oxide thickness and a known uncertainty, so as to ensure that the ellipsometer operates at its normal conditions. I maintained my measurement procedures as consistent as possible for each oxide sample. I made at least three repeated measurements at a certain area of the sample. Once the measured thickness was proven to be consistent for that particular spot, I recorded the last value, and then continued the same procedure at other regions of the same sample.

Because each oxide sample has similar size, I generally divided each sample into four or five regions of which three of them were around the centre of the sample and two of them were at each corner. Therefore, in the end, there were four or five thickness measurements for each sample, which entirely cover the sample. The average value of those measurements was calculated and taken as the final thickness for the sample. The standard deviation of the measurements was also evaluated. It provided a way to examine the overall uniformity of the oxide layer. All the ellipsometry measurements are summarized in Table 3 above.

4.2.2 Atomic force microscope (AFM)

Owing to its atomic resolution in measuring both lateral and vertical dimensions of surface features, AFM is a key characterization tool to yield high-precision information on surface topography [88]. All the AFM work, including equipment setup and image acquisition were done by Dr. Jessica Carvalho who is a post-doctorate fellow

in Professor John Preston's group. The AFM equipment used in this thesis is the Caliber (TM) system from Veeco. According to its manufacture specifications, the maximum scanning range in the z-direction is typically 10 μm. The noise floor along the z-direction is less than 0.15 nm in tapping mode at 1 kHz sampling bandwidth. This noise level contributes to part of the errors in the actual measurements of height profiles.

All of the AFM scanning was carried out in tapping mode. The key reason to run in tapping mode, instead of contact mode, is to avoid any potential damage to the sample surface that are due to the constant downward forces from the tip when operating in contact mode, even for rigid Si samples. In contrast, in tapping mode, the AFM tip-cantilever assembly oscillates above the sample surface while the tip is rastering across the sample. A constant distance between the tip and the sample surface is preserved by maintaining a constant oscillating amplitude, thus preventing any direct physical contact [89].

Because the AFM was shared by other researchers and students, exchange of the AFM tips happened quite frequently. It was impractical and time-consuming to change back to the exactly same tip that was employed the first time on different days of taking the measurements. However, all the tips are quoted to have original radius around 20 nm. Yet, depending on the consumption of each tip, the actual dimension may differ from one another. The AFM data in ASCII format were processed and analyzed by using the software: scanning probe image processor (SPIP, Version 5.0) from nanoScience.

4.2.3 Optical microscope (OM)

An optical microscope (Zeiss upright light and stereo microscope) was used as an initial step to examine samples both before and after laser irradiation thanks to its free and easy access. The images were taken from a CCD camera accompanying with an image acquisition software (Northern Eclipse). During September 2012, the CCD camera was updated to Clemex CCD camera, together with a package software (Clemex Vision Lite). The OM images provide overall surveys of the samples and help to identify the most interesting regions on the samples that are worthy of being further investigated under SEM. The OM is normally operated in bright-field reflected light mode in order to observe discernible surface features, such as LIPPS, craters, dirt, on the samples.

To reveal as many details as possible from this microscope, its maximum magnification was most frequently in use. It was achieved by applying a 100X objective together with an additional 2.5X magnification lens. However, according to the Rayleigh criterion, the best resolution of an typical optical microscope that is normally around 0.2 μm is fundamentally limited by the wavelength range of the light source, in addition to the numerical aperture of the lens for an OM [90].

The Nomarski differential interference contrast (DIC) mode has the advantage of showing subtle variations in height of the features, thus improving the sharpness of their edges with better imaging contrast. As a result, the DIC mode was extensively employed for observing the samples with ripple structures whose height profiles otherwise appear to be much less prominent under normal imaging mode.

The calibration of the scale bars stamped on acquired OM images at different magnifications was automatically performed by the acquisition software. To verify

this calibration and compare its accuracy with other analysis techniques, such as SEM and AFM, a straight line with a fixed length of 1 mm was marked using the laser beam at a corner of each sample after irradiation. Then, the line was imaged under the OM. Later on, the actual length of each calibration line were measured using CorelDraw. The measurements confirmed that the calibration of the scale bars was quite accurate and consistent at all magnifications for all acquired OM images.

4.2.4 Scanning electron microscope (SEM)

Because of its advantages over OM, such as superior imaging resolution and large depth of field, the SEM was a principal tool in this research to examine the surface quality of samples before laser processing, as well as the surface features, mainly the ripples, created on the samples after laser irradiation. The majority of the SEM work was performed with the JEOL 7000 field-emission SEM, together with an image acquisition software. The early SEM work from Eugene Hsu's experiments was carried out with the Philips 515 SEM, and an image acquisition software called UltraRapid Spectral Analyzer by Mekteck. All the SEM images were acquired in secondary-electron (SE) imaging mode that uses a SE detector to mainly reveal the morphology of the sample surface.

Depending on the acceleration voltage of the electrons, the finest resolution on the order of 10 nm can be easily achieved in most SEM at present. Even though the electrical conductivity of Si is fairly good, the accelerating voltage used for imaging is often maintained at a low value in the range of 5 to 10 keV in order to avoid significant charging effects and surface contamination from the carbon deposition on the surface. For the SiO_2-Si samples, a low accelerating voltage of 5 keV is mostly

employed due to the poor conductivity of the SiO_2.

Because typical dimensions of the surface features, e.g. LIPSS on the samples are on the order of 100 nm, the required magnifications for capturing enough details are not very high, which vary between 3000 to 15000 times. As a result, a working distance of 10 mm and a medium level of probe current were largely applied. The tilt angle is always set at zero degree. During each SEM session, the calibration line with a fixed length of 1 mm that was cut on each post-processing sample was imaged. Its actual length was then measured in CorelDRAW. The same routine was also carried out for the OM images, as mentioned in 4.2.3.

4.2.5 Transmission electron microscopy (TEM) and focused ion beam (FIB) technique

All the FIB and TEM work presented in this thesis was carried out at the Canadian Center for Electron Microscopy (CCEM) at McMaster University. Julia Huang, a staff member at CCEM was a primary contributor to the FIB work, and Dr. Andreas Korinek, a research associates at CCEM performed the TEM operations, including image acquisition, x-ray diffraction analysis, and energy-dispersion x-ray (EDSX) analysis. By means of the FIB milling procedure, a TEM specimen was acquired by slicing off a piece of oxide sample around the central regions of the ripples. The specimen contains an entire layer of SiO_2-Si and a layer of part of the Si substrate. The model of the FIB instrument is Zeiss NVision 40.

After the TEM specimen was prepared, it was first imaged under an analytical TEM (Philips CM12) operating at 120 keV. The TEM images provide a preliminary survey about the nature of the sample in terms of its overall layered structure, and

the relative dimensions of all the layers made of different materials. A further TEM examination of the specimen was conducted in a high resolution TEM (HRTEM) with a model number of Titan 80-300LB from the FEI Company. It is incorporated with an energy-dispersive x-ray spectrometer, which was employed to help identify the elemental composition of the TEM specimen.

4.3 Parameter extraction

4.3.1 Extraction of incident laser spot size

The most direct technique to measure the spot size of a laser beam is to use a CCD beam profiler. But, as the minimal size of a typical pixel on a regular CCD detector is limited in the range of 10 - 20 μm, this technique will result in larger uncertainty when measuring tightly focused beams whose diameters are close to or much less than the size of a single pixel. Although some major optics vendors, such as Duma Optronics, Thorlabs, Newport, offer high-resolution CCD beam profilers that are specially designed for measuring the spot size down to 10 μm, they are generally very costly. Another common technique to determine the spot site is referred as to knife-edge measurement. However, the difficulty of ensuring that the scanning plane matches perfectly with the sample surface while making the measurements, makes this method very impractical to apply. Moreover, both techniques mentioned here suffer from causing potential damage to the CCD detector or the knife-edge when the pulse energy used is high, which rarely occurs in practice.

The technique extensively used in this thesis for measuring the spot size is referred as the "D^2" technique that was initially developed to provide a simple way to

experimentally determine the spot size of laser pulses with a Gaussian spatial profile [91]. Based on the empirical correlation of the laser-induced material modification in terms of forming rim features, referred to as craters, with the Gaussian spatial intensity distribution, the spot size can be found through the following equations [69]:

$$D^2 = 2\,\omega_o^2\,\ln\left(\frac{\phi_o}{\phi_{\mathrm{th}}}\right) \tag{6}$$

where D is the measured diameter of an laser-induced crater; ω_o is the spot size defined as the spatial radius at $1/e^2$ of peak intensity; ϕ_o denotes the peak laser fluence in [mJ/cm^2] at the centre of a Gaussian spatial profile; ϕ_{th} is the threshold fluence of a certain material, in [mJ/cm^2];

The peak fluence ϕ_o can be obtained from its direct relation with the measured pulse energy E_{pulse}, such that:

$$\phi_o = \frac{2\,E}{\pi\,\omega_o^2} \tag{7}$$

Thus, equivalently, equation 6 can be expressed in terms of the pulse energy as:

$$D^2 = 2\,\omega_o^2\,\ln\left(\frac{E_{pulse}}{E_{\mathrm{th}}}\right) \tag{8}$$

where E_{pulse} is the pulse energy that is directly obtained via measuring the incident optical power at a fixed repetition rate using a power meter; the E_{th} is the threshold energy.

Regarding the procedure of conducting the D^2 measurements, a row of craters was produced at different laser powers on a bare Si sample. Then, the craters were

imaged under OM in DIC mode. As most of craters are not perfectly circular showing some degree of ellipticity, the diameters of each crater along the horizontal axis and along the vertical axis were measured altogether. The geometric mean of both measurements was evaluated as the final value of D. According to the equation 8, the spot size can be calculated by linearly fitting the plot of D^2 against the $\ln(E)$. Such linear curve fittings with corresponding plots for two most frequently used lenses are shown in Figure 6, in order to show typical results for the D^2 measurements.

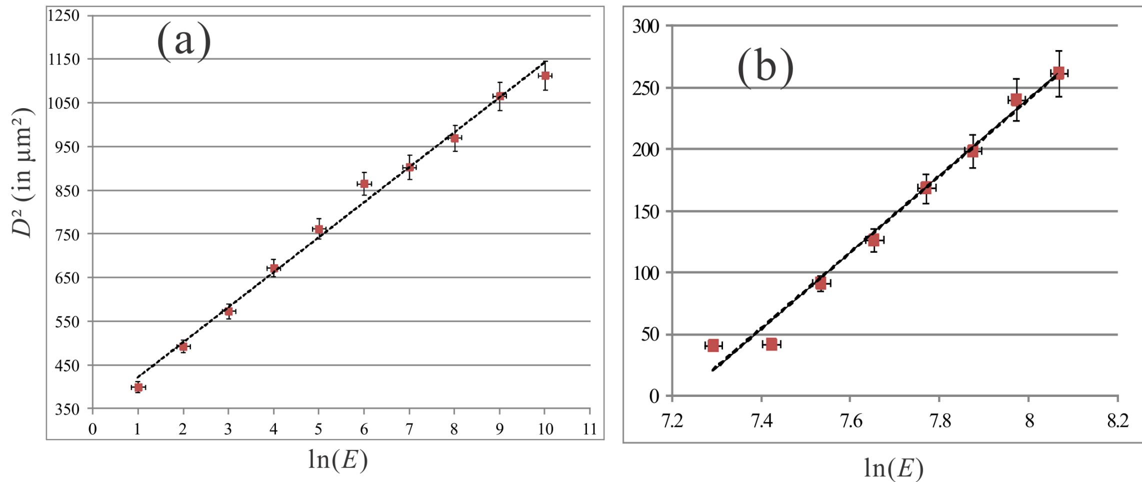

Figure 6: Plot of D^2 against the $\ln(E)$ for a typical single-shot D^2 measurement. (a) for the Thorlabs 125 mm lens, the measured spot size is 19.5 ± 0.9 μm at $\lambda = 800$ nm; (b) for the Newport 5X microscopy objective lens, the measured spot size is 4.4 ± 0.7 μm at $\lambda = 800$ nm.

Based on the linear fitting of the plot, the laser spot size can be extracted from evaluating the square root of the line's slope (including the a factor of 2). In addition, the intercept (including the a factor of 2) of the line with the x-axis (ln(E)) can be used to extract the threshold pulse energy E_{th} that is required to create the observed feature on that specific material.

4.3.2 Extraction of the effective number of laser pulses in translational motion

For all the experiments present in this thesis, the samples were irradiated by a translating laser beam. In other words, by moving the sample at a specific speed in either the x- or y- direction, the laser beam linearly scans across the sample surface. Considering the change in the spatial overlapping of subsequent laser pulses, the difference in the number of laser pulses at a specific site for translating irradiation must be taken into account, when compared with the case of stationary irradiation. Assuming a 2-dimensional Gaussian intensity distribution for the laser pulse characterized by a spot size ω_o and a peak fluence ϕ, the effective number of laser pulse at a particular spot can be estimated as [92]:

$$N_{eff} = \sqrt{\frac{\pi}{2}}\,\frac{\omega_o\, f}{\upsilon} \tag{9}$$

where N_{eff} denotes the effective numbers of laser pulses at a given region enclosed by the laser pulse; ω_o is the spot size in [μm] of the incident laser beam that is taken as the radius at $1/e^2$ of the peak intensity; f is the laser repetition rate in [Hz]; υ is the translation speed of the laser beam, normally in [μm/s]. Regarding the origin of the correction factor of $\sqrt{\frac{\pi}{2}}$, it can be referred to the reference [92].

Chapter 5

Results and discussion

5.1 Laser irradiation using femtosecond pulses at 800 nm wavelength

5.1.1 Experimental details

For all the experiments mentioned in the following, the Ti:Sapphire laser system that was described in Chapter 3 operated at a peak wavelength of 800 $\pm$ 3 nm with a measured FWHM linewidth of 10 nm. A fixed repetition rate of 1 kHz was always maintained as well. Depending on different experiments, the measured pulse durations varied within the range of between 141 fs and 184 fs. The specific value of the pulse width will be explicitly provided for an individual sample. A BK7 plano-convex lens (Thorlabs LA1986) with a focal length of 125 mm was used to focus the laser beam onto samples through a 1-mm thick window. For this lens, a spot size of 19.5 $\pm$ 0.9 μm (at $1/e^2$ radius) was extracted at the time of my experiments based on the D^2 technique [69], whereas for Eugene Hsu's experiments, a spot size of 17 μm (at $1/e^2$

radius) was measured at the time of his experiments.

The experiments were all conducted in a rough vacuum environment at room temperature, which is around 40 - 60 mTorr. All the samples under laser irradiation were translated by moving motorized stages relative to a stationary laser beam. The translation directions used consist of both x- and y- directions that are parallel to and perpendicular to the polarization of the incident E-fields, respectively. Four different translation speeds were regularly used, including 100, 500, 1000 and 2000 μm/s. According to the equation 4.3.2 in Chapter 4, the numbers of effective laser shots on a given location for the four speeds were calculated using a spot size of 19.5 μm. Their values are 244, 48, 24 and 12 that are in accordance with increasing speeds.

5.1.2 Ripples formed at the SiO_2-Si interface

Observation of the ripples prior to removing the oxide layer

Both DIC-OM and SEM images in Figure 7 show that there are very distinct periodic structures, referred to as ripples that have been produced on the SiO_2-Si sample after it was processed under laser irradiation. The spatial periodicity of the ripples was evaluated to be around 705 nm by directly measuring their dimensions in the images. The SiO_2-Si sample has an oxide thickness of 216 nm that is verified by multiple ellipsometry measurements. The displayed site was translated at 2000 μm/s along the y-direction that was perpendicular to the polarization of the E-fields. When Eugene Hsu was conducting the experiments, he measured a pulse duration of 156 fs and used the same 125 mm focus lens. As the incident laser energy for forming the ripples was measured at 0.906 μJ, the corresponding peak fluence was calculated at 200 mJ/cm^2 using the known spot size of 17 μm for this lens.

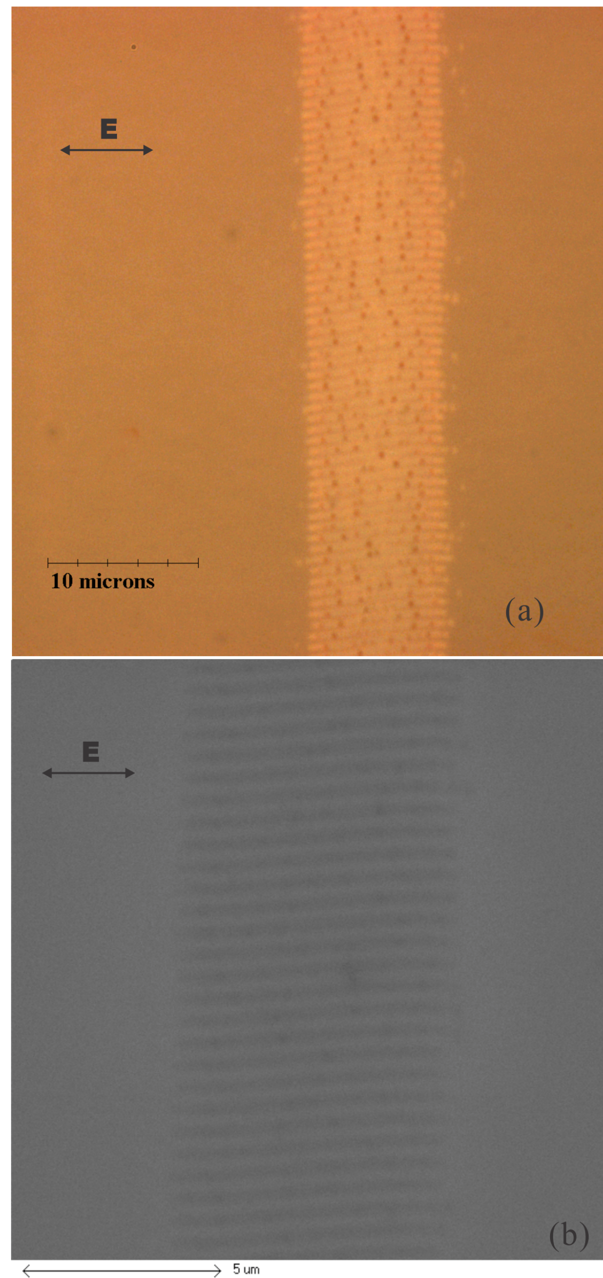

Figure 7: Observation of the ripples on the SiO_2-Si sample with an intact 216 nm oxide layer. (a) DIC-OM image; (b) SEM image (Obtained in the SEM Philips 515). The 216 nm SiO_2-Si sample was irradiated at $\lambda = 800$ nm with a laser energy of 0.906 μJ (a peak fluence of 200 mJ/cm^2), and translated at a speed of 2000 μm/s along the y-direction.

By comparing the regions that contain the ripples with their surroundings not processed by the laser beam, the sample surfaces appear to maintain their overall flatness and integrity in both regions. In particular, judging from the barely discernible image contrast on the SEM image in Figure 7, the surface topology strongly suggests that the oxide layer in the irradiated areas still remains completely attached to the Si substrate beneath it. Naturally, it then can be suspected that the ripples are formed under the oxide and most likely on the Si substrate. Additionally, it is known that Si has a linear absorption depth of 0.1176 μm at $\lambda = 800$ nm [74], whereas the SiO_2 is completely transparent at this wavelength owing to its large bandgap energy (9.0 eV). As a result, the majority of the incident laser energy is absorbed and deposited into the Si substrate. It primarily results in the formation of ripples at the SiO_2-Si interface while the oxide layer stays mostly untouched.

Several comments can be made though careful examinations on the appearance of the ripples. First of all, the ripples do not seem to be very straight, but rather look somewhat wavy extending from one end to the other. Their overall widths are measured to be approximately 9 $\pm$ 2 μm. When comparing this value with the spot size of 17 μm (at $1/e^2$ radius) for the Gaussian spatial intensity distribution, it means that only about a 27% part of the whole spot-size diameter has adequate intensities to contribute to the creation of the ripples. Furthermore, in Figure 7 (a), there are dark-brownish dots dispersed along the ripples. Because the SEM Philip 515 is an old instrument with very poor resolution, the dark dots look much less discernible and prominent in the SEM image, but they are still visible as black dots along the ripples. Limited by its resolution, OM can not reveal more details of the ripples beyond what is shown in Figure 7 (a). In addition, as it blocks the secondary electrons from

penetrating through when the sample is imaged under SEM, the oxide layer must be removed so as to acquire more intricate information regarding the ripple structures.

Observation of the ripples after removing the oxide layer

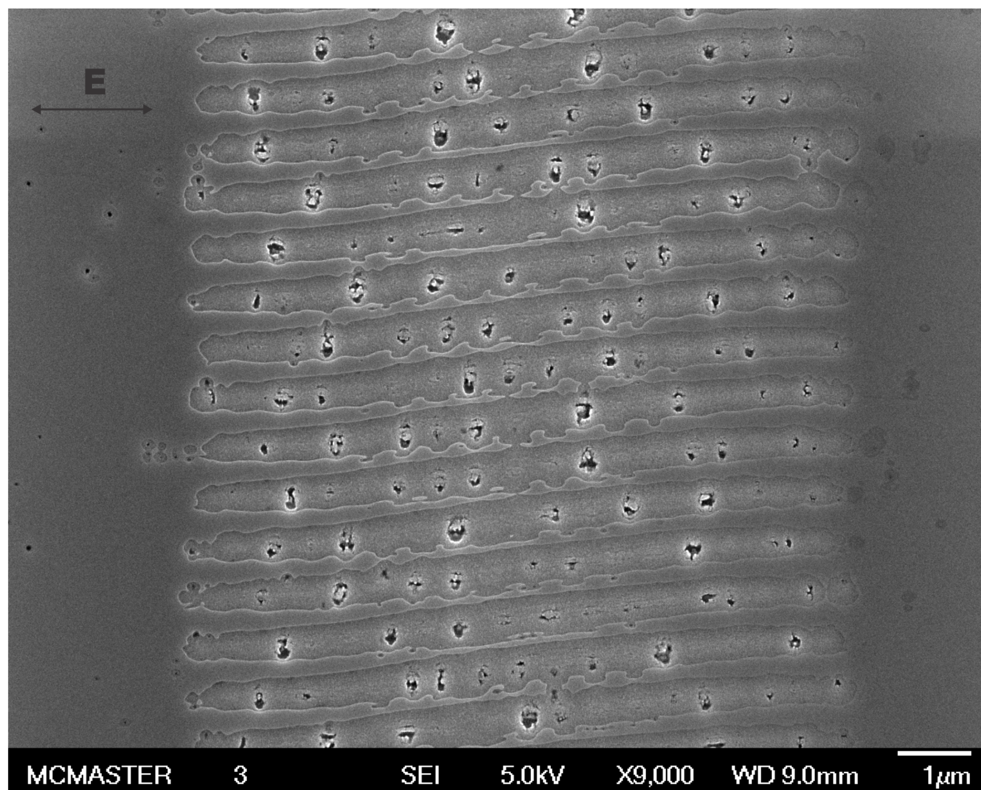

Figure 8: SEM image of the ripples on the Si substrate after the oxide layer was removed using HF solution. It is the same sample as the one shown in Figure 7, and its laser irradiation conditions can be found above.

Chemical etching using HF solutions was chosen to remove the SiO_2 layer without affecting the Si. Thus, further examinations on the ripples underneath the oxide layer can be pursued. The etching procedure was performed in a facility of CEDT and supervised by Dr. Doris Stevanovic. The SiO_2-Si sample that was shown in Figure 7 was cleaved into two specimens with similar sizes. One of the two specimens

was preserved for future FIB/TEM analysis. The other one was placed into 10:1 buffered HF solutions that was directly purchased from a commercial vendor. The quoted etching rate of this solution for removing SiO_2 at room temperature is 50 nm/min. As the oxide thickness of the sample was 216 nm, the sample was left in the HF solution for around 6 minutes at room temperature to ensure that complete removal of the oxide was achieved. After rinsing the etched sample with deionized water to get rid of residual HF solution, the sample was dried and cleaned with a N_2 gas gun.

Figure 8 shows the detailed appearance of the ripples on the Si substrate after the HF etching procedure. There are many pits scattered along the ripples. They are identified to be the dark-brownish dots in the DIC-OM image, as well as the faint black dots in the SEM image in Figure 7. Even though the detailed structure of the ripples is able to be brought into light by simply etching away the oxide layer, it also raises a question as to whether what has been observed here in Figure 8 is entirely caused the laser processing or somehow altered during the HF etching process.

AFM measurements

Both of the same samples, illustrated in Figure 7 and 8 were also examined by the AFM technique, which was to provide direct and quantitative measurements on the surface topology of the samples. Multiple AFM images and assessments were acquired for the SiO_2-Si samples both before and after the HF etching procedure. However, as there is no noticeable discrepancy among the outcomes, typical AFM results of each sample are selected and displayed in Figure 10. The ripples in the AFM images seem to be tilted because the samples were purposely rotated at a certain angle when

carrying out the AFM scanning. The scanning range for both AFM images is the same, that is 7.5 μm by 7.5 μm. The big black dots and white dots in Figure 10 (a) and (b) were identified to be dust on the sample surfaces. To make a more evident comparison between the two sample surfaces, especially in terms of the ripple structure, 3-D representations of the 2-D AFM images are demonstrated in Figure 11.

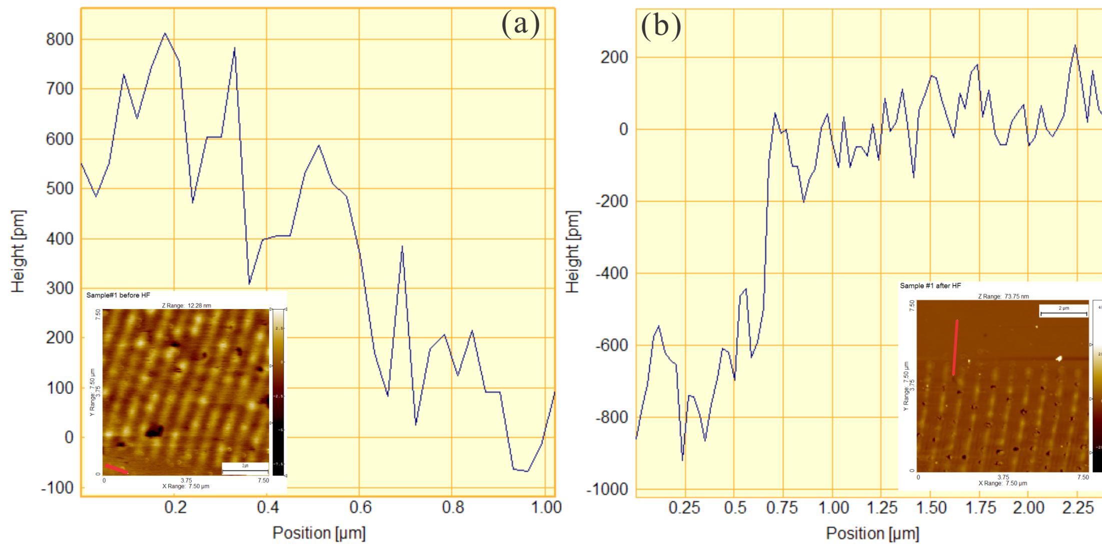

Figure 9: Height profiles of the flat regions near the ripples on the SiO_2-Si sample. (a) Height profile of the SiO_2-Si sample before HF etching (the sampled regions are indicated in the enclosed AFM image at the left-bottom corner); (b) height profile for the Si substrate after SiO_2 is removed using HF etching (the sampled regions are indicated in the enclosed AFM image at the right-bottom corner).

A height profile of the ripples was sampled on a particular location of each sample, and evaluated using the SPIP software. According to the height profiles, the ripples on the SiO_2-Si sample with an untouched oxide layer have an average height of approximately 0.8 nm. In contrast, after the oxide layer was removed, the ripples on the Si have an average height of 4.5 nm. Figure 9 shows that the height profiles

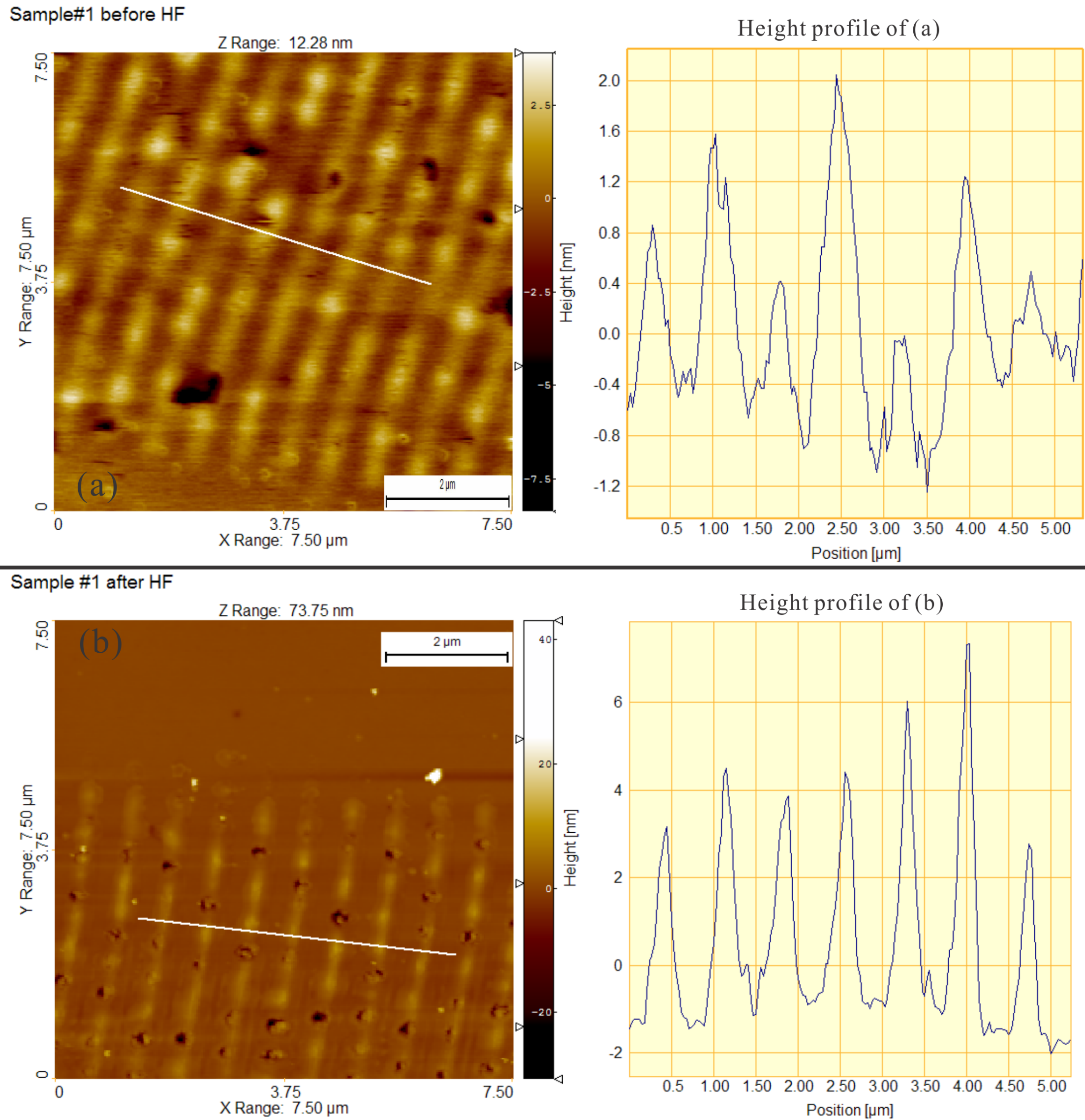

Figure 10: AFM measurements of the SiO_2-Si samples with a 216 nm thick oxide layer. (a) AFM topographic image of the 216 nm SiO_2-Si sample with an intact oxide layer, together with its corresponding height profile (right) for a sampled location, indicated by a white line; (b) AFM topographic image of the SiO_2-Si sample after the oxide layer was etched away using HF solution, together with its corresponding height profile (right) for a sampled location, indicated by a white line. The samples in (a) and (b) are exactly the same samples as shown in Figure 7 and 8, respectively.

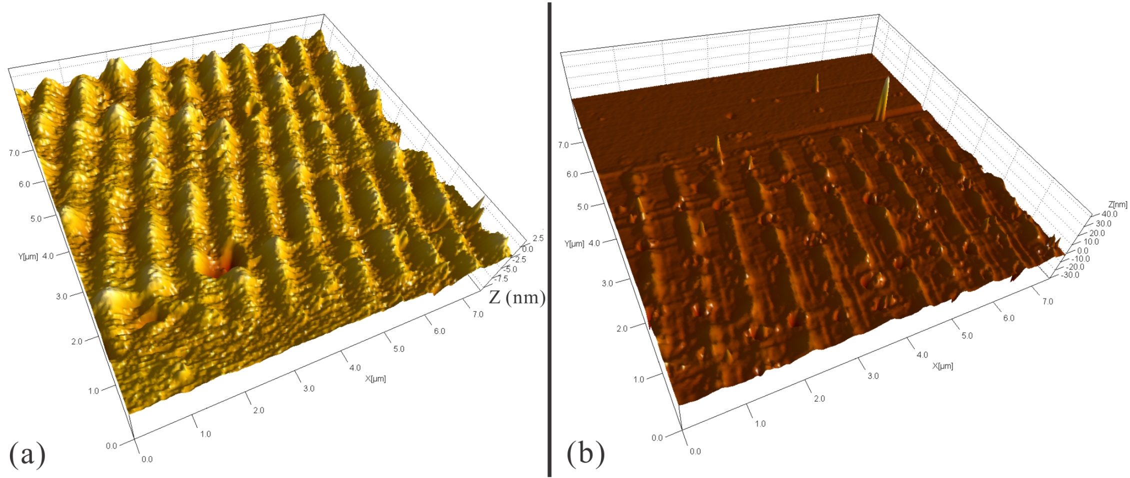

Figure 11: 3-D representation of the AFM topographic images. (a) The SiO_2-Si sample with a 216 nm thick oxide layer before HF etching; (b) the Si substrate after the oxide layer of the SiO_2-Si sample with a 216 nm thick oxide layer was etched away. The scanning ranges of (a) and (b) are 7.5 μm by 7.5 μm.

for the regions that were not covered by ripples for both unetched and etched SiO_2-Si samples. The height measurements indicate that the sample surfaces near the ripples are very flat with an average height of less than 1 nm for both samples. The ripple periods for both samples are measured to be very close, which are around 710 nm from peak to peak.

Like in the SEM images, the pits can also be observed in the AFM images, but they become more conspicuous after the oxide layer was removed. Based on the height profile in Figure 12 (b), the average depth of the three sampled pits is evaluated to be around 15 nm. The diameter at the FHWM of the pits is around 63 nm. Thus, it leads to an aspect ratio of roughly 4.2 (63:15) for the pits.

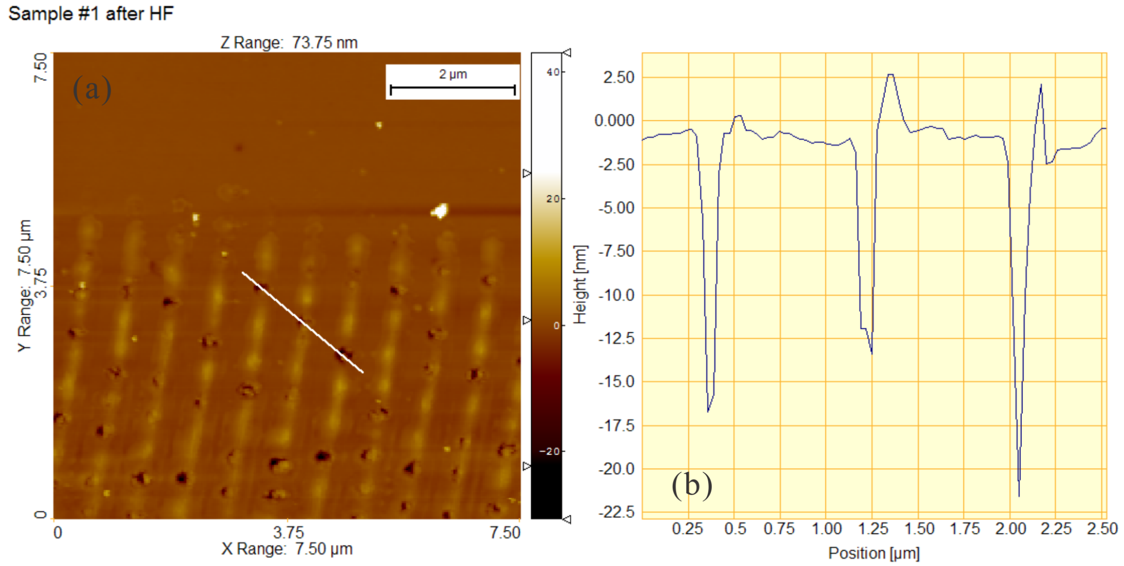

Figure 12: AFM measurements of the pits along the ripples on the etched SiO_2-Si sample. (a) AFM topographic image; (b) the corresponding height profile for the three sampled pits, indicated by a white line in (a).

TEM analysis

As mentioned previously, part of the original sample shown in Figure 7 was preserved for FIB/TEM analysis. From the preserved sample, a TEM specimen was obtained by slicing a strip of the ripples around their central regions using the FIB technique. Prior to the FIB operation, the surfaces of the chosen regions were coated with two protective layers that are a thin layer of platinum with a thickness of roughly 20 nm, and a much thicker layer of carbon with a thickness of roughly 1.5 μm, so that any potential damage to the irradiated areas can be minimized during the ion-milling procedure.

Figure 13 (a) shows bright-field cross-sectional TEM images of the FIB-prepared specimen. While acquiring TEM images, the specimen was purposely oriented at a tilted angle, which leads to the images not looking completely straight along neither

the vertical nor horizontal axes. The outermost part can be identified as the protective carbon layer. The black thin line adjacent to the carbon layer is the protective platinum layer. The smooth band next to the platinum layer is recognized as the oxide layer. Based on the ellipsometry measurements, the measured thickness of the oxide layer on the FIB specimen is 216 nm. From this TEM image, the thickness of the SiO_2-Si layer is directly measured at 218 nm, which agrees well with the ellipsometry measurements. The majority of the specimen is composed of crystalline Si substrate containing curved stress lines that can be identified by the dark bending lines running all the way to the SiO_2 layer.

The ripples as shown in Figure 13 (a) can be clearly discerned as periodically modulated materials in the Si substrate. They appear to be small bumps with similar dimensions extending roughly 78 nm in depth into the Si. The spatial distance is measured at 720 between two adjacent bumps at their peaks. The overall SiO_2 layer does not seem to be modified in any way, which confirms that the oxide layer remains fairly untouched after laser irradiation. There are nine ripples captured in this TEM specimen. Eight out of the nine ripples are solid, filled with nano-crystalline Si. Only a single ripple is partially solid and partially occupied with voids that can be distinguished by the white colour.

Figure 13 (b) shows the magnified view of the ripple with voids. There is a black line separating the ripple from the Si substrate. Upon a closer look, the uneven boundary between the SiO_2 layer and the ripple suggests that there does exist very subtle modifications to the structure of the SiO_2, which are likely to be caused by the melting Si. However, compared to the dimensions of the ripples, this material modification is restricted to a very shallow layer of oxide that can only be noticed at

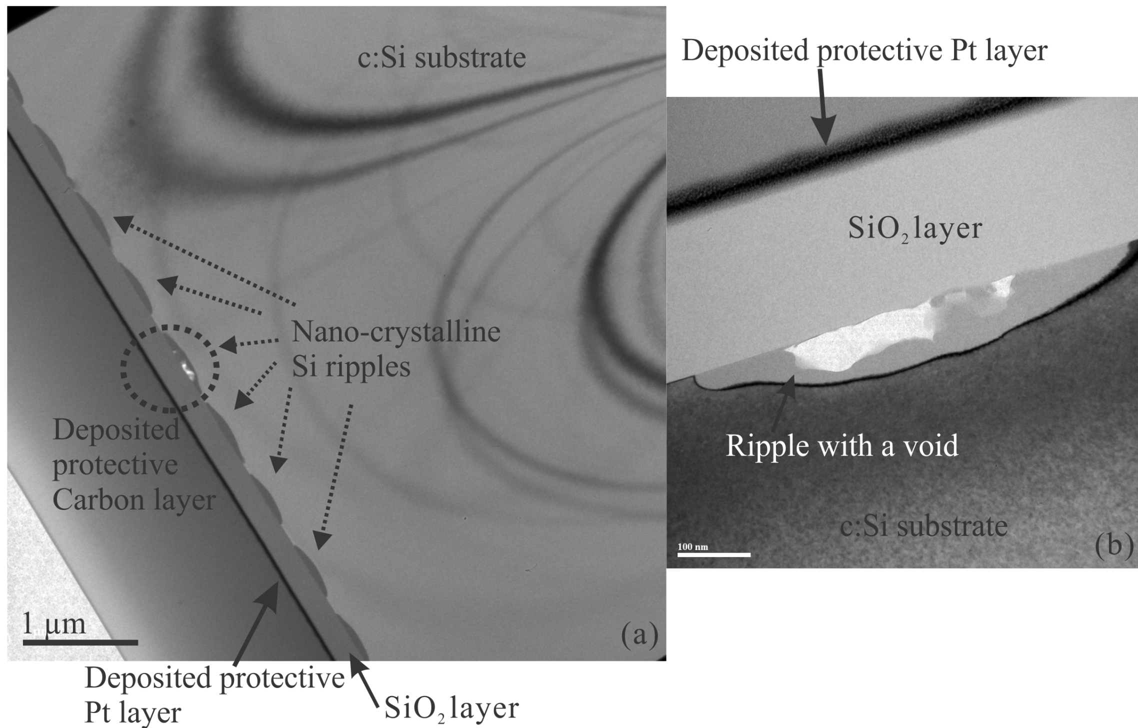

Figure 13: Cross-sectional bright-field TEM images of the FIB-prepared SiO_2-Si specimen with an intact 216 nm oxide layer. (a) Overall view of the cross-section containing several ripples; (b) magnified view on the ripple with voids (highlighted by a dotted circle in (a)). Note: different material compositions are explicitly labelled in the images, and c:Si stands for crystalline silicon.

a high magnification.

Further investigations on the material properties of the created ripples were accomplished by high resolution TEM (HRTEM) and EDX analysis. A bright-field HRTEM micrograph of one of the ripples is displayed in Figure 14 (a). There is a distinct bright curve that defines a transitional region between the Si substrate and the ripple. In addition, a faint straight band can be viewed between the ripple and the SiO_2 layer, which also establishes a clear boundary between the two different material compositions. Judging from the image contrast that largely results from the crystalline structure of the imaging materials, the crystallinity of the ripple can be

determined as nano-crystalline with crystallite sizes on the order of a few nanometers.

Electron diffraction patterns (EDPs) for the Si substrate, the ripple and the SiO_2 are, separately, illustrated in Figure 14 b-1, b-2, and b-3. The diameter of the electron beam is on the order a few nanometers, so it is small enough to get focused entirely on the ripple. By comparing the EDPs between the Si (b-1) and the ripples (b-2), the major distinction is that there are about four distinguishable concentrical rings in the ripple's EDP. In contrast, the EDP of the oxide layer exhibits no sign of any rings verifying the amorphous nature of its crystallinity. Therefore, the rings show that the ripples possess a certain degree of crystallinity. It also confirms that the crystalline structure of the ripple is nano-crystalline that is an intermediate structure between the crystalline and the amorphous. As a complementary approach to help identify the material crystalline structures, dark-field TEM results with clear indications for different material compositions are shown in Figure 15.

To further verify the elemental compositions of different regions, particularly of the ripples, EDX was performed after the TEM analysis was completed. As indicated by a dotted circle in Figure 15, one of the ripples was chosen and sampled by the EDX. To provide accurate sampling locations on the chosen areas, a dark-field TEM image at higher magnification was provided with proper labelling in Figure 16 (a). The acquired EDX spectra corresponding to the oxide layer and the ripple are shown in Figure 16. With respect to the spectrum of the SiO_2-Si, two distinctive peaks are clearly present, which are associated with oxygen and silicon.

However, in the spectrum of the sampled ripple, the oxygen peak disappears while the silicon peak can still be seen. It substantiates the previous finding obtained from the HRTEM micrographs regarding the elemental composition of the ripple, which

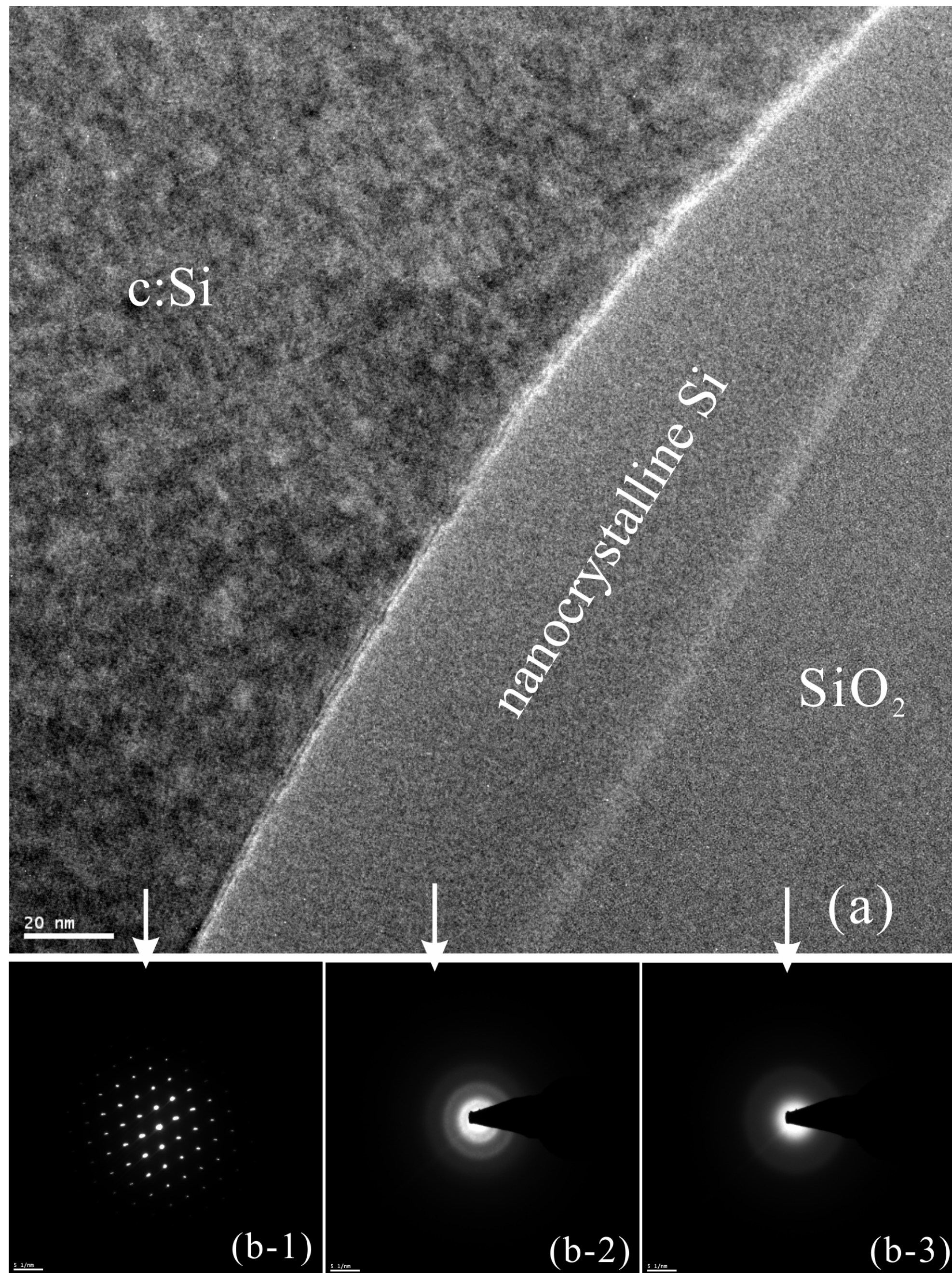

Figure 14: Bright-field high-resolution TEM micrograph (HRTEM) of the central regions of the ripples in the SiO_2-Si sample with an intact 216 nm thick oxide layer. (a) Bright-field HRTEM micrograph of the central regions of a ripple; (b-1) EDP of the crystalline Si (c:Si) substrate; (b-2) EDP of the nanocrystalline ripple; (b-3) EDP of the amorphous SiO_2 layer.

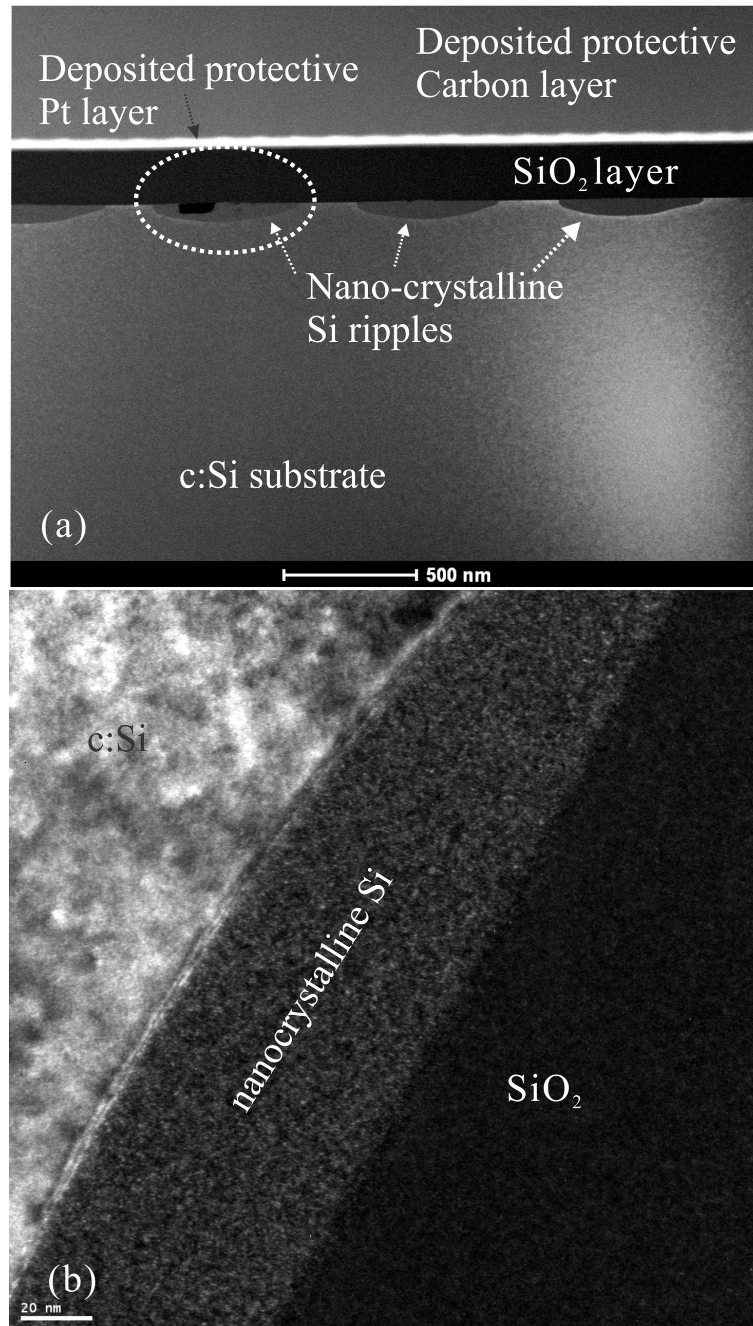

Figure 15: Dark-field TEM results of the same specimen shown in Figure 13 and 14. (a) Dark-field cross-sectional view of TEM image of the FIB-prepared SiO_2-Si specimen with an intact 216 nm thick oxide layer; (b) dark-field HRTEM micrograph of the central area of a typical ripple. Note: the magnifications are different.

is that the ripples are made up of pure Si, not SiO_2-Si. As the TEM specimen was secured on a sample stage made of copper, there are copper peaks that are inevitably detected in both spectra, but with much smaller amplitudes when compared with the oxygen and silicon peaks.

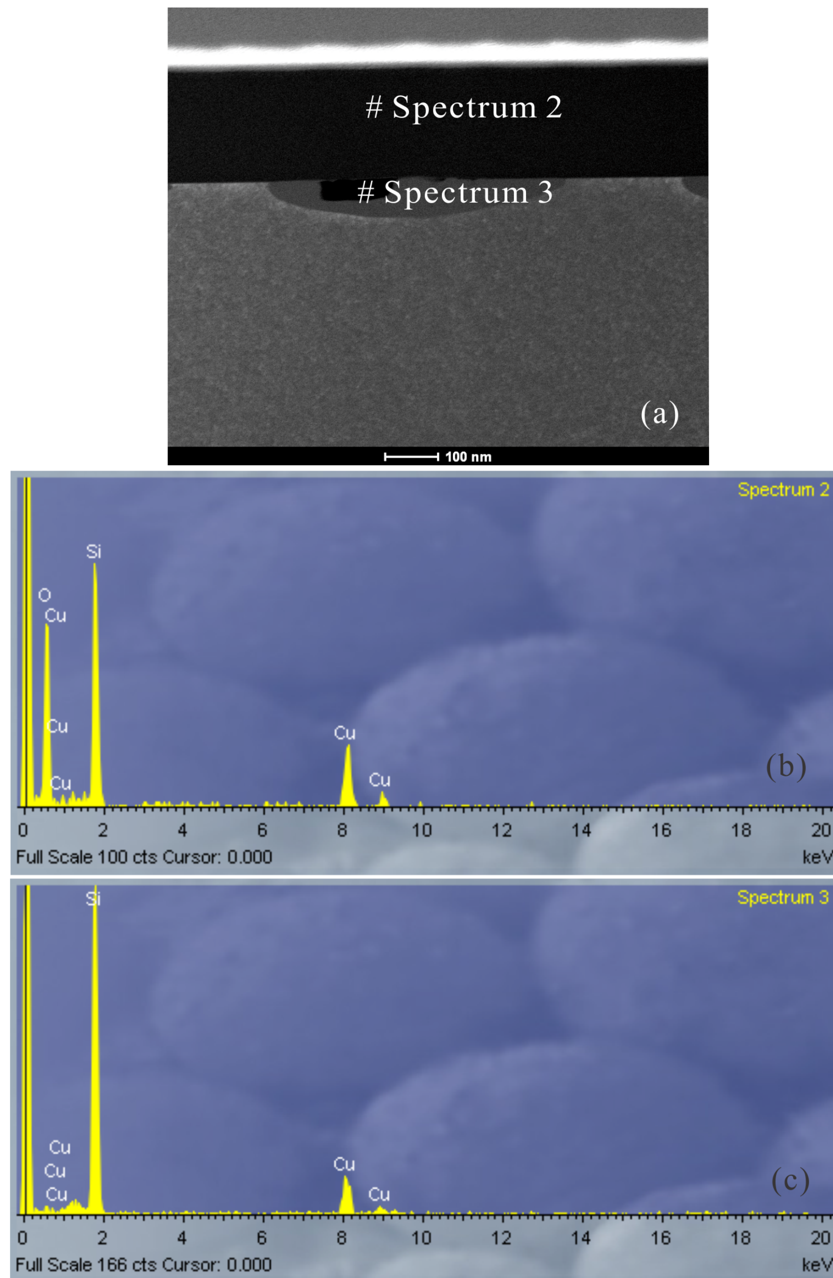

Figure 16: EDX spectra of the same specimen as shown in Figure 15. The sampled locations on one of the ripples are indicated in the TEM image in (a). (a) Dark-field TEM image of one of the ripples at high magnification. The sampled location is indicated by a white dotted circle in Figure 15; (b) EDX spectrum of the SiO_2 layer; (c) EDX spectrum of the sampled ripple.

5.1.3 Effects of oxide thickness

To investigate how the oxide thickness would affect the ripple formation at the SiO_2-Si interface, SiO_2-Si samples with five different oxide thicknesses that are 24, 112, 117, 216, and 1013 nm were laser-processed under similar experimental conditions. Four individual experiments were performed on those samples. Eugene Hsu carried out two experiments on the 117 nm and 216 nm samples. I did two separate experiments: one on the 112 nm sample, the other one on 24 nm and 1013 nm samples. The same focus lens with a focal length of 125 mm was applied in all experiments. In addition, all the samples were irradiated at $\lambda = 800$ nm and a repetition rate of 1 kHz. For Eugene Hsu's experiments, a spot size of 17 μm was measured at the time of his experiments based on the "D^2" technique [69]. For my experiments, a spot size of 19.5 μm was obtained using the same technique. The measured pulse durations for each experiment are listed in Table 4.

Oxide thicknesses (nm)	Pulse durations (fs)	Pulse energy (μJ)	Speed (μm/s)	OM & SEM images
24	184	0.915	2000	Figure 17 (a)
112	156	0.984	2000	Figure 17 (b)
117	141	0.743	2000	Figure 17 (c)
216	156	0.906	2000	Figure 17 (d)
1013	184	1.12	2000	Figure 18

Table 4: Summary of laser irradiation conditions for the SiO_2-Si samples with different oxide thicknesses.

The effects of oxide thicknesses on the ripple formation at the SiO_2-Si interface are demonstrated in Figure 17. All the samples were translated at a speed of 2000 μm/s in the x-direction that is parallel to the polarization of the incident E-fields.

The samples with intact oxide layers were imaged under SEM, but their SEM images have different magnifications. By examining the SEM images, it is fairly reasonable to conclude that there is no significant difference in the overall appearance and structure of the ripples formed on the samples with 112 nm, 117 nm and 216 nm oxide layer thicknesses. The black dots that are the pits shown in Figure 8 are still clearly noticeable along the ripples for all three 112 nm, 117 nm and 216 nm oxide samples. It seems that the oxide thickness has very little impact on the creation and positioning of the pits.

Moreover, because the oxide layer started to break off in most areas, no well-behaved ripple was produced at the SiO_2-Si interface for the 24 nm thick oxide sample. It can be reasoned by the fact that the oxide layer is too thin to withstand the incident laser power that is required to create the ripples while allowing itself to maintain its integrity without being partially damaged. Nevertheless, ripples do form underneath the oxide layer and on the Si substrate for the 24 nm thick oxide sample.

For the 1013 nm oxide sample, it is impossible to observe any ripples underneath the thick oxide layer using SEM because secondary electrons, even with the allowed maximum acceleration voltage of 20 keV, can not penetrate through the oxide. Thus, after laser processing, the 1013 nm oxide sample was put into 10:1 buffered HF solution for about 25 minutes in order to remove the oxide layer. The 1013 nm sample was also irradiated at $\lambda = 800$ nm. The site shown in Figure 18 was translated at a speed of 2000 μm/s in the x-direction parallel to the polarization of the incident E-fields. Other relevant experimental data are listed in Table 4.

In the DIC-OM image shown in Figure 18 (a), the ripples can be identified at their edges, but tend to fade away toward the central regions. In comparison, after

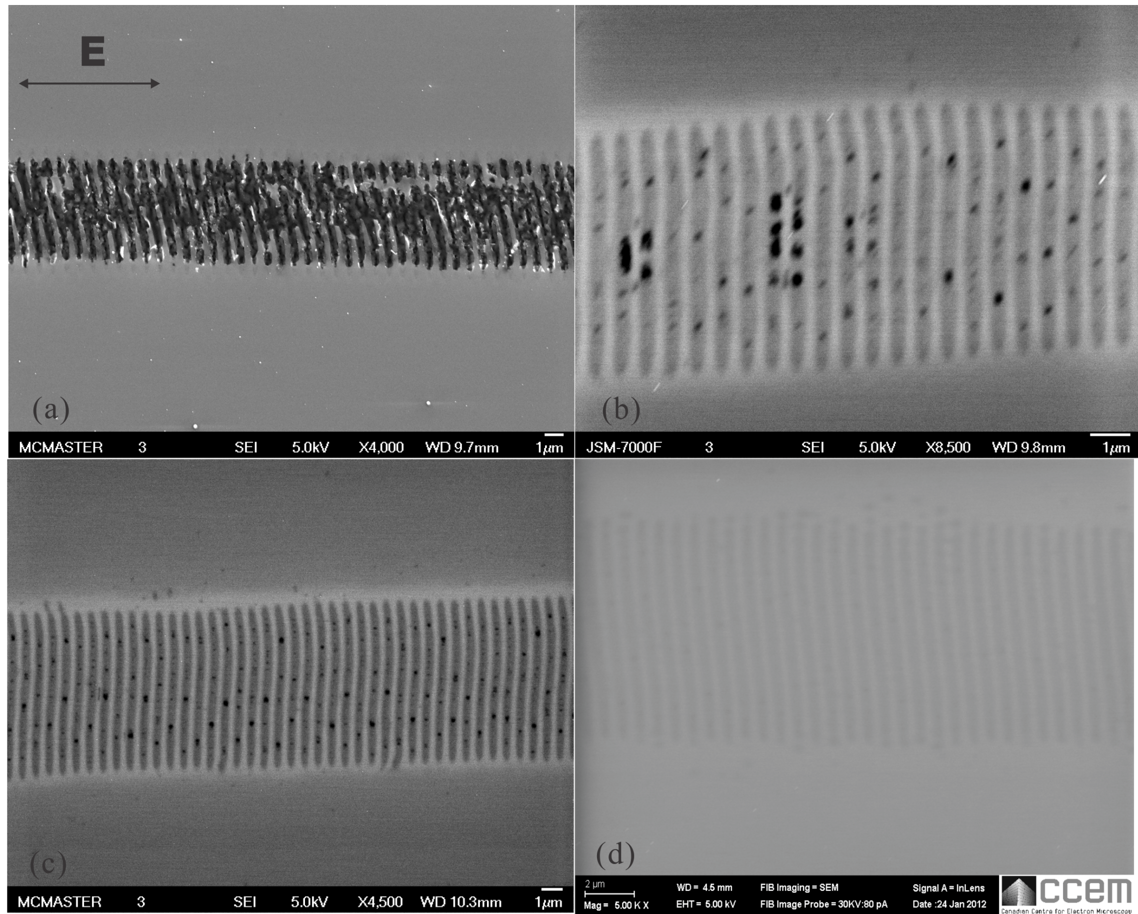

Figure 17: SEM images of the ripples formed on the SiO_2-Si samples with different oxide thicknesses. (a) 24 nm SiO_2-Si sample; (b) 112 nm SiO_2-Si sample; (c) 117 nm SiO_2-Si sample; (d) 216 nm SiO_2-Si sample. Note: the magnifications are different. The polarization of the incident E-fields is indicated in (a).

etching away the oxide layer, the central parts of the ripples can be clearly viewed in the SEM image shown in Figure 18 (b). The distribution of black dots seems to follow sort of a semi-circular pattern in both OM and SEM images. It is most likely related to the overlapping of subsequent laser beams on a passing location, which will be discussed in detail later.

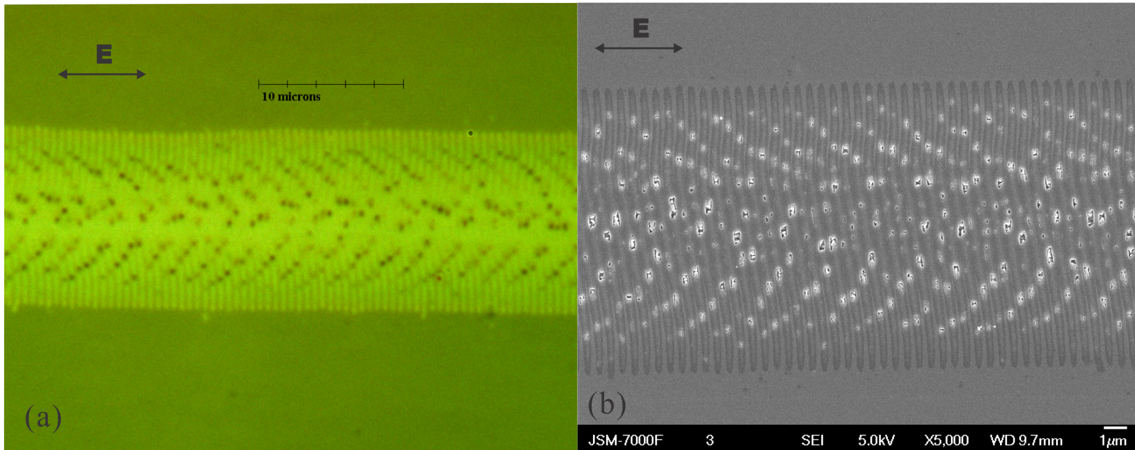

Figure 18: Observation of the ripples for the SiO_2-Si sample having an oxide layer of 1013 nm. (a) DIC-OM image before removing the oxide with HF solution; (b) SEM image after removing the oxide with HF solution. Note: the magnifications are different.

Oxide thicknesses (nm)	24	112	117	216	1013
Peak fluences (mJ/cm^2)	153 ± 23	165 ± 25	164 ± 25	200 ± 30	197 ± 30
Ripple periods (nm)	—	627	634	703	509

Table 5: Comparison of the spatial periodicity of the ripples for the SiO_2-Si samples with different oxide thicknesses. The overall uncertain for the peak fluence is estimated to be 15 %.

The ripple periods for the SiO_2-Si samples with different oxide thicknesses are

evaluated and summarized in Table 5. For each oxide sample, its calculated peak laser fluences for producing corresponding ripples, which are shown in Figure 17 and 18 are also listed in Table 5. As there is no well-defined ripples formed on the 24 nm thick sample, its ripple period is not considered. For the 112 and 117 nm thick samples, their ripple periods are very similar. As both the oxide thickness and the laser energy increase, the ripple periods fluctuate quite a bit. The effects on the ripple formation due to the change in the laser energy are discussed below.

5.1.4 Effects of laser energy

Four different sites on the 1013 nm oxide sample were selected to demonstrate the evolution of ripple formation as a function of the laser power. The SEM images of the four sites are illustrated in Figure 19. To solely emphasize the relationship between the varying laser power and the ripple formation, other experimental parameters for the four sites were chosen to be identical, except for the incident laser power. Their translation speeds are all 2000 μm/s. For the four sites, the oxide layer remained fully attached to the Si after laser irradiation. Thus, HF etching was used to remove the oxide layer in order to observe the details of the ripples under SEM.

From examining the SEM images, three main observations can be realized on the effects of pulse energy on the ripple formation for this particular sample. The first one is that the central regions of the ripples start to get more severely modified as the laser energy increases. It is simply because those areas coincide with the centre of the Gaussian laser beam. The second one is that ripple periods have little dependence on the laser energy. It can be verified by the fact that the measured ripple period is around 510 nm for all four specimens regardless of the variation of the laser energy.

The last observation is that the width of ripples decreases as the laser energy drops. By comparing the SEM images (c) and (d), it can be viewed that the width of ripples almost reduces 50 % even with a slight decrease in the peak fluence between the two specimens, that is around 20 mJ/cm^2. However, one advantage of reducing laser power is that it makes the ripples to become more straight.

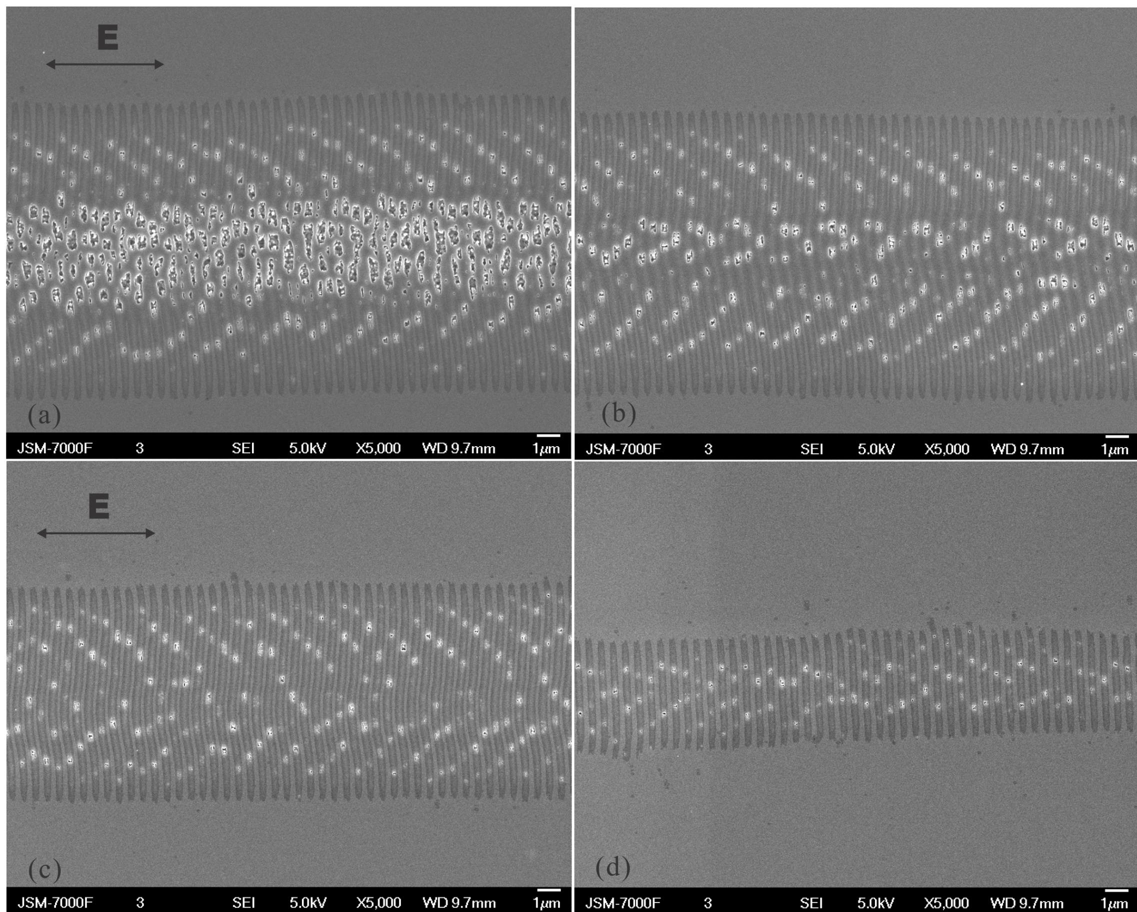

Figure 19: SEM images of the ripples formation as a function of the laser energy for the 1013 nm thick oxide sample after HF etching. (a) 1.20 μJ (200 mJ/cm^2); (b) 1.16 μJ (194 mJ/cm^2); (c) 1.04 μJ (174 mJ/cm^2); (d) 0.932 μJ (155 mJ/cm^2). The four sites were translated at a speed of 2000 μm/s (corresponding to 12 effective numbers of shots) along the x-direction. The 1 kHz repetition rate laser pulses at $\lambda = 800$ nm have a measured pulse duration of 184 fs.

Furthermore, another particularly important matter which must be addressed is that there is a certain range of laser peak fluence at $\lambda = 800$ nm for forming the ripples at the SiO_2-Si interface without breaking off the oxide layer, as well as without causing destructive modifications to the formed ripples. Nevertheless, the exact fluence range has a dependence on the oxide thickness. Figure 20 shows the ripple formation for the oxide sample with an oxide thickness of 112 nm. Except that the oxide thickness is different, other experimental parameters for the 112 nm oxide are the same as those of the 1013 nm thick oxide sample. In Figure 20 (c), it is apparent that there is no ripple created on the 112 nm sample at a peak fluence of 156 mJ/cm^2.

In contrast, in Figure 19 (d) well-structured ripples were created on the 1013 nm thick oxide sample at a peak fluence of 155 mJ/cm^2. Thus, it is valid to conclude that the oxide thickness affects the threshold peak fluence for forming ripples at the SiO_2-Si interface. Additionally, by comparing the SEM images of Figure 20 (b) and (c), the subtlety of finding the exact peak fluence for the onset of creating ripples becomes obvious because an extremely slight difference in the peak fluence (such as, 2 mJ/cm^2 for the 112 nm thick oxide sample) would lead to a strikingly dissimilar outcome in terms of ripple formation.

5.1.5 Effects of cutting direction

The results reported so far only focus on the oxide samples whose cutting directions are in the x-direction. To study how the cutting direction would affect the ripple formation, oxide samples with different oxide thicknesses were also processed under the same laser irradiation conditions in the y-direction, that is perpendicular to the polarization of the E-fields. However, regardless of the oxide thickness, the overall

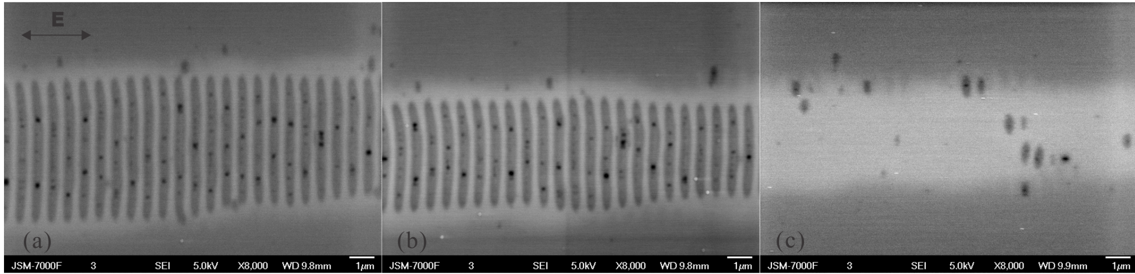

Figure 20: SEM images of the ripples formation at different laser energies for the oxide sample with an intact oxide layer of 112 nm. (a) 0.963 μJ (161 mJ/cm^2); (b) 0.946 μJ (158 mJ/cm^2); (c) 0.936 μJ (156 mJ/cm^2). The three specimens were all translated at a speed of 2000 μm/s along the x-direction.

outcomes and the ripples formed at the interface when cutting in the y-direction turned out to be much less appealing in terms of their uniformity and continuity in the structure. For the purpose of making a comparison between two different cutting directions, typical results for the case of translating the samples along the y-direction are shown in Figure 21.

The oxide sample shown in Figure 21 has an oxide thickness of 112 nm. It was translated at a speed of 2000 μm/s that corresponds to 12 effective laser shots on a given location. Based on the SEM image in Figure 21 (c), the ripples formed at the interface extend in an irregular fashion along the same direction as the cutting direction. Their central regions appear to be more severely modified than their peripheral regions. As the laser power increases, the oxide layer gets peeled off from the Si substrate in which the areas seem to have resolidified Si from a previously molten state.

By examining the SEM images in Figure 21 (b), (c) and (d), there is only a difference of 10%, at best, for the peak fluence "window" from the scenario where the oxide is broken off, to the scenario where there are no continuous ripples created.

Thus, it is reasonable to infer that, when the samples are irradiated along the y-direction, the range of laser peak fluence for creating nice ripples without damaging both the oxide layer and the ripples themselves is extremely narrow. This observation is true for all the oxide samples that have been laser-processed, regardless of the variation in the oxide thicknesses.

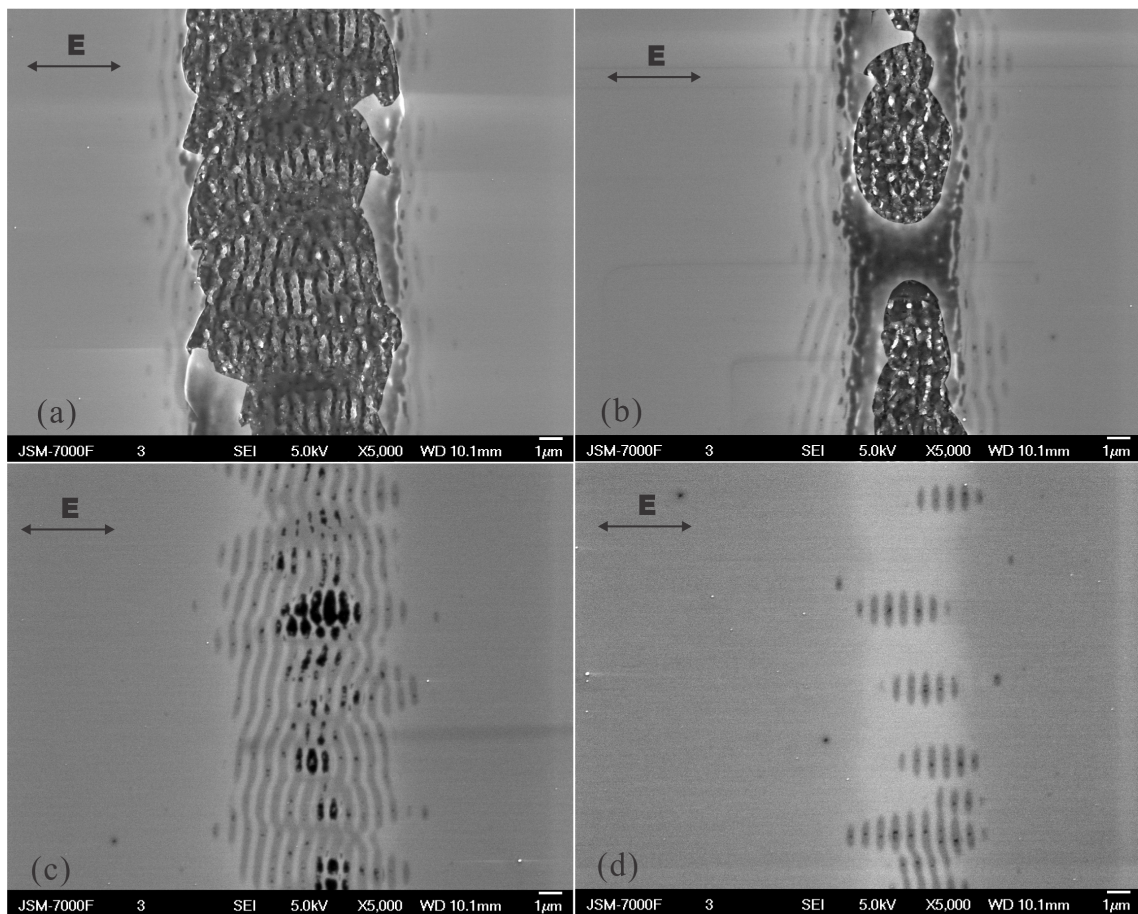

Figure 21: SEM images of the ripples for the 112 nm oxide sample that was translated at a speed of 2000 μm/s in the y-direction perpendicular to the polarization of the E-fields. (a) 0.859 μJ (144 mJ/cm^2); (b) 0.787 μJ (132 mJ/cm^2); (c) 0.753 μJ (126 mJ/cm^2); (d) 0.703 μJ (118 mJ/cm^2).

5.1.6 Effects of different spot size

Other than using the 125 mm focus lens in all the experiments mentioned above, I also conducted an experiment on an oxide sample with a thickness of 158 nm using a Newport 5X microscopy objective lens. The goal was to investigate how the change in the spot size would affect the ripple formation. Apart from changing the focus lens, the rest of experimental details remained identical to other experiments mentioned above. However, for the 5X objective lens, it turned out that there was not even a single irradiation condition that could produce any ripples resembling those when using the 125 mm focus lens. The measured spot size for the 5X objective lens is roughly 4.4 μm (at $1/e^2$ radius) that is almost 4.5 times smaller than the spot size of the 125 mm focus lens.

Even though no regular ripples were produced from the experiment using the 5X lens, it is still worthwhile noticing the unusual patterns that were created at the SiO_2-Si interface upon laser irradiation. As shown in Figure 22, there are semi-circular features appearing at regions where the most intense part of the Gaussian laser beam has passed. The change in the cutting direction did not alter the overall shape of the patterns. For the case of cutting in the x-direction, the edge of each individual semi-circular feature is distinctively defined by a black curve, followed by a relatively short straight line. In contrast, for the case of cutting in the y-direction, their edges are very thin curves attaching to long tails with strange shapes. It is known that the laser beam was moving from the left to the right on the page, as indicated by the arrows. The development of the edges can be contributed to by the overlapping of several subsequent laser pulses. The coincided areas are more severely modified due to larger amount of deposited energy, thus leading to the formation of the clear edges.

The average widths of all the features were measured at 3.0 ± 0.2 μm for the x-direction case, and 2.7 ± 0.3 μm for the y-direction one. Considering that the measured spot size for the 5X lens is 4.4 μm at the 1/e^2 radius, it means that approximately 30% - 35% part of the Gaussian laser beam has sufficient intensity to cause visible modifications to the samples. This value is quite comparable with the 30% value for the 125 mm focus lens. The average distance between the edges of two neighbouring features is measured to be at 2 μm, which is exactly the same for both the x-direction and the y-direction. As demonstrated in Figure 19, there are plenty of small holes occurring on the 1013 nm thick oxide sample, which are regarded as nano-scaled explosions on the Si substrate. The arrangement of the holes seems to follow a semi-circular pattern. The average distance between two adjacent curves that are aligned with numbers of holes is measured at 1.9 ± 0.7 μm. This value is incidentally in close agreement with the average distance of 2 μm between the edges for the structures shown in Figure 22.

Thus, it can be inferred that the nano-scaled explosions result from increasingly deposited laser energy on certain regions that are determined by the amount of overlapping of consecutive laser pulses. Furthermore, the overlapping does not depend on the size of the laser beam, which is evidently supported by the similar average distances from two different experiments using two different focal length lenses. Nevertheless, it does have a critical dependence on the translation speed because the semi-circular patterns can rarely be viewed once the translation speed is reduced from 2000 μm/s to 1000 μm/s. The overlapping should also depend on the repetition rate of the incident laser pulses.

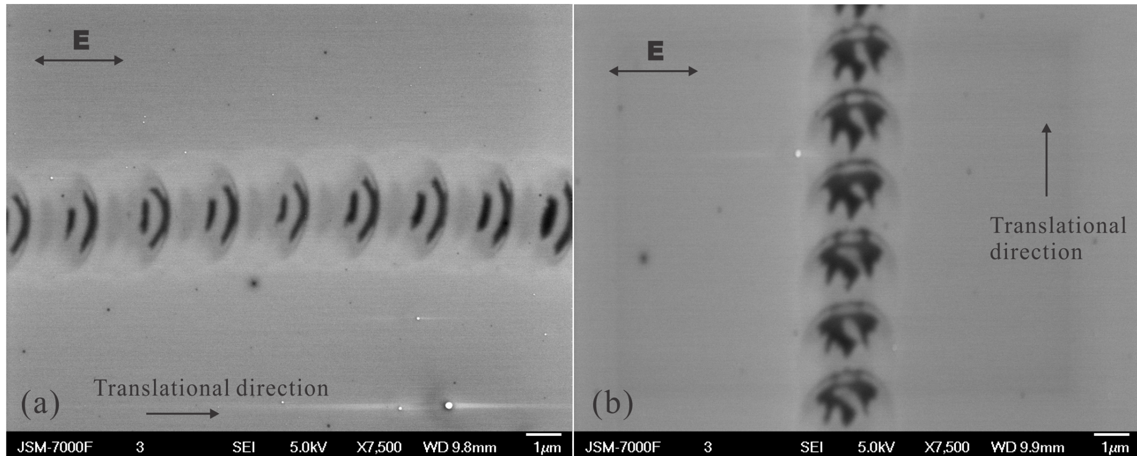

Figure 22: SEM images of the patterns created on the SiO_2-Si samples when being irradiated using a 5X objective lens. The 158 nm thick oxide sample was translated at a speed of 2000 μm/s. (a) cutting in the x-direction with a pulse energy of 58.1 nJ/pulse (183 mJ/cm^2); (b) cutting in the y-direction with a pulse energy of 66.7 nJ/pulse (209 mJ/cm^2).

5.1.7 Comparative results of the ripples between the SiO_2-Si and Si samples at $\lambda = 800$ nm

Typical LSFL that are generated on a pure Si sample by the femtosecond laser pulses translating in both the x- and y- directions can be found in Figure 23, 27 and 28. Compared to the pure Si samples, the ultrashort laser interaction with the SiO_2-Si samples is somehow complicated by the fact that the oxide samples have a layer of dielectric materials on a semiconductor substrate. Therefore, it is not sensible to make a definite comparison of the LSFL formed on the Si sample surface with the ripples created on the SiO_2-Si interface, in terms of their underlining physical interactions. However, making comparisons on certain key characteristics of the features, including surface morphology, detailed structures, ripple periods, etc., could establish connections between Si and SiO_2-Si samples, thus providing new perspectives in helping

understand the fundamental mechanisms of the ripple formation for both cases.

The bulk Si sample was irradiated at λ = 800 nm with a pulse duration of 184 fs. A fixed repetition rate of 1 kHz was used. The sample was translated at speeds of 100, 500, 1000 and 2000 μm/s in both the x- and y- directions, respectively. The same 125 mm focus lens was also used for the Si sample, which has a measured spot size of 19.5 μm (at 1/e^2 radius) at the time of the experiment. Figure 23 shows the evolution of LSFL on the Si sample when translating in the y-direction as a function of pulse energy. As the pulse energy increases, the LIPSS start to be produced at the centre of laser beam and extend outward to the edges. Like the ripples at the SiO_2-Si interface, as shown in Figure 21, the LSFL run perpendicular to the polarization of the E-fields when the Si sample was translated along the y-direction under irradiation.

Nevertheless, it requires almost twice or more the laser peak fluence to create the LSFL on the Si than to form ripples at the SiO_2-Si interface. It indicates that the presence of the oxide layer, to some extent, facilitates the processes of creating ripples on the Si substrate. One likely reason is that the oxide layer constrains the propagation of the deposited laser energy, thus leading to more intense coupling among the generated surface waves. It then reduces the threshold for producing periodic modifications on the Si substrate.

The results of LIPSS formation when cutting the Si sample in the x-direction are illustrated in Figure 27 and 28. One observation that must be pointed out is that it requires much more laser energy to generate LSFL on the Si sample when translating in the y-direction than in the x-direction when other experimental conditions are maintained identical. However, the opposite situation is true for creating ripples at the SiO_2-Si interface. Moreover, regardless of cutting directions, the ripples formed

on both the Si and the SiO_2-Si samples are all perpendicular to the polarization of the incident E-fields, that is along the x-direction.

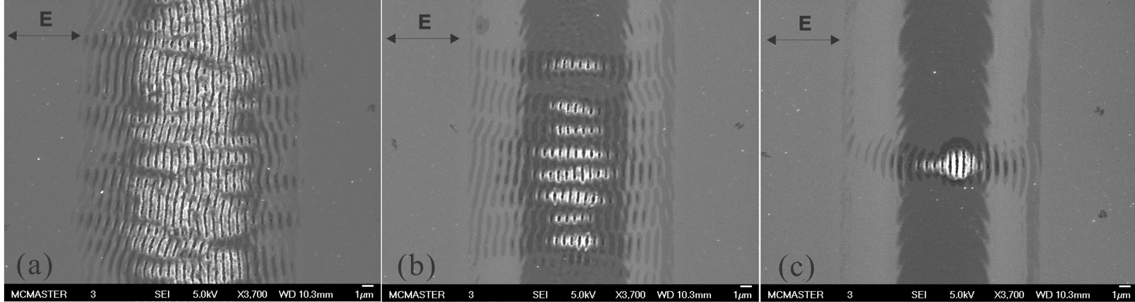

Figure 23: SEM images of LIPSS formed on a pure Si sample translating in the y-direction with a translation speed of 2000 μm/s. (a) 1.58 μJ (279 mJ/cm^2); (b) 1.52 μJ (268 mJ/cm^2); (c) 1.48 μJ (261 mJ/cm^2).

In addition to comparing the ripple structures and the threshold laser fluences between the Si sample and the SiO_2-Si samples, another important aspect that must be considered is their ripple periods. As an example, four different sites from the 117 nm thick oxide sample were chosen, which were irradiated with different laser fluences. The main reason to select the four sites is that they all have intact oxide layers. Their ripple periods were measured based on their SEM images (not shown here) and plotted in Figure 24. The specimens from the Si sample and the SiO_2-Si samples were all translated at a speed of 2000 μm/s along the x-direction, which are also indicated in the Figure 24. It is evidently noticed that the ripple period of the LSFL for the bulk Si is approximately 10 % larger than that of the ripples formed at the interface of the SiO_2-Si.

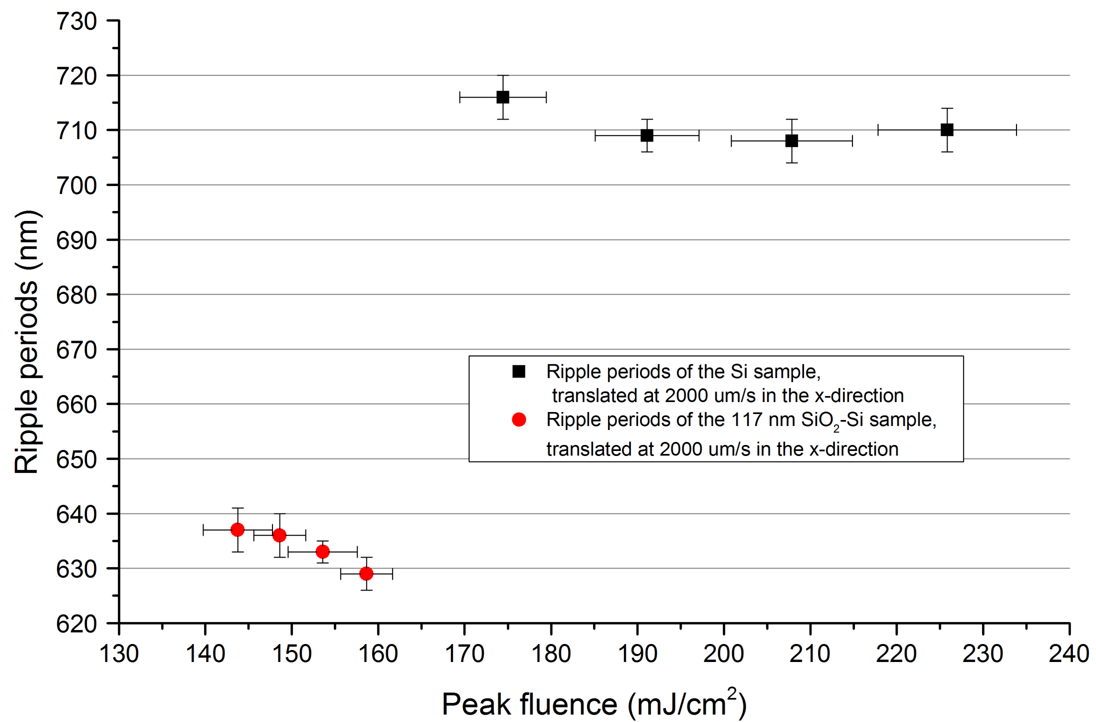

Figure 24: Plot of the ripple periods for both the pure Si samples and the SiO_2-Si sample with an oxide thickness of 117 nm. Both samples were irradiated at $\lambda = 800 \pm 3$ nm.

5.1.8 Additional results

Typical features created at slow translation speeds

From a series of experiments conducted on the oxide samples with different oxide thicknesses, it is found that there is a quite distinction in terms of the ripple formation and material modifications when the translation speed drops from 1000 μm/s to 500 μm/s while other experimental conditions are identical. As the translation speed is reduced from 2000 μm/s to 100 μm/s, the number of effective shots on a given spot increases from 12 to 244. Assuming a constant laser energy is maintained, the increasing number of laser pulses brings about more laser energy deposition into the samples, thus leading to more violent material modifications and removal of the oxide layer. Even though the oxide layer can still remain fully attached to the Si substrate within a certain range of laser fluences at translation speeds of 100 μm/s and 500 μm/s, the well-behaved ripple structures that are obtained at higher speeds disappear at those low speeds.

Figure 25 shows typical LIPSS produced at the SiO_2-Si interface after the 117 nm thick oxide sample was irradiated at a translation speed of 100 μm/s. The translation direction is along the y-axis that is perpendicular to the E-fields. In Figure 25 (a), it can be seen that the oxide layer does not seem to be modified in a significant way and remains unbroken. In addition, there are LSFL features running along the direction that is parallel to the polarization of the E-fields. The regions between the LSFL appear to be filled with holes. After removing the oxide layer using HF etching as shown in Figure 25 (b), the main outlines of the LSFL are still visible, but they appear to be thinner. The holes now seem to converge into shallow trenches that are full of HSFL whose dimensions are substantially smaller than the LSFL, which also

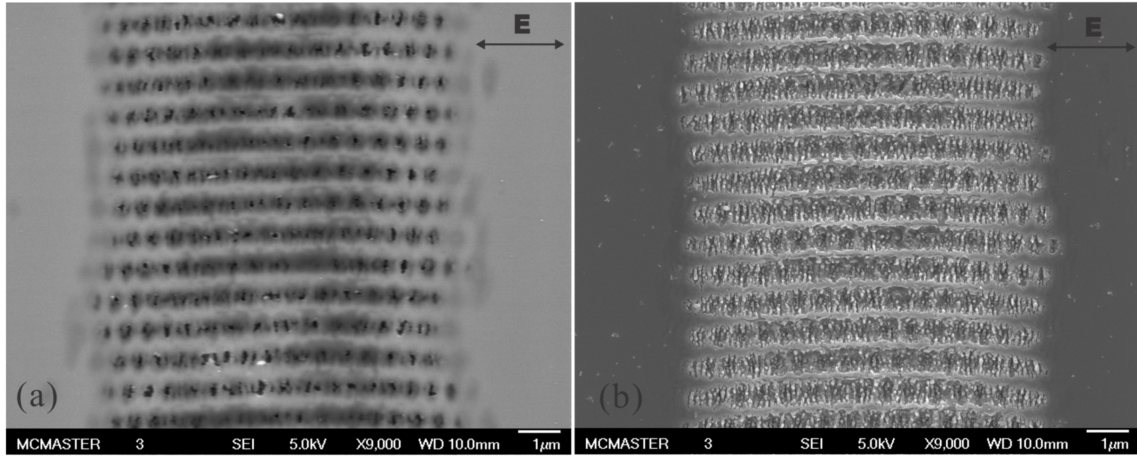

Figure 25: SEM images of the LIPSS formed at the SiO_2-Si interface when the translation speed is reduced to 100 μm/s. (a) Prior to HF etching; (b) after HF etching. The sample has an oxide thickness of 117 nm before HF etching. The site was irradiated at 800 nm wavelength with a laser energy of 0.581 μJ (an individual pulse fluence of 131 mJ/cm^2).

extend perpendicularly to the LSFL. The spatial periodicity of the LSFL is measured to be roughly 720 nm, whereas the spatial periodicity of the HSFL is in the range of between 110 - 190 nm. The AFM measurements of the structures shown in Figure 25 can be found in Figure 26.

Tilting of the LSFL on Si samples

From the experiments done on pure Si samples, it was a observed that the orientation of the LSFL that were produced on the Si surface after laser irradiation depends on both the translation speed and the incident laser power. This phenomenon only occurred when the samples were translated along the x-direction. The LSFL that were formed in the case of translating in the y-direction do not exhibit these dependences. Figure 28 and 27 demonstrate how the slopes of the LSFL vary as a function of the translation speed and a function of the incident laser power, respectively. From the

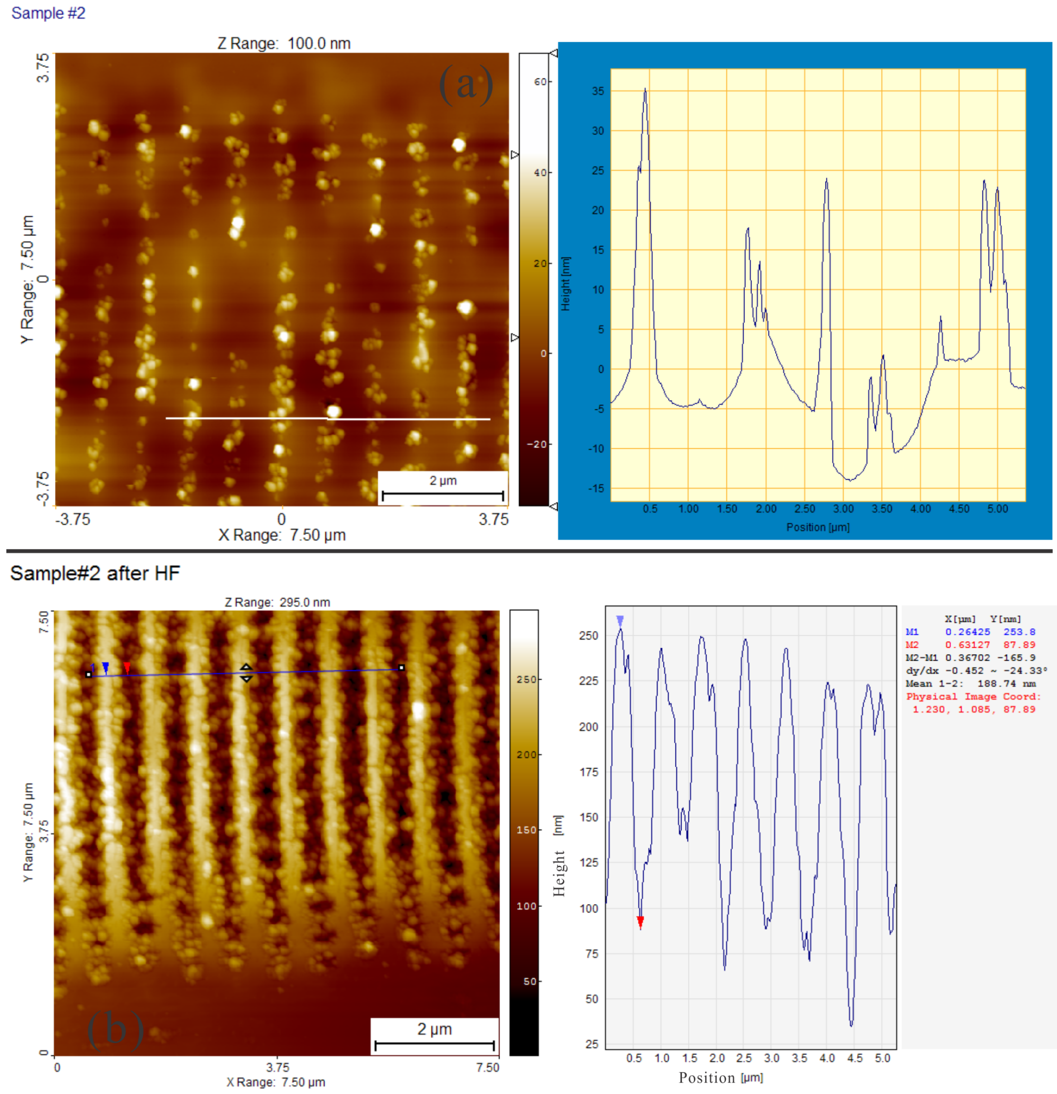

Figure 26: AFM measurements for the LIPSS formed at the SiO_2-Si interface when the translation speed is reduced to 100 μm/s. (a) AFM scanning image and the corresponding height profile (right) prior to HF etching; (b) AFM scanning image and the corresponding height profile (right) after HF etching. The scanning range is 7.5 μm by 7.5 μm for both (a) and (b).

SEM images, it can be clearly observed that the LSFL become gradually less slanted as the speed is reduced from 2000 μm/s to 500 μm/s, while other experimental conditions remain identical. The same tendency happens when the laser energy drops from 1.46 μJ to 0.896 μJ. Despite the variation in the orientation, the spatial periodicity of the LSFL stays roughly the same, that is approximately 710 nm.

The exact reasons for the occurrence of these dependences are still uncertain. At first, it was suspected that the impurity in the polarization of the laser beam would be likely to cause the slanted LSFL. However, this argument appears to be less plausible after the polarization of the laser beam was experimentally confirmed to be quite linear-polarized along the x-direction and close to its best quoted quality (within 2 - 3 %). Moreover, by observing the edges of the LSFL, particularly in Figure 27 (e) and (f), they look very straight compared to the central parts with stronger modifications. It indicates that the tilting of the LSFL is somehow triggered by a more intricate mechanism. Nevertheless, one definite conclusion that can be made here is that the tilting of the LSFL can be adjusted by changing the accumulated amount of laser energy deposited into the Si samples, either through increasing the number of effective laser shots or through simply increasing the laser energy.

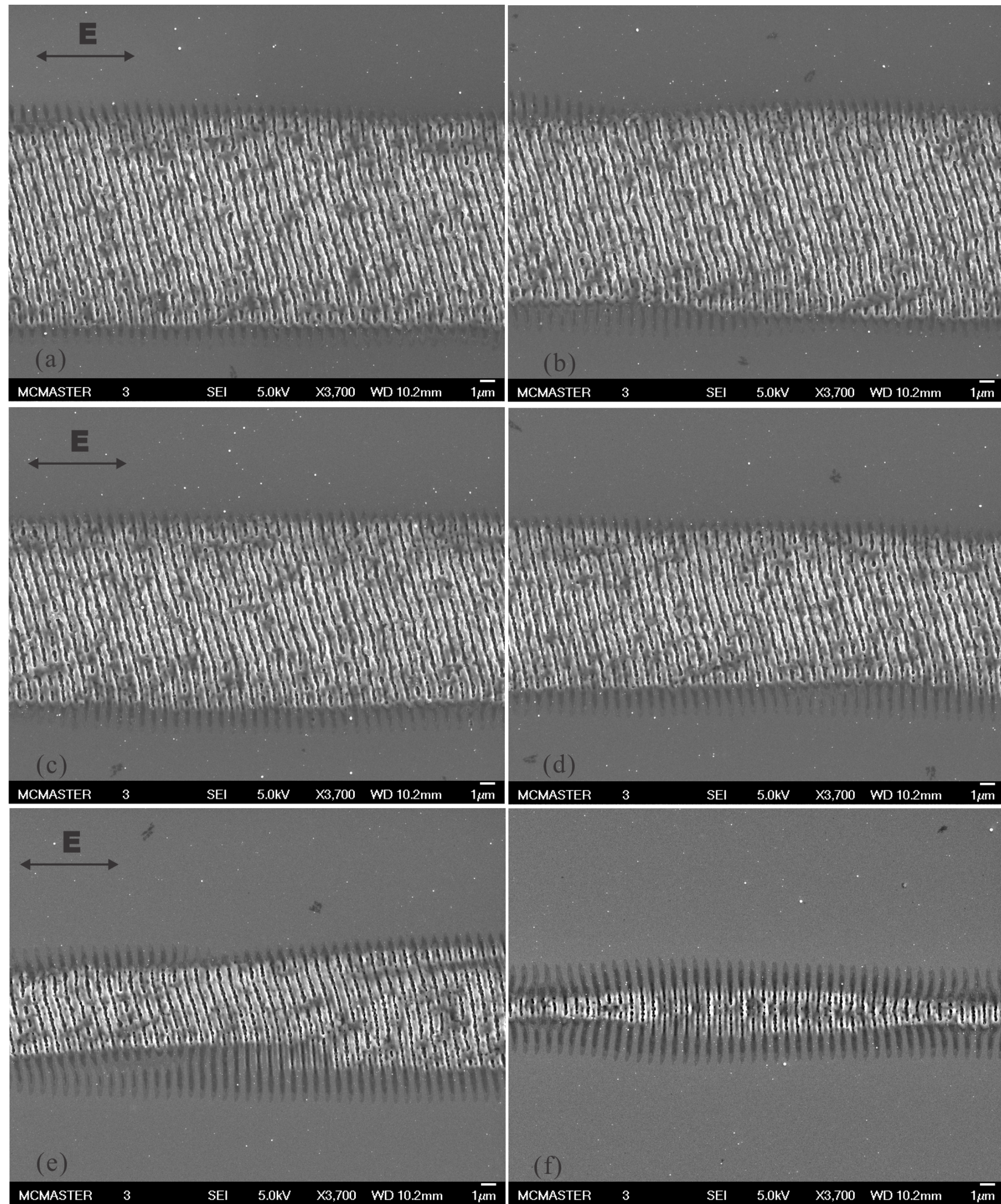

Figure 27: Change in the slope of the LSFL on a pure Si sample as a function of incident laser energy. (a) 1.46 μJ (258 mJ/cm^2); (b) 1.28 μJ (225 mJ/cm^2); (c) 1.18 μJ (208 mJ/cm^2); (d) 1.08 μJ (191 mJ/cm^2); (e) 0.989 μJ (174 mJ/cm^2); (f) 0.896 μJ (158 mJ/cm^2). The sample was translated at a speed of 2000 μm/s in the x-direction.

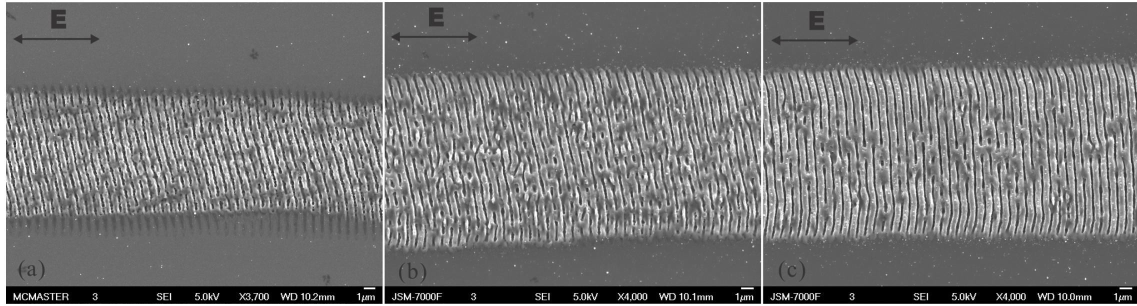

Figure 28: Change in the slope of the LSFL on a pure Si sample as a function of translating speed. (a) At 2000 μm/s (i.e. 12 numbers of effective shots); (b) at 1000 μm/s (i.e. 24 numbers of effective shots); (c) at 500 μm/s (i.e. 48 numbers of effective shots). The three specimens have the same pulse energy of 1.08 μJ (an individual laser peak fluence of 191 mJ/cm^2) and the same translation direction (along the x-axis).

"Sub-threshold" ripples on Si samples

The term "sub-threshold" introduced here is to distinguish between the case when the regular LIPSS are produced on Si samples with evident material ablation and the case when periodic structures are created due to only non-thermal melting on the Si surface. The "threshold" is considered as the single-shot ablation threshold for a bulk Si sample under sub-picosecond laser pulse irradiation. The "sub-threshold" ripples are demonstrated in Figure 29. They are very straight and run perpendicular to the polarization of the incident E-fields. Their spatial period is measured to be around 765 nm, which is about 8 % larger than the spatial periodicity of 710 nm for the regular LSFL on Si samples.

Observed from the SEM image, the central regions of the "sub-threshold" ripples, which correspond to the most intense part of the Gaussian laser beam seem to be darker than their peripheral areas, indicating that they were subjected to more strong modifications upon laser processing. Even so, compared to the unaffected Si substrate, the subtle discolouration of the ripples is the evidence supporting that the Si has

gone through from non-thermal melting to resolidification without significant material ablation.

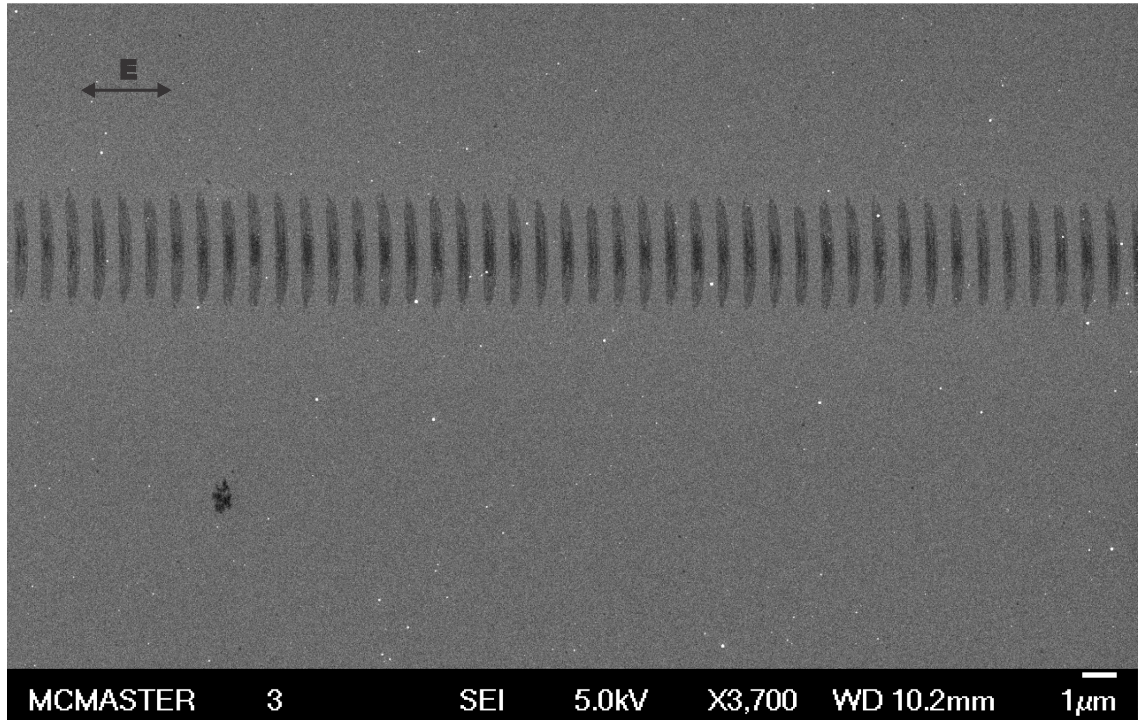

Figure 29: SEM image of "sub-threshold" ripples on a bulk Si sample. The site was translated at a speed of 2000 μm/s along the x-direction and irradiated with a pulse energy of 0.859 μJ (151 mJ/cm^2) at $\lambda = 800$ nm. The ripple period is measured to be around 765 nm.

Comments on the experiment of increasing the number of passes

The laser experiments mentioned above consider the case of irradiating an individual site on a given oxide sample with a single-pass of the laser beam. It means that each track under irradiation is processed only once by translating the laser beam at a certain speed from one end of the track to the other. Subsequently, while blocking the laser beam with a temporally closed mechanical shutter, the laser beam is immediately

moved away from the irradiated site to another site that has not been processed yet. I also carried out a laser experiment with a sole intention of increasing the number of passes on a specific track in order to see how it would affect the ripple formation at the interface. However, the overall experimental outcomes in terms of the ripple formation turned out to be not very interesting.

An oxide sample with an oxide thickness of 112 nm was used in the experiment. The peak laser wavelength and the pulse duration were measured to be 800 nm and 170 fs respectively. The same focusing lens with an focus length of 125 mm was also employed. The translation speeds covered 2000, 1000 and 500 μm/s in both x- and y-directions. Limited by the size of an oxide sample and the total processing time, the numbers of passes used were chosen to be 1, 5, 10, 20, 40, 50, 60 and 80. An increase in the number of passes leads to the number of effective laser shots at a specific speed on a given location to be correspondingly multiplied by the same value. Therefore the laser pulse energy must be reduced substantially to compensate the drastic increase in the effective shots so as to allow the ripples to form at the SiO_2-Si interface without damaging the oxide layer. The laser energy is within the range of between 0.391 μJ and 0.598 μJ.

Within the applied irradiation conditions in the experiment, there are no well-structured ripples that can be formed on the oxide sample. At low laser energies, e.g. below 0.5 μJ, and faster translation speeds, such like 2000 and 1000 μm/s, the regular ripples were created in a discontinuous fashion for both translation speeds (i.e. x- and y- directions). In addition, partial removal of the oxide layer on the ripples occurs in a random manner. As both laser energy and translation speed increase, the general features created on the sample resemble closely the typical features which are

produced at slow translation speeds, as shown in Figure 25.

5.2 Laser irradiation using femtosecond pulses at 400 nm wavelength

5.2.1 Experimental details

The same Ti:Sapphire laser system as mentioned in Chapter 3 was run at $\lambda = 800$ nm with a repetition rate of 1 kHz. The 400 nm wavelength light was acquired by frequency-doubling the fundamental 800 nm wavelength using a AR-coated beta barium borate (BBO) crystal, with a thickness of 500 μm. The BBO crystal was inserted in the beam path between the last thin-film polarizer (TFP 3) and the first dielectric mirror (DM 1), as illustrated in Figure 3. Because the four dielectric mirrors (DM 1, 2, 3, 4) used for the 800 nm wavelength are only coated for the IR region, they must be swapped with four dielectric mirrors particularly coated for the UV region when the 400 nm wavelength is in use. Moreover, the calcite polarizer was removed from the beam path as its operating wavelength range does not cover the 400 nm wavelength.

A different BK 7 plano-convex lens (Newport KDX097) was used because its AR-coating was more suitable for the 400 nm wavelength as compared with the focusing lens used for the 800 nm wavelength. However, both lenses have the same focus length of 125 mm. Due to the reduction in the incident wavelength, the spot size (at $1/e^2$ radius) at $\lambda = 400$ nm for the lens was measured to be at approximately 12.3 ± 0.6 μm using the D^2 technique [69]. For safety reasons, a fully reflecting mirror at the position of M1 in Figure 3 (refer to it in Chapter 3) was replaced with a 20% beam

splitter to reduce the 400 nm intensity after conversion. In addition, a beam block was also placed right behind the first dielectric mirror to block the residual 800 nm light going through the BBO crystal.

Three individual experiments were conducted using the 400 nm wavelength on SiO_2-Si samples with two different oxide thicknesses that were 112 nm and 158 nm. The SiO_2-Si samples for the $\lambda = 400$ nm experiments were cleaved from exactly the same oxide wafers for the $\lambda = 800$ nm experiments. The overall sample cleanness for the 112 nm and 158 nm samples can be referred in Figure 5 (e) and (f) of Chapter 4. In the first experiment, the pulse duration was measured to be at 184 fs, and it was measured to be at 198 fs for the last two experiments. The measured pulse durations were acquired using $\lambda = 800$ nm. For $\lambda = 400$ nm, the actual pulse durations are likely to altered, when compared with the measured values due to extra dispersion caused by going through the BBO crystal or due to the SHG process itself. The samples were all irradiated in a translational fashion. The translation speeds include 2000, 1000, 500 and 100 μm/s, which correspond to numbers of effective laser shots on a given spot of 8, 15, 30 and 150 with the 12.3 μm spot size. The cutting directions cover both the x- and y- axes. Regardless of the slight difference in the oxide thicknesses, the overall outcome in terms of the ripple formation and material modifications from the three experiments are in close agreement with one another.

5.2.2 The most well-structured ripples formed at the SiO_2-Si interface at $\lambda = 400$ nm

Observation under SEM

The most well-behaved ripple example from the $\lambda = 400$ nm experiments is selected and displayed in Figure 30. The oxide sample has a 158 nm thick SiO_2 layer that remained fully intact after laser irradiation. The chosen site was translated along the x-direction with a translation speed of 500 μm/s. Judging from the SEM image, it can be seen that the orientation of the ripples runs along the y-direction that is perpendicular to the polarization of the incident E-fields. The ripples extend very straight and continuously all the way from one edge to the other. Unlike the case for $\lambda = 800$ nm, the waviness of the ripples vanishes, at least under SEM imaging.

More importantly, the nano-explosions that appear to be small black dots along the ripples produced with laser pulses at $\lambda = 800$ nm also become hardly discernible in the SEM image. The black dots can not be found in the SEM image at a higher magnification around 8000 times either, which is not shown here. Nevertheless, there are some tiny black dots scattered all over the specimen, as well as a few spots covered with larger and denser dots. By comparing the SEM image of the specimen after laser irradiation with the SEM image of the 158 nm thick oxide sample before processing as shown in Figure 5 (f), it can be verified that the black dots are likely to be external contamination, e.g. dust, which already resides on the sample surface before laser processing. The ripple formation does not seem to be affected by the presence of the dust. For the ripples shown in Figure 30, their spatial periodicity is directly measured to be around 310 nm. However, regardless of the variations in the translation speed

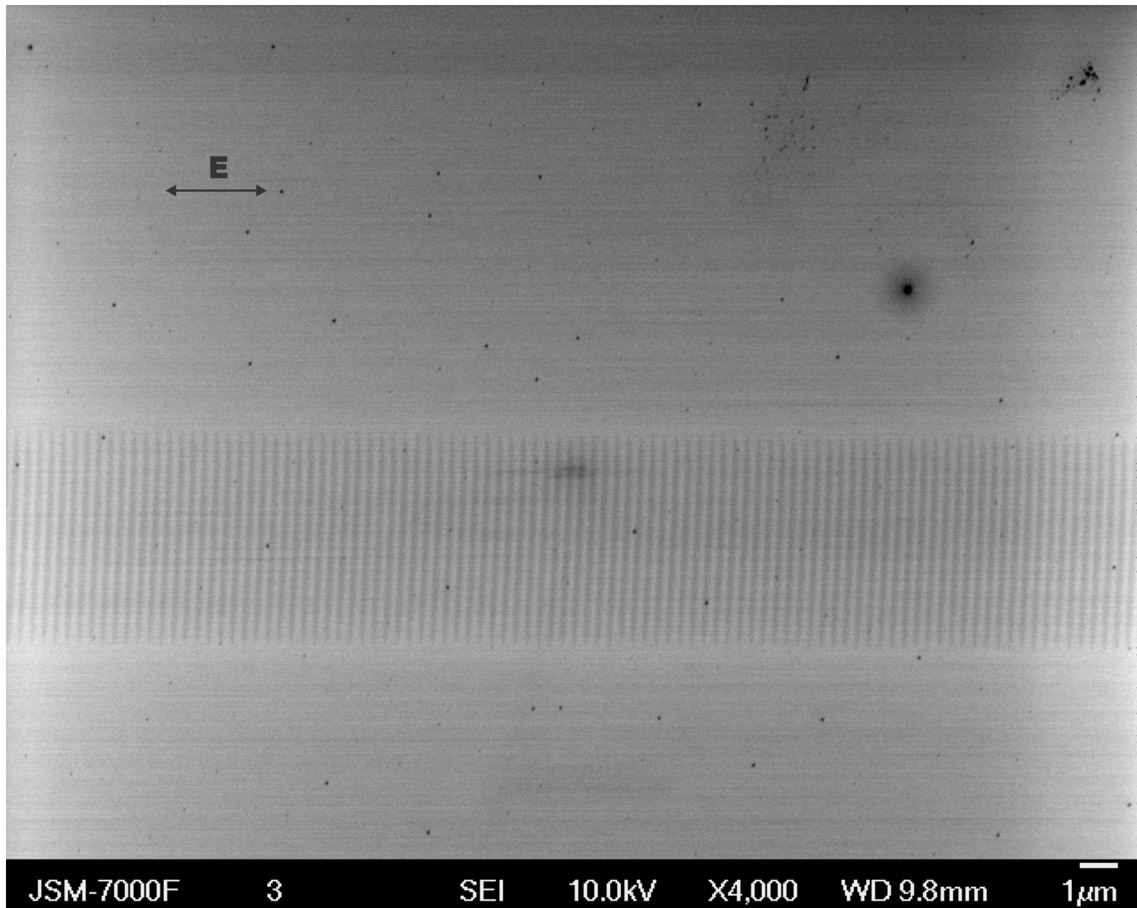

Figure 30: SEM image of the well-behaved ripples on a SiO_2-Si sample with an oxide thickness of 158 nm after being irradiated with $\lambda = 400$ nm laser pulses. The site was translated at a speed of 500 μm/s in the x-direction, which corresponds effectively to 30 shots on a given spot. The incident laser energy is 0.0970 μJ (a peak fluence of 43 mJ/cm^2). The black dots are external contaminants, such as dust.

and the incident laser energy, the ripples maintained the same period of 310 nm for the 158 nm thick oxide sample when it was translated along the x-direction. In terms of the ripples when the sample was translated along the y-direction, typical results will be discussed later.

TEM analysis

Figure 31 shows the cross-sectional bright-field TEM image of the TEM specimen that was prepared using the FIB technique. The specimen was acquired from the central regions of the ripples formed on a SiO_2-Si sample with an oxide thickness of 158 nm after it was irradiated under the same experimental conditions as the ripples shown in Figure 30. It can be seen that the TEM image contains three entire ripples appearing to be small bumps in the Si substrate. It confirms that the ripples are produced at the interface of SiO_2 and Si after laser irradiation while the oxide layer remains fully intact. In addition, the ripples seem to be quite similar in terms of their overall appearance and structure. The thickness of the oxide layer was directly measured to be roughly 155 nm that is in very close agreement with the ellipsometry measurement of 158 nm. The average spatial distance between adjacent bumps was evaluated to be around 310 nm.

Figure 32 (a) shows the magnified view of a single ripple in the same FIB specimen shown in Figure 31. Judging from the image contrast, the ripple extends into the Si substrate with the largest depth of roughly 22 nm at its peak. This is almost 4 times less than the largest modulation depth for the ripples that are formed at $\lambda = 800$ nm, which is around 78 nm. The boundaries that separate different material compositions can be clearly viewed from the TEM image. To acquire detailed information about the

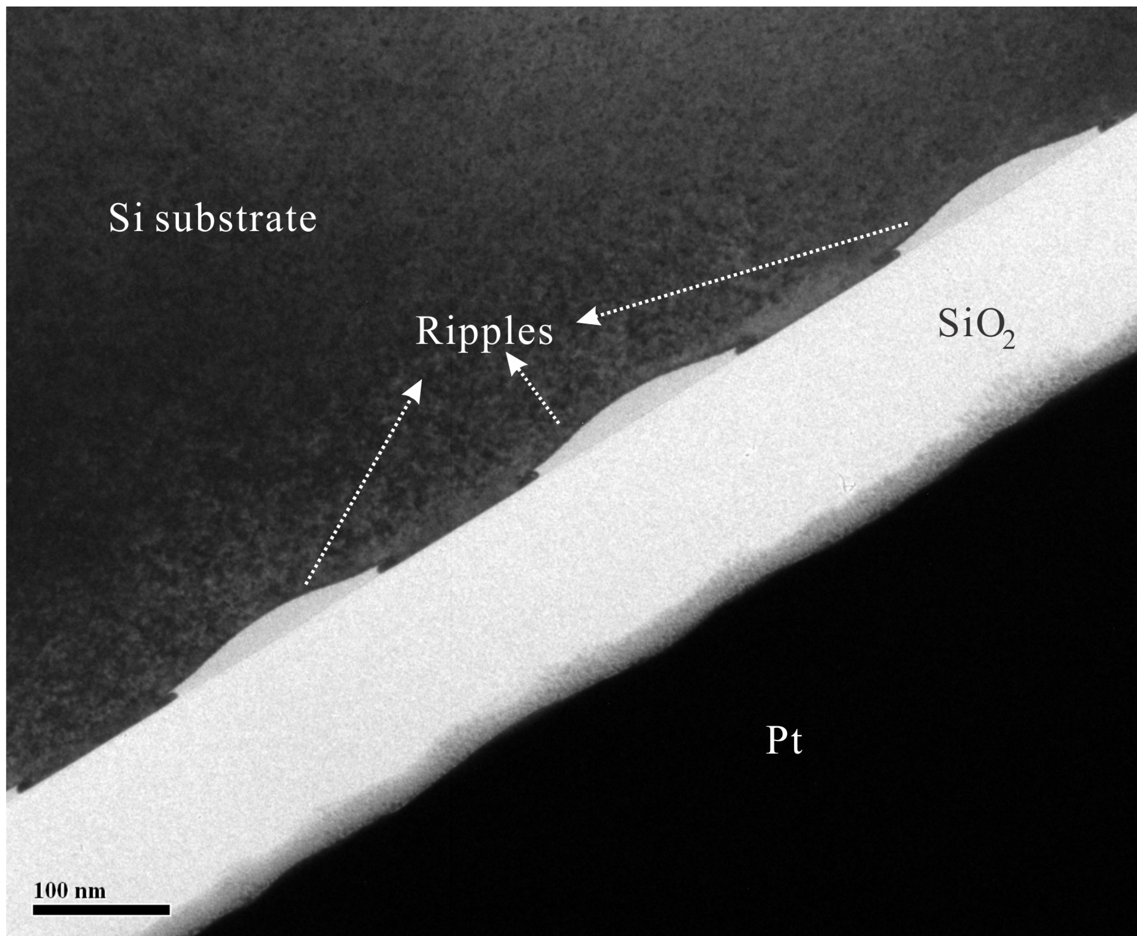

Figure 31: Cross-sectional bright-field TEM image of the FIB-prepared SiO_2-Si specimen with an intact oxide layer of 158 nm, showing the ripples produced at the SiO_2-Si interface after the sample was irradiated with laser pulses at $\lambda = 400$ nm. Three ripples are captured in the TEM image (taken by Dr. Carmen Andrei in Philips TEM CM12). Different material compositions are explicitly labelled.

crystalline properties of the ripple, HRTEM micrographs were acquired and shown in Figure 32 (b - d) regarding different locations of the ripple, including its upper edge, its central area near the peak, and its lower edge. Based on the HRTEM micrographs, it can be inferred that the ripple is composed of nano-crystalline silicon, which has the same crystalline structure as the ripples produced with laser pulses at $\lambda = 800$ nm.

The transition between the purely crystalline Si substrate and the nano-crystalline ripple can be clearly distinguished by a curved boundary. Moreover, the transition between the nano-crystalline ripple and the SiO_2 layer can also be recognized by a straight boundary. The most intriguing finding from the HRTEM micrographs is that both edges of the ripple with nano-crystalline structure appear to stretch out laterally into Si substrate that has pure crystalline structure. The mixed regions where both crystalline forms coexist appear to be more prominent and compelling in the dark-field micrograph that is shown in Figure 33 (b). At the edges of the ripples, it is evident that small amounts of materials in white colour are contained within darker materials that seem to be the same materials making up the ripple.

Furthermore, through comparing the HRTEM micrographs as shown in Figure 33 of the same ripple that were acquired in bright-field and dark-field imaging modes, it can be verified that the crystalline structure of the ripple bears more resemblance to the amorphous SiO_2 layer than to the crystalline Si substrate. In order to provide relatively quantitative measurements on the crystalline structure of the ripple, selected area electron diffractions (SAED) were performed. Multiple electron diffraction patterns (EDPs) were acquired by sampling different spots on the ripple and the SiO_2 layer to evaluate the statistical variations in the EDP.

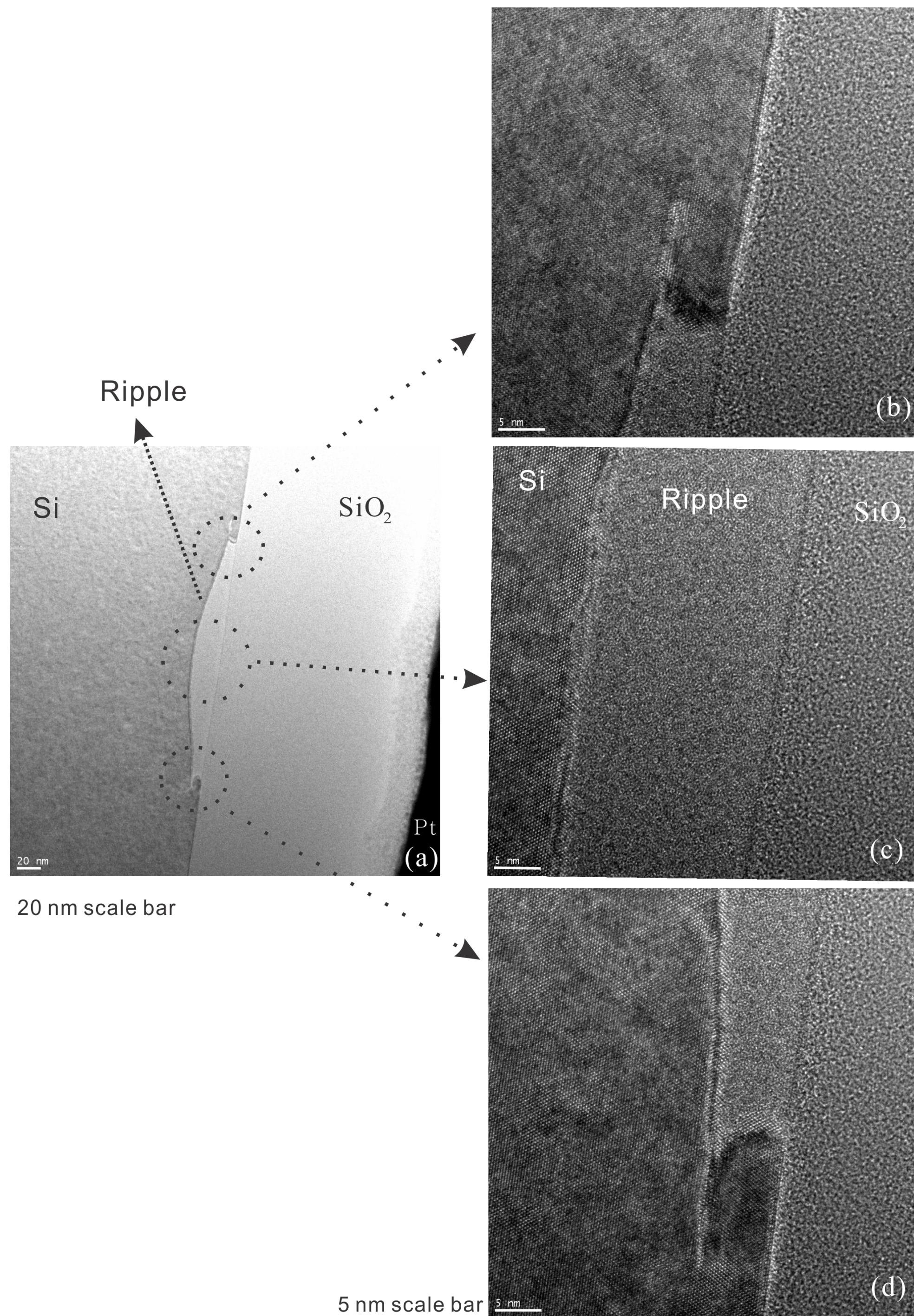

Figure 32: Bright-field HRTEM micrographs of the same FIB specimen shown in Figure 31. (a) Overview of a single ripple; (b) one edge of the ripple; (c) its central region; (d) its other edge. The corresponding sampled areas for each micrograph on the ripple are indicated with dotted circles in (a).

There are six sampling spots obtained within the ripple, which are indicated with sampling marks from O_2 to O_7 in Figure 34 (a). There are six samples spots on the SiO_2 layer, which are denoted with sampling marks from O_8 to O_{13}. However, because the EDPs corresponding to the ripple and the SiO_2 layer are quite consistent with one another, typical EDPs for the Si substrate, the ripple and the SiO_2 layer are illustrated in Figure 34 (b - d). The concentrical ring-patterns in the EDP of the ripple substantiate that the ripple is in the form of a nano-crystalline structure with a crystalline size on the order of a few nanometers, which is the same conclusion drawn for the ripples created at $\lambda = 800$ nm.

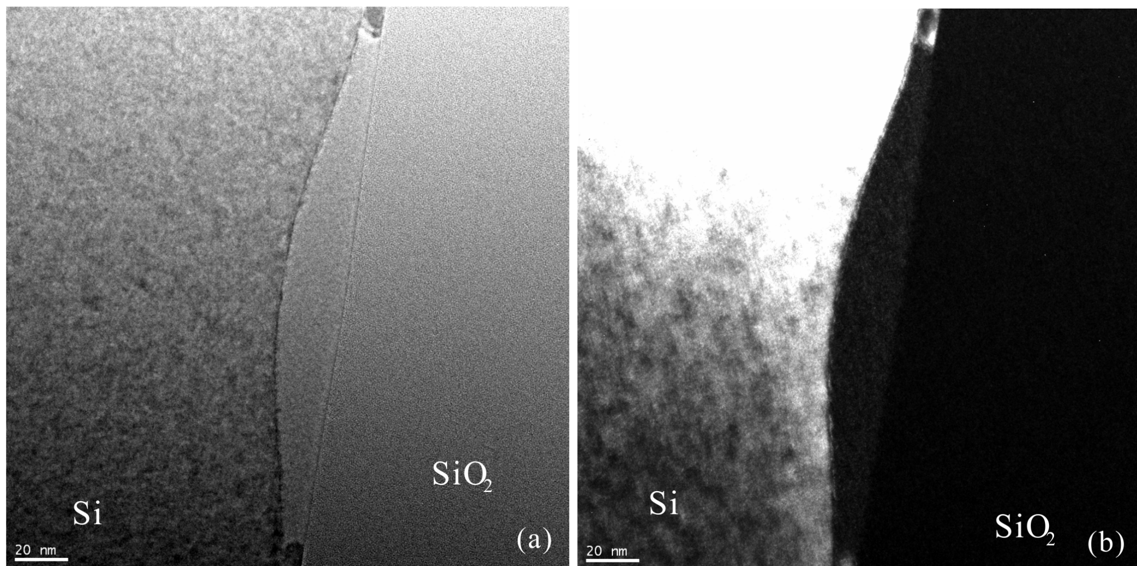

Figure 33: HRTEM micrographs of the same ripple taken under different imaging modes. (a) Bright-field HRTEM micrograph; (b) dark-field HRTEM micrograph. The same ripple is imaged under the same magnifications.

By means of obtaining the EDS spectra for the TEM specimen, the elemental composition of the ripple was determined to be pure silicon. Figure 35 displays the EDX spectra for different regions near one of the ripples in the TEM specimen. A

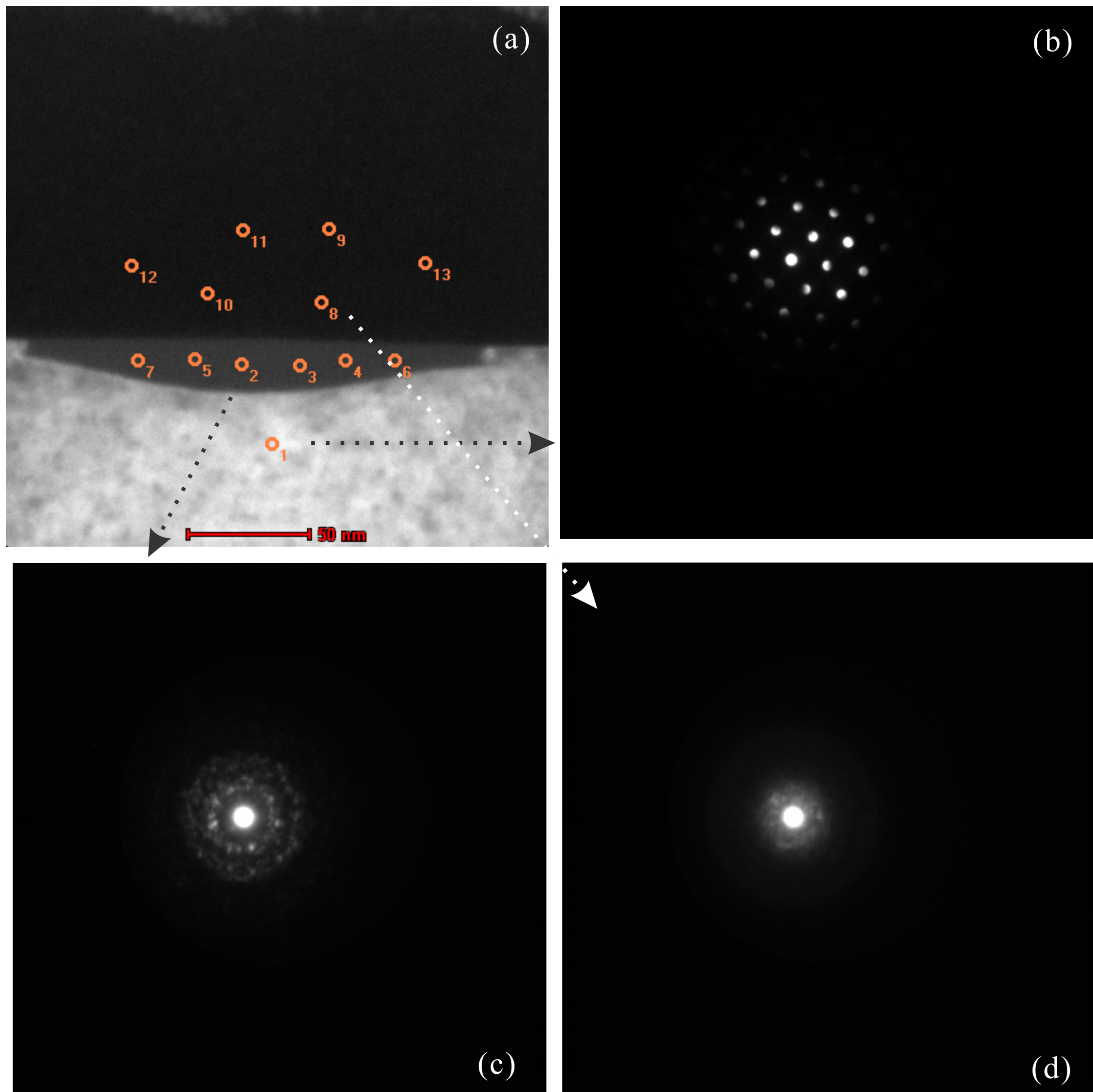

Figure 34: Electron diffraction patterns (EDPs) of different sampling spots around the ripple produced with laser pulses at $\lambda = 400$ nm. (a) TEM image of the ripple being sampled by the electron diffraction beams; (b) EDP of the crystalline Si substrate (corresponding to the sampling mark of O_1); (c) EDP of the nano-crystalline ripple (corresponding to the sampling mark of O_2); (d) EDP of the amorphous SiO_2 (corresponding to the sampling mark of O_8).

dark-field TEM image with indications of the sampling areas for the EDX spectra is shown in Figure 35 (a). The EDX spectra of the ripple and the Si substrate seem to be identical in which only the distinctive silicon peak stands out. In comparison, apart from the silicon peak, the oxygen peak can be clearly viewed in the EDX spectrum of the SiO_2 layer. As a result, regardless of the change in the laser wavelength, such as at $\lambda = 400$ nm or 800 nm, the ripples produced by femtosecond laser pulse irradiations are composed of pure silicon. As the TEM specimen is mounted on a copper sample holder, the copper peaks are present in all the EDX spectra.

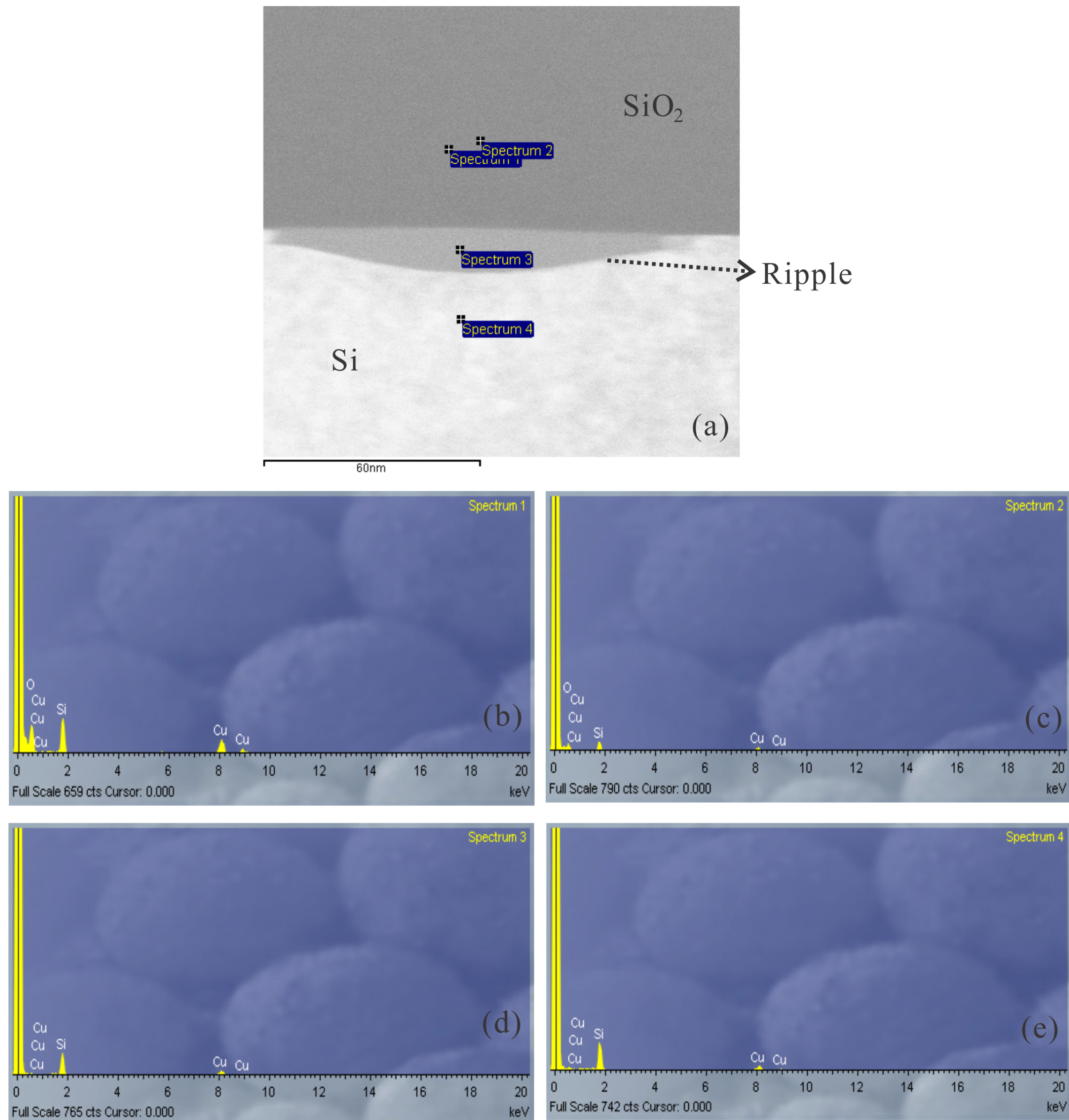

Figure 35: EDX spectra of different regions near one of the ripples on the same FIB specimen shown in Figure 31. (a) Dark-field TEM image of one of the ripples. The specific locations where the EDX spectra are acquired are marked with spectrum numbers. Different material compositions are also explicitly labelled.; (b) and (c) EDX spectrum of the SiO_2 layer; (d) EDX spectrum of the sampled ripple; (e) EDX spectrum of the Si substrate.

5.2.3 Effects of incident laser energy

Figure 36 shows how the ripples evolve as the incident laser energy drops from 0.161 μJ to 0.091 μJ when irradiating at $\lambda = 400$ nm. Other than the difference in the laser energy, other experimental parameters are identical for all the sites. They have an intact 112 nm thick oxide layer, and were translated at a speed of 1000 μm/s in the x-direction. At a higher laser energy, the ripples appear to be washed-out in their central regions, but gradually become more prominent at the edges. Once the laser energy is lowered to a certain point, such as 0.129 μJ, the ripples converge all the way through. Eventually, when the power is too low for producing ripples, the ripples fade away entirely, and only slight discolouration can be visible on the sample surface, as shown in Figure 36 (f).

For the 112 nm thick oxide sample that was translated along the x-direction, the spatial periodicity of the ripples is measured to be roughly 350 nm, regardless of changes in the laser energies and the translation speeds. It is about 12 % larger than the ripple period of 311 nm for the 158 nm thick oxide sample. The ripples on the oxide sample with an oxide thickness of 112 nm are slightly more slanted. As indicated in Figure 36, the laser fluence window for creating continuous ripples on the 112 nm thick oxide sample is within the range of 42 and 60 mJ/cm^2 or less. In comparison, this range is within 34 and 44 mJ/cm^2 for the 158 nm oxide sample. It can be concluded that the oxide thickness plays a role in determining the amount of laser energy required for producing ripples at $\lambda = 400$ nm, which is consistent with the case of at $\lambda = 800$ nm. The small dots on the SEM images are likely due to the external contaminants existing prior to the laser irradiation, and bigger white rods might be due to imaging artifacts.

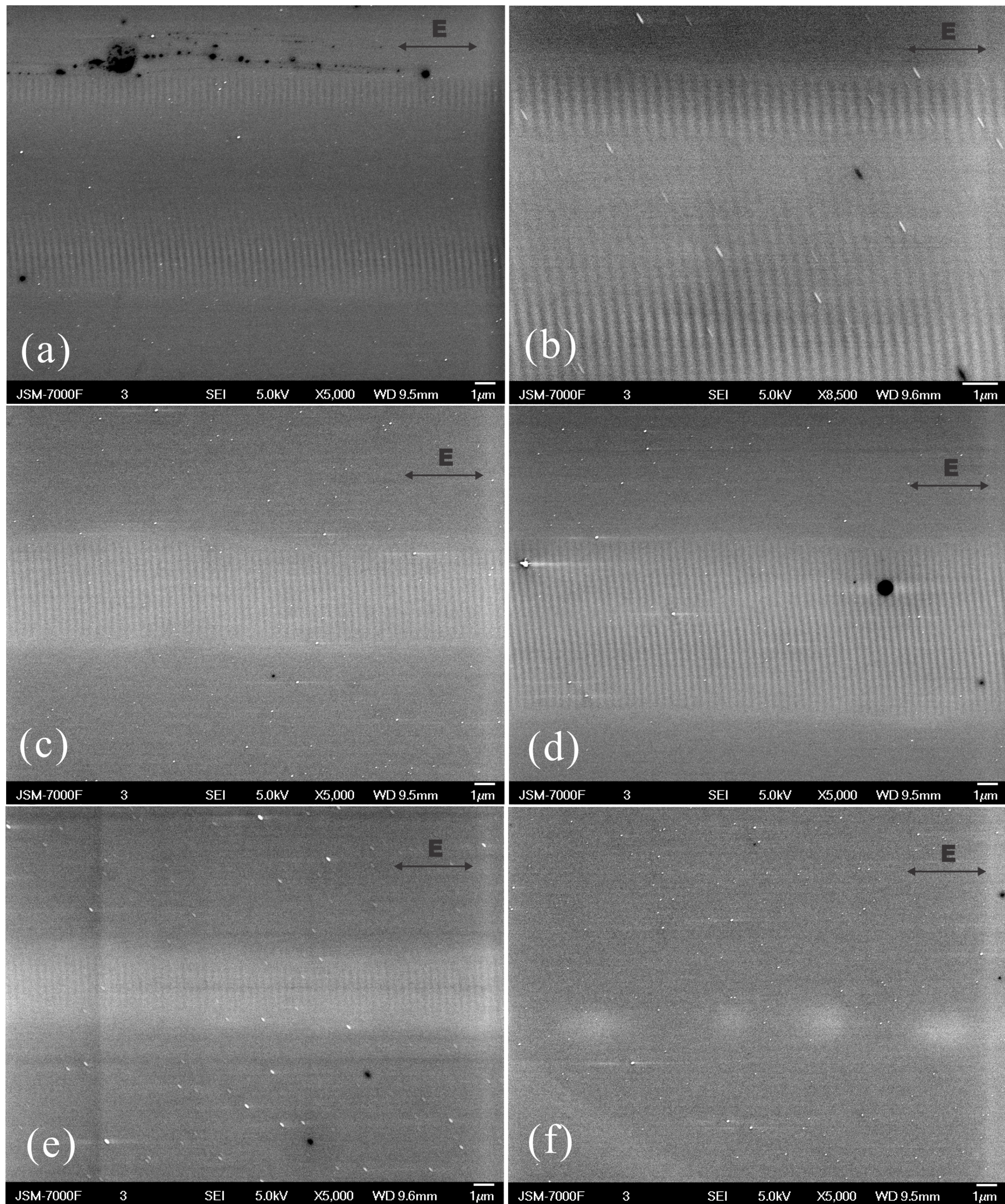

Figure 36: SEM images demonstrating the ripple evolution as a function of the incident laser energy at λ = 400 nm. The 112 nm SiO_2-Si sample was translated at a speed of 1000 μm/s in the x-direction. (a) 0.161 μJ (71 mJ/cm^2); (b) 0.146 μJ (65 mJ/cm^2); (c) 0.129 μJ (57 mJ/cm^2); (d) 0.106 μJ (47 mJ/cm^2); (e) 0.095 μJ (42 mJ/cm^2); (f) 0.090 μJ (40 mJ/cm^2). Note: the magnifications are different.

5.2.4 Effects of translation speed

Figure 37 demonstrates how the ripple formation changes as a function of the translation speed varying from 2000, 1000 to 500 μm/s. The three specimens are all from the 112 nm oxide sample that was translated along the x-direction. They have an identical incident laser energy of 0.135 μJ (60 mJ/cm^2). At 2000 μm/s, there are no ripples present, indicating that the number of effective shots, (i.e. 15) at this speed is too few to create any ripples. Once the speed is reduced to 1000 μm/s with exactly twice the number of effective shots, the regular ripples can be formed even when the sample was irradiated with the same amount of laser power. The ripples continue to form at a slower speed of 500 μm/s. The black dots are due to external contaminants, e.g. dust existing on the sample surfaces.

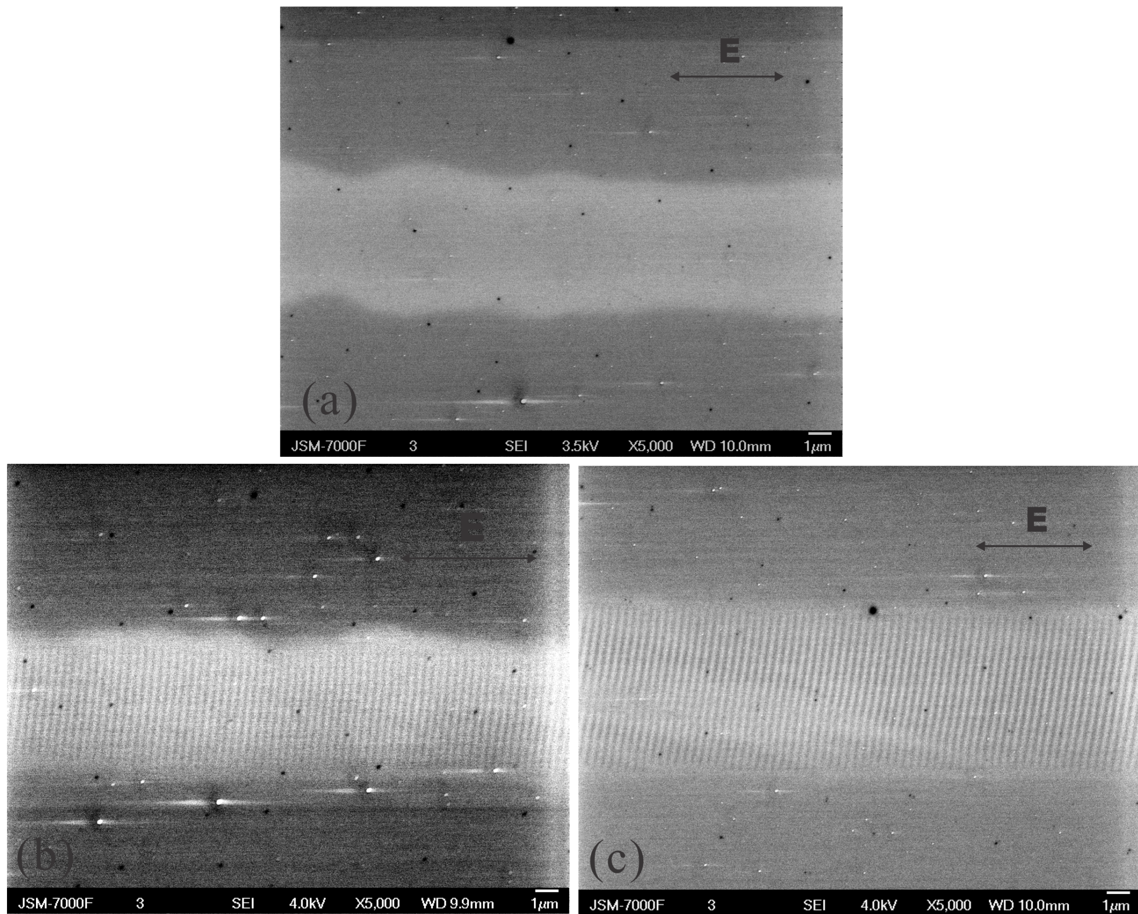

Figure 37: SEM images demonstrating the ripple evolution as a function of the translation speed at λ = 400 nm. (a) At 2000 μm/s; (b) at 1000 μm/s; (c) 500 μm/s. The oxide thickness is 112 nm. The three sites have the same incident laser energy of 0.135 μJ (60 mJ/cm^2) and the same translation direction, i.e. along the x-direction. Note: the black dots are due to external contaminants, e.g. dust existing on the sample surfaces prior to laser processing.

5.2.5 Effects of cutting direction

A typical outcome in terms of ripple formation when the oxide samples were translated in the y-direction is shown in Figure 38. The specimens are selected from the SiO_2-Si sample with an oxide thickness of 112 nm. The general development of the ripples for the y-direction transition can be inferred and described based on the SEM images shown in Figure 38. When the translation speeds are as high as 2000 and 1000 μm/s, no ripples can be produced on all the SiO_2-Si samples within the laser power range that was used in the experiments. By comparing with the results from the x-direction translation, it can be concluded that there does not exist a laser fluence window for the y-direction transition that can produce well-structured ripples at high translation speeds. As the translation speed goes down to 500 μm/s, the ripples start to form, but appear with mixed orientations. The well-behaved ripples appeared at 100 μm/s. They look fairly similar to the ripples shown in Figure 30, but are oriented at a large angle relative to the polarization of the E-field that is along the x-direction. The ripple periodicity is measured to be approximately 260 nm that is significantly smaller than the formed ripples for the x-direction translation, which is around 310 nm.

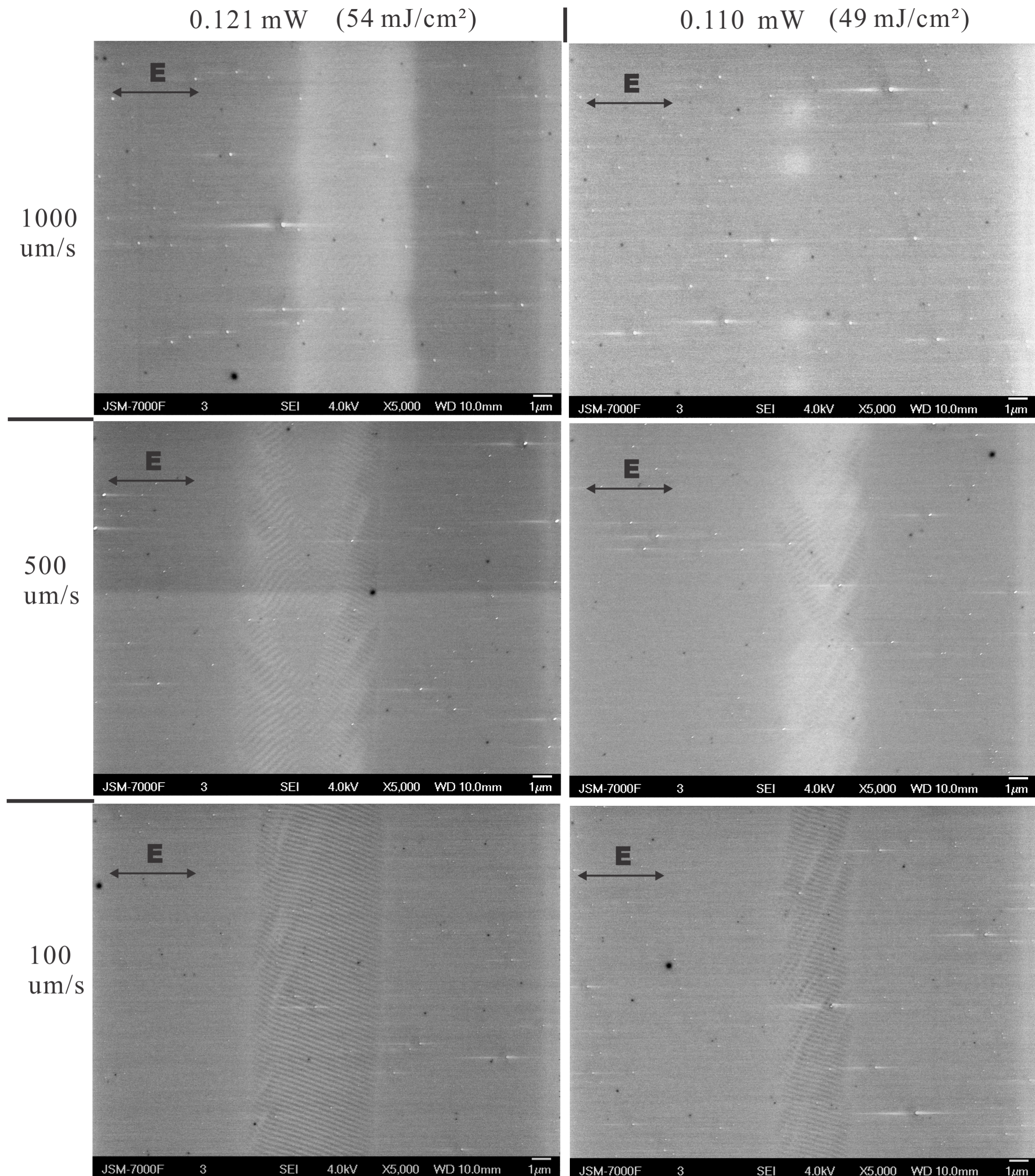

Figure 38: SEM images demonstrating the ripple evolution with variations in both the translation speed and the laser power when the 112 nm thick SiO_2-Si sample was irradiated at $\lambda = 400$ nm and translated along the y-direction.

5.2.6 Comparative results of the ripples between the SiO_2-Si and Si samples at $\lambda = 400$ nm

Typical features produced on a pure Si sample after it was irradiated with femtosecond laser pulses at $\lambda = 400$ nm are demonstrated in Figures 39 and 40. For both translation directions, a general observation can be made that the Si undergoes more modifications, particularly near the center of the Gaussian laser beam, as the laser energy increases. Under a certain proper combination of translation speed and laser energy, some sorts of LIPSS-like features can be created on the Si surface. Compared with the LIPPS produced when translating in the x-direction at $\lambda = 800$ nm, as shown in Figure 28, the orientation of the LIPSS produced at $\lambda = 400$ nm with the same translation direction (i.e. along the x-direction) also seems to be tilted at an angle relative to the polarization of the E-fields.

Compared with the LIPSS formed using $\lambda = 800$ nm laser pulses when translating the Si sample in the y-direction, as shown in Figure 23, the orientation of the LIPSS created at $\lambda = 400$ nm when translating in the y-direction runs along the same direction with a slightly tilted angle as the polarization of the E-field, rather than being perpendicular to it. In addition, the LIPSS that can be viewed in Figure 40 (c) look quite similar to the interface ripples formed at a translation speed of 100 μm/s, which is shown in Figure 38. The spatial periodicity of the LIPSS is evaluated to be roughly 350 nm that is about 36 % greater than the spatial periodicity of the interface ripples (i.e. roughly 260 nm).

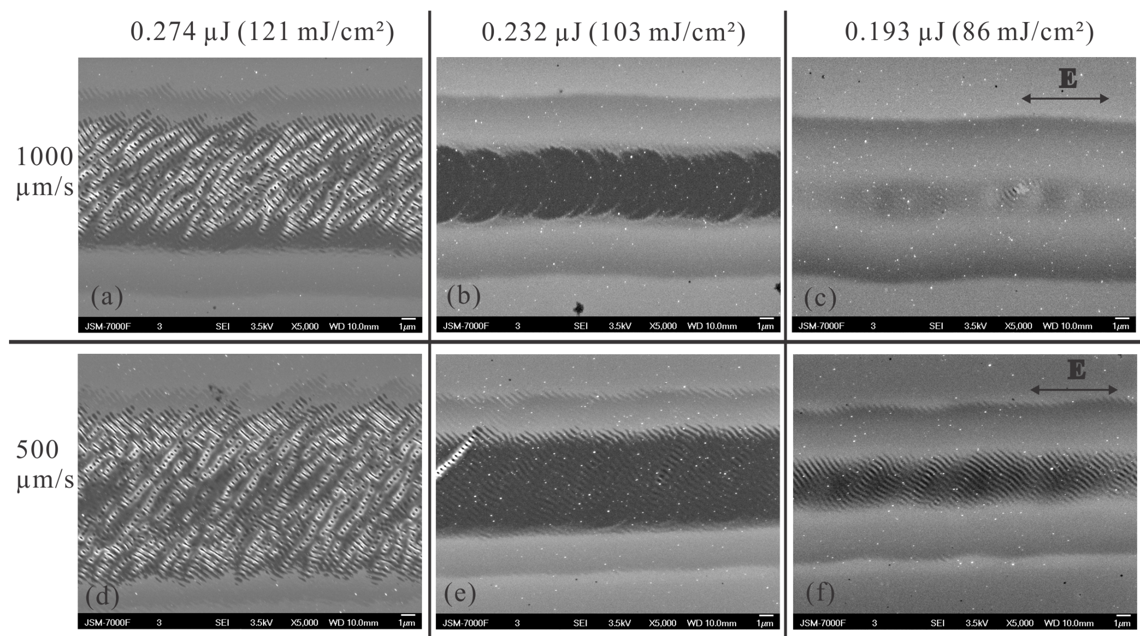

Figure 39: SEM images demonstrating the LIPSS evolution as functions of both the translation speed and laser power for a pure Si sample that was irradiated at $\lambda =$ 400 nm and translated along the x-direction. The black dots are dust on the sample surface prior to laser processing. The white dots might be from the debris produced during the laser irradiation.

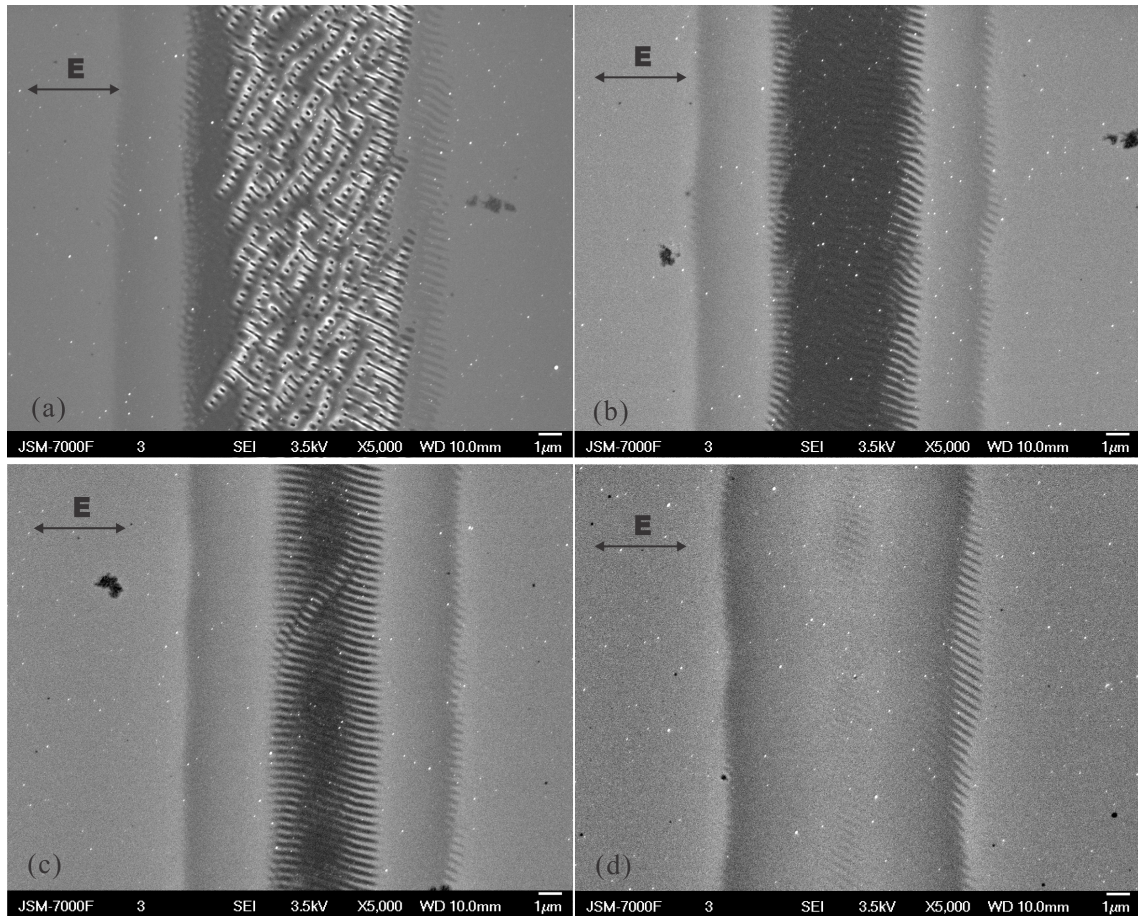

Figure 40: SEM images demonstrating the LIPSS evolution as a function of the laser power when a pure Si sample was irradiated at λ = 400 nm, and translated at a speed of 500 μm/s along the y-direction. (a) 0.232 μJ (103 mJ/cm^2); (b) 0.212 μJ (94 mJ/cm^2); (c) 0.193 μJ (86 mJ/cm^2); (d) 0.177 μJ (78 mJ/cm^2). The black dots are dust on the sample surface prior to laser processing. The white dots might be from the debris produced during the laser irradiation.

5.3 Laser irradiation using picosecond pulses at 800 nm wavelength

5.3.1 Experimental details

To investigate how the pulse duration would affect the ripple formation at the SiO_2-Si interface, a 112 nm thick oxide sample was irradiated using two different pulse durations that were 1.0 ps and 5.0 ps. The same Ti:Sapphire laser system produced a linearly polarized laser beam with a peak wavelength of 800 nm at a repetition rate of 1 kHz. Except for the pulse duration, the rest of experimental conditions were maintained identical to the experiment that was carried out on the 112 nm thick oxide sample irradiated with a pulse of 156 fs time duration

The pulse duration of laser pulses can be changed by adjusting the position of the retro-reflector mirror in the compressor part of the Spitfire. The retro-reflector mirror is installed on a stationary rack, but it can be slid in either the forward or backward direction. For the CPA technique using a pair of gratings, it is known that the pulse compression is an inverse process of the pulse stretching, which employs a complementary grating to introduce negative group velocity dispersion to the laser pulses [75]. The use of the compressor is to attempt to fully restore the original pulse duration of a laser pulse after being reflected by an optical grating in the stretcher [1]. In order to acquire the shortest pulse duration from the Spitfire, there is an optimal distance between the two gratings that must be set [93]. Any deviation from that optimal distance can lead to the imperfect pulse compression, and, thus an increase in the final pulse duration. However, because the mounting rack has a limited length restricting the allowable travelling distance of the retro-reflector mirror, the maximum

pulse duration that can be obtained using this approach is approximately 35 ps.

Two pieces of specimen with similar dimensions were cleaved from the 112 nm oxide wafer. The two samples were placed in the vacuum chamber and processed under a translational motion in both x- and y- cutting directions, separately. Two cutting speeds of 2000 and 1000 μm/s were chosen. As the same 125 mm focusing lens was consistently used in the experiments, the same spot size of 19.5 μm (at $1/e^2$ radius) was assumed and employed to calculate peak fluences. Furthermore, the same effective number of laser shots of 12 and 24 that correspond to the two cutting speeds were also presumed. For the experiment using 1 ps pulse width, the laser energy covered the range from 0.787 μJ (139 mJ/cm^2) to 1.23 μJ (216 mJ/cm^2), whereas the laser energy for the 5-ps pulse width experiment extended over a bit larger range, which is from 0.976 μJ (172 mJ/cm^2) to 1.55 μJ (273 mJ/cm^2).

5.3.2 Results and discussion

Typical results from both 1 ps and 5 ps experiments are shown in Figure 41 and 42, individually. As indicated in the caption, the selection of the entire scope of laser fluences used for four sites on the samples have laser fluences that are in the intermediate range of the entire laser fluence used for the related experiment. The SEM images demonstrate the transitional region between the case when the oxide layer is completely ripped off by the deposited laser energy and the case when the oxide layer is fully intact. Judging from the given images, the oxide layer was partially removed in some random locations where the ripples formed on the Si substrate become easily visible. However, at the regions where the oxide layers still remain intact, discolouration on the sample surface suggests that there are obviously modifications

on the Si substrate, and yet it is hard to distinguish their details looking through the oxide layer. Furthermore, by comparing Figures 41 and 42, there are no significant differences in the outcomes between 1 ps pulse duration and 5 ps pulse duration cases. However, it is worth noticing that it requires larger laser fluences, which are around 40 % more than for the 5 ps laser pulses to create similar sample modifications on the 112 nm oxide sample, compared to the case of 1 ps laser pulses.

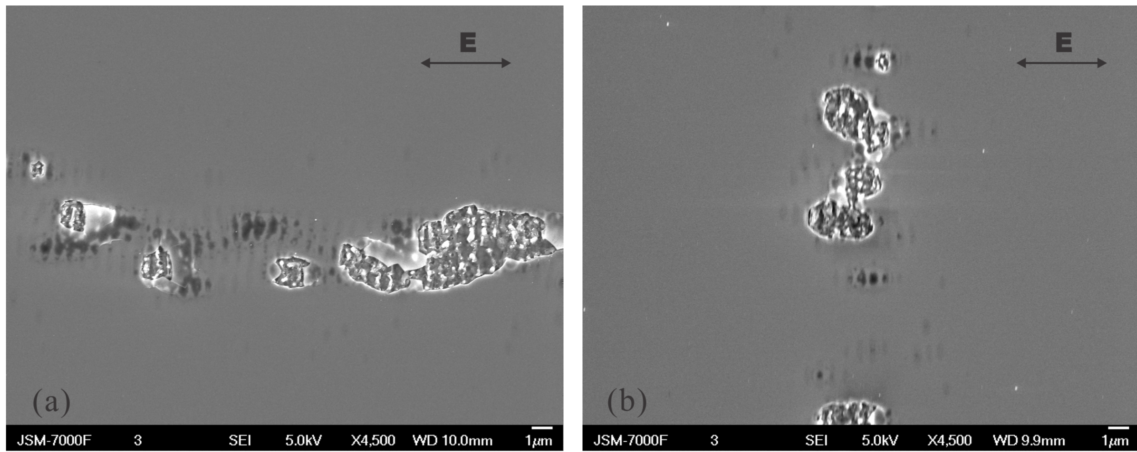

Figure 41: SEM images of typical results for the 112 nm thick oxide sample after being irradiated with 1 ps laser pulses, and at a translation speed of 2000 μm/s. (a) Translating in the x-direction with a laser energy of 0.959 μJ (a peak fluence of 169 mJ/cm^2); (b) translating in the y-direction with a laser energy of 0.939 μJ (a peak fluence of 166 mJ/cm^2). Both sites were irradiated at λ = 800 nm.

The most critical experimental finding from the two picosecond experiments is that there does not exist a laser fluence window that allows the ripples to form at the SiO_2-Si interface while the oxide layer remains fully untouched after laser irradiation. In contrast, for the experiments using the femtosecond laser pulses, such laser fluence windows do exist at both λ = 400 nm and 800 nm. Within the laser fluence range that was employed for the picosecond experiments, the oxide layer was either removed partially in some random spots or completely broken off revealing the ripples created

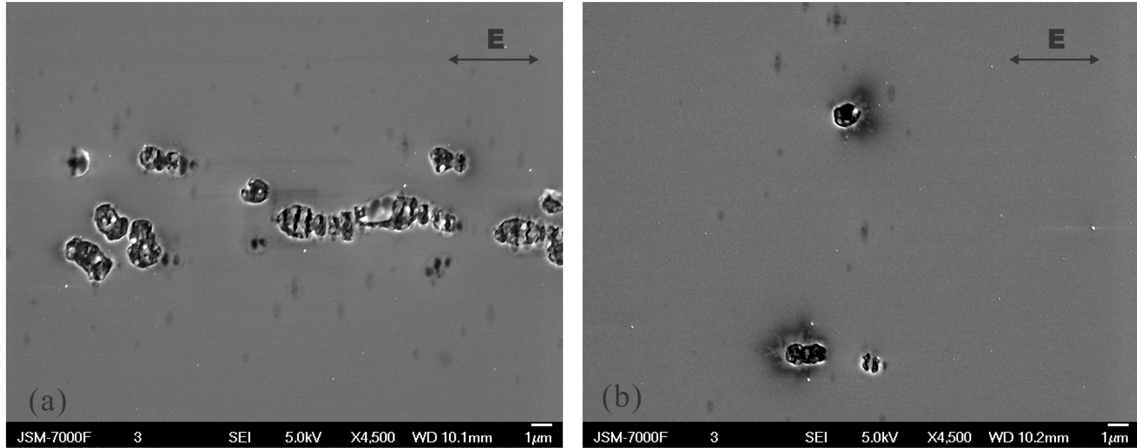

Figure 42: SEM images of typical results for the 112 nm thick oxide sample after being irradiated with 5 ps laser pulses, and at a translation speed of 2000 μm/s. (a) Translating in the x-direction with a laser energy of 1.27 μJ (224 mJ/cm^2); (b) translating in the y-direction with a laser energy of 1.19 μJ (210 mJ/cm^2). Both sites were irradiated at $\lambda = 800$ nm.

on the Si substrate. I did not further explore the experimental parameters in terms of translating speeds and different oxide thicknesses, etc., similar to what have been done for the femtosecond irradiation. Even so, based on the results from both 1 ps and 5 ps experiments, I was convinced that generation of the ripples at the SiO_2-Si interface while preserving the integrity of the oxide layer is an exclusive phenomena for the laser pulse durations within the femtosecond regime.

According to the delamination mechanism suggested and experimentally confirmed through the pump-probe imaging technique by McDonald, et al. [94], removal of the SiO_2 layer results from the relaxation of compressive stress between the thin oxide film and the heat-affected Si layer that absorbs most of incident laser energy. The deposited laser energy causes the Si substrate near the interface to form the electron plasma and subsequent melting of the Si. The SiO_2 layer gets heated and

softened through both direct heat transfer from the molten Si and collisional momentum transfer from the electron plasma. Consequently, it will lead to the deformation and delamination of the SiO_2 layer [17]. Caused by the statistical variations, such as intrinsic defects in the Si substrate, and the initial density of seed electrons for the avalanche ionization, it is known that the formation of the electron plasma created by MPI becomes less predictable and deterministic once the pulse duration enters the picosecond regime [3, 18]. This unpredictable nature of depositing laser energy into materials, to a large extent, would explain the sporadic removal of the oxide layer using picosecond pulses.

Chapter 6

Summary and future work

6.1 Summary

6.1.1 Laser irradiation conditions

Firstly, it has been found that ripples can be produced at the interface of the SiO_2-Si structure after irradiating the SiO_2-Si samples with femtosecond laser pulses in a translational motion fashion. To further learn how the ripple formation evolves with varied irradiation conditions and what might be the optimal situations for creating the ripples, a series of laser experiments were conducted in a very systematic approach. Table 6 summarizes the fixed experimental parameters that were consistently applied to all the experiments. Those parameters can be experimentally adjusted and should be considered for the future work to study their effects on the ripple formation.

In contrast, other more important experimental parameters were the main focus of the research of which their effects on the ripple formation have been extensively investigated. The varying experimental parameters are listed in Table 7. It is proven

that forming well-structured ripples at the SiO_2-Si interface is an intricate phenomena that depends on the laser wavelengths, laser pulse durations, laser peak fluences, translation speeds and translation directions, as well as oxide thicknesses. Therefore, it is very crucial to keep a careful track of accurate experimental conditions that have been considered and might be taken into account for future explorations.

Experimental parameter	**Setting used in this thesis**
Repetition rate of laser pulses	1 kHz
Polarization of the incident E-fields	Linearly-polarized
Spatial intensity shape of the laser beam	Gaussian shape
Angle of incidence	Normal (90 degree)
Sample type	SiO_2-Si and bulk Si samples
Environment	Rough vacuum (40 - 60 mTorr)
Temperature	Room temperature (21 - 24 °C)

Table 6: Summary of the fixed experimental parameters employed in the laser experiments

6.1.2 General material characterization of the ripples

Initially, it was observed that there were ripples formed on the SiO_2-Si sample with an oxide thickness of 216 nm after the sample was processed under laser irradiation. However, simply judging from the image contrast of the acquired OM and SEM images for the ripples, it lacked of convincing evidence to support the conclusion that the ripples are created at the SiO_2-Si interface. After removing the oxide layer using HF solution, the detailed structures of the ripples were revealed, which indicated that the ripples are produced on the Si substrate, not in the oxide layer. In these cases, the

Experimental parameter	Values used in this thesis
Laser wavelength at peak	400 nm, and 800 nm (fundamental)
Spot size of the laser beam ($1/e^2$ radius)	4.4 μm and 17-19μm
Pulse duration	141 fs - 198 fs, 1.0 ps and 5.0 ps
Laser energy range	0.6 - 1.4 μJ (for λ = 800 nm); 0.03 - 0.2 μJ (for λ = 400 nm)
Translation speed (μm/s)	2000, 1000, 500, and 100
Translation direction	x-axis and y-axis
Number of consecutive passes on a track	1, 5, 10, 20, 40, 50, 60, and 80
SiO_2 thickness (nm)	24, 112, 117, 150, 216 and 1013

Table 7: Summary of the varying experimental parameters applied in the laser experiments to study their effects on the ripple formation.

oxide layer remained fully intact after laser irradiation.

Based on the AFM measurements of the sample surfaces, in the cases of samples with an intact oxide layer and without the oxide layer, it can be concluded that the presence of the oxide layer inhibits the outward extension of the ripples formed on the Si substrate. Although most of the laser energy is absorbed and deposited into the Si substrate, the oxide layer does have a role in confining the propagation of thermal energy by exerting mechanical restoring forces to the molten Si, particularly at the interface of the SiO_2-Si and Si [16, 68]. In addition, the cross-sectional view of the ripples through TEM micrographies confirmed that the Si surfaces are periodically modified. The depth of modulation is approximately 78 nm below the SiO_2-Si interface for the ripples produced at $\lambda = 800$ nm, whereas the value is reduced dramatically to roughly 22 nm for the ripples created at $\lambda = 400$ nm. According to the results from the HRTEM and EDX analysis, as well as the EDP patterns, the ripples are composed of nano-crystalline Si whose crystalline dimensions are on the

order of a few nanometers. Despite the fact that the molten Si did cause some very subtle deformation to the oxide layer adjacent to the Si substrate, the oxide layer still maintained its overall integrity with respect to its mechanical structure and material composition.

6.1.3 Effects of different irradiation conditions on the ripple formation

The most direct impact on the ripple formation, especially in terms of its spatial periodicity and overall features, is recognized as the change in the laser wavelength. For oxide samples irradiated using ultrashort laser pulses at $\lambda = 800$ nm, the spatial periodicity of the ripples is within the range between 510 - 705 nm, that is within 65% - 88% of the peak laser wavelength. Additionally, when irradiating oxide samples with ultrashort laser pulses at $\lambda = 400$ nm, the ripple periods are reduced to the range of 310 - 350 nm, that is within 78% - 88% of the peak laser wavelength.

Apart from affecting the ripple periods, the laser wavelength also has an impact on the extent of material modifications in the silicon substrate. For the ripples formed at $\lambda = 800$ nm, the effects of many nano-explosions are observed to spread along the ripples. It seems that they are inevitably generated once the ripples are formed at this wavelength, regardless of variations in other experimental parameters, such as laser fluences, and oxide thicknesses. However, for the ripples produced at $\lambda = 400$ nm, the effects of nano-explosions are not observable in the SEM images either because they can not be created at this shorter wavelength or because they are too small to be detected under SEM. Further removal of the oxide layers using the HF etching method for the oxide samples processed at $\lambda = 400$ nm should be able to provide key

information about revealing the existence of the nano-explosions.

The oxide thicknesses also affect the spatial periodicity of the interface ripples, which is true for ripples created at both λ = 400 nm and 800 nm. Based on the measurements from the cases of λ = 400 nm and 800 nm, it seems that as the oxide thickness increases, the ripple period is somehow decreased. The only exception is from the oxide sample with an oxide thickness of 216 nm, which was irradiated at λ = 800 nm. Its ripple period turned out be around 700 nm, which is larger than the ripple periods of oxide samples with oxide thicknesses of 112 nm and 1013 nm.

In addition, the oxide thickness plays a role in determining the threshold fluence that is required to create the ripples at the interface. For oxide samples irradiated at λ = 800 nm, it is noticed that an increase in the oxide thickness leads to a reduction in the threshold fluence for initiating the ripple generation. Because oxide samples with a only slight difference in the oxide thicknesses (112 nm and 150 nm) were irradiated at λ = 400 nm, the change in the threshold fluence caused by the varying oxide thickness is not significant enough to draw the same conclusion as for the case of λ = 800 nm.

It is found that the structure of the ripples is highly dependent on the incident laser fluence, the translation direction, and the translation speed (i.e. the number of effective laser shots on a given location). If other experimental conditions are fixed, e.g. oxide thicknesses and laser wavelengths, the well-structured ripples can only be produced when the oxide samples are translated along the x-direction (i.e. parallel to the polarization of the E-fields) under strict conditions consisting of a narrow “window” of laser fluence at a proper translation speed. From an engineering point of view, it may forecast a technical obstacle if fabricating the ripples in mass

production for practical applications.

6.2 Suggestions for future work

6.2.1 Extensive work on post-analysis of the irradiated oxide samples

HF etching could be done to the oxide samples that were irradiated with femtosecond laser pulses at λ = 400 nm, as well as to the samples that were irradiated with picosecond laser pulses. By removing the oxide layer, the detailed appearance of the ripples can be readily observed under SEM. Just like what has been done on the samples processed at λ = 800 nm, the unetched and etched samples irradiated at λ = 400 nm could also be examined through the AFM measurements in order to find out the morphological characteristics of the sample surfaces.

A TEM specimen from the SiO_2-Si sample with an intact oxide thickness of 150 nm after being processed at λ = 400 nm has been obtained by Julia Huang using the FIB technique. Although preliminary TEM and EDX analysis for that specimen have been carried out, thorough examinations are needed to extract more detailed information about the characteristics of the ripples formed at λ = 400 nm. Moreover, further comparisons between the cases of λ = 800 nm and 400 nm with respect to their TEM results also require immediate attentions.

6.2.2 Further exploration on the laser irradiation conditions

In this research, all the experiments were carried out at λ = 400 nm and 800 nm whose photon energies are greater than the band-gap energy of Si (1.1 eV) [21]. It

would be a very valuable direction to pursue for the laser wavelengths that have photon energies lower than 1.1 eV. The optical parametric amplifier (OPA) system available in the lab could be utilized to achieve this goal. The OPA (Spectra-Physics OPA-800) can produce two output laser beam with tuneable wavelengths: signal and idler beams. The optimal laser wavelengths for the signal beam and the idler beam are approximately at 1300 and 2100 nm, respectively. It is known that the absorption depth of Si at $\lambda = 1300$ nm is around 4.5×10^{-5} cm^{-1}, which is significantly larger than the value of 8.5×10^{2} cm^{-1} at $\lambda = 800$ nm, as well as than the value of 9.5×10^{4} cm^{-1} at $\lambda = 400$ nm [74]. It would be interesting to see if ripples or other unexpected features may be produced at the SiO_2-Si interface upon irradiating with sub-bandgap wavelengths.

As mentioned in the Appendix A, I built a setup with a heating stage that is properly incorporated with the micromachining vacuum chamber for Eugene Hsu's projects. The setup has the ability to raise the sample temperature up to 500 °C. Considering the fruitful results from Eugene Hsu's projects, particularly in terms of the ripple formation on the bulk Si at elevated temperatures [12], irradiating the oxide samples with increased sample temperatures would provide a new perspective toward understanding the underlying mechanisms of forming ripples at the SiO_2-Si interface. Because many optical and thermal material properties have a temperature-dependence, particularly the absorption coefficient [95] of Si, the difference in the linear absorption coefficient between Si and SiO_2-Si [96], in addition to the thermal conductivity [97], I suspect that there would be valuable outcomes resulting from processing the oxide samples at an elevated temperature.

6.2.3 Applications to various layered samples

In this research, only one type of a layered system, that is the SiO_2 on Si, was considered. However, the experimental framework could be applied to a variety of layered systems with different combinations of oxide layers and semiconductor materials. Among them, owing to its rapidly increasing applications in the current technology, particularly in the area of photonic-integrated circuit, the silicon-on-oxide (SOI) sample would be the most interesting system to work on. In addition, considering the accessible techniques of depositing different oxide layers on a silicon substrate which are offered from Dr. Peter Mascher's research facility, the silicon-dioxide layer can readily replaced with the silicon oxynitride. This kind of novel layered system would be also an interesting direction to pursue.

6.2.4 Theoretical study of the ripple formation for layered structures

It would be really beneficial to have a better understanding in the underlying physical mechanisms for elucidating the ripple formation at the interface of a layered system. This thesis is mainly focused on the experimental aspect. Even though many important findings have been attained and verified based on the experimental results, it would be compelling to support them with theoretical corroborations. Achieving this goal will call for a rigorous theoretical investigation on the ripple formation mechanisms, particularly regarding the role of the oxide layer upon laser irradiation. Additionally, as a possible starting point, I suspect that the existing theories of elucidating the LIPSS formation mechanisms, such as Sipe-SPPs theory [39, 42, 43, 50–52] and SHG theory [59, 61, 66], may be revised for a layered system, instead of a bulk

material.

Appendix A

Academic contributions

A.1 Contributions to collaborative projects

I was a key contributor in building a setup with a heating stage from its initial design, prototyping, and to the final testing and implementation. The setup played a critical role in achieving the experimental goals of two of Eugene Hsu's Ph.D projects. The details of the setup and its schematic diagram, in addition to its specific functions in the projects can be referred to in the Chapter 3 and 5 of Eugene Hsu's Ph.D thesis [12].

I was involved in utilizing an integrating sphere to characterize textured silicon samples in Eugene Hsu's other Ph.D project. I designed several different sample holders in order to allow the Si samples to properly fit in the ports of the integrating sphere. I also conducted a few independent measurements using the integrating sphere to figure out the optical properties of textured silicon samples, such as their absorption and reflection.

A.2 Conference poster

- **B. Liu**, E.M. Hsu, G.A. Botton, A.P. Knights, J.S. Preston, and H.K. Haugen, *Studies of ultrafast laser interaction with SiO_2-Si samples*, 8th International conference on photo-excited processes and applications, Rochester, USA, 2012.
- **B. Liu**, E.M. Hsu, G.A. Botton, A.P. Knights, J.S. Preston, and H.K. Haugen, *Studies of ultrafast laser interaction with SiO_2-Si samples*, submitted to the 12th International Conference on Laser Ablation (COLA), Ischia, Italy, 2013.

Bibliography

[1] J.-C. Diels and W. Rudolph, *Ultrashort laser pulse phenomena,*. Academic Press, 2006.

[2] S. Backus, C. G. Durfee, M. M. Murnane, and H. C. Kapteyn, "High power ultrafast lasers," *AIP, Review of Scientific Instruments*, vol. 69, no. 3, pp. 1207–1223, 1998.

[3] X. Liu, D. Du, and G. Mourou, "Laser ablation and micromachining with ultrashort laser pulses," *IEEE Journal of Quantum Electronics*, vol. 33, no. 10, pp. 1706–1716, 1997.

[4] R. Osellame, H. J. W. M. Hoekstra, G. Cerullo, and M. Pollnau, "Femtosecond laser microstructuring: an enabling tool for optofluidic lab-on-chips," *Laser Photonics Reviews*, vol. 5, no. 3, pp. 442–463, 2011.

[5] P. R. Miller, R. Aggarwal, A. Doraiswamy, Y. J. Lin, Y.-S. Lee, and R. J. Narayan, "Laser micromachining for biomedical applications," *JOM Journal of the Minerals, Metals and Materials Society*, vol. 61, no. 9, pp. 35–40, 2009.

[6] D. von der Linde, K. Sokolowski-Tinten, and J. Bialkowski, "Laser-solid interaction in the femtosecond time regime," *Applied Surface Science*, vol. 109-110, pp. 1–10, 1997.

[7] B. N. Chichkov, C. Momma, S. Nolte, F. Von Alvensleben, and A. Tunnermann, "Femtosecond, picosecond and nanosecond laser ablation of solids," *Applied Physics A: Materials Science Processing*, vol. 63, no. 2, pp. 109–115, 1996.

[8] J. D. Plummer, M. D. Deal, and P. B. Griffin, *Silicon VLSI technology: fundamentals, practice and modeling*, vol. 4. Prentice Hall Upper Saddle River, NJ, 2000.

[9] J. M. Bustillo, R. T. Howe, and R. S. Muller, "Surface micromachining for microelectromechanical systems," *Proceedings of the IEEE*, vol. 86, no. 8, pp. 1552–1574, 1998.

[10] T. Dullweber, S. Gatz, H. Hannebauer, T. Falcon, R. Hesse, J. Schmidt, and R. Brendel, "19.4 percent efficient large area rear-passivated screen-printed silicon solar cells," *Proc. 26th EU PVSEC Hamburg*, pp. 811–816, 2011.

[11] S. Wenham, J. Zhao, X. Dai, A. Wang, and M. Green, "Surface passivation in high efficiency silicon solar cells," *Solar Energy Materials and Solar Cells*, vol. 65, no. 1, pp. 377–384, 2001.

[12] E. Hsu, "Ultrashort-pulse laser ablation of silicon toward device applications," *McMaster Univeristy, Ph.D thesis*, 2012.

[13] H. van Driel, J. Sipe, and J. Young, "Laser-induced periodic surface structure

on solids: A universal phenomenon," *Physical Review Letters*, vol. 49, no. 26, pp. 1955–1958, 1982.

[14] S. Hermann, N.-P. Harder, R. Brendel, D. Herzog, and H. Haferkamp, "Picosecond laser ablation of SiO2 layers on silicon substrates," *Applied Physics A*, vol. 99, no. 1, pp. 151–158, 2009.

[15] X. Y. Chen, Y. F. Lu, B. J. Cho, Y. P. Zeng, J. N. Zeng, and Y. H. Wu, "Pattern-induced ripple structures at silicon-oxide/silicon interface by excimer laser irradiation," *Applied Physics Letters*, vol. 81, no. 7, p. 1344, 2002.

[16] Y. F. Lu, W. K. Choi, Y. Aoyagi, A. Kinomura, and K. Fujii, "Controllable laser-induced periodic structures at silicon-dioxide/silicon interface by excimer laser irradiation," *Journal of Applied Physics*, vol. 80, no. 12, p. 7052, 1996.

[17] J. P. McDonald, V. R. Mistry, K. E. Ray, and S. M. Yalisove, "Femtosecond pulsed laser direct write production of nano- and microfluidic channels," *Applied Physics Letters*, vol. 88, no. 18, p. 183113, 2006.

[18] C. B. Schaffer, A. Brodeur, and E. Mazur, "Laser-induced breakdown and damage in bulk transparent materials induced by tightly focused femtosecond laser pulses," *Measurement Science and Technology*, vol. 12, no. IEE, pp. 1784–94, 2001.

[19] S. K. Sundaram and E. Mazur, "Inducing and probing non-thermal transitions in semiconductors using femtosecond laser pulses," *Nature Materials*, vol. 1, pp. 217–224, 2002.

[20] M. D. Feit, A. M. Komashko, and A. M. Rubenchik, "Ultra-short pulse laser interaction with transparent dielectrics," *Applied Physics A*, vol. 79, no. 7, 2004.

[21] B. G. Streetman and S. Banerjee, *Solid state electronic devices*, vol. 2. Prentice-Hall Englewood Cliffs, NJ, 1995.

[22] L. Jiang and H. Tsai, "Femtosecond laser ablation: challenges and opportunities," in *Proceeding of NSF Workshop on Research Needs in Thermal, Aspects of Material Removal, Stillwater, OK*, pp. 163–177, 2003.

[23] S. K. Lai, "Interface trap generation in silicon dioxide when electrons are captured by trapped holes," *Journal of Applied Physics*, vol. 54, no. 5, p. 2540, 1983.

[24] S. S. Mao, F. Qur, S. Guizard, X. Mao, R. E. Russo, G. Petite, and P. Martin, "Dynamics of femtosecond laser interactions with dielectrics," *Applied Physics A*, vol. 79, no. 7, pp. 1695–1709, 2004.

[25] B. Wu and Y. C. Shin, "A simplified predictive model for high-fluence ultra-short pulsed laser ablation of semiconductors and dielectrics," *Applied Surface Science*, vol. 255, no. 1.The Institution of Engineering and Technology, pp. 4996–5002, 2009.

[26] L. Keldysh, "Ionization in the field of a strong electromagnetic wave," *Zh. Eksperim. i Teor. Fiz.*, vol. 47, 1964.

[27] F. Qur, S. Guizard, and P. Martin, "Time-resolved study of laser-induced breakdown in dielectrics," *Europhys. Lett*, vol. 56, no. 1, pp. 138–144, 2001.

[28] E. G. Gamaly, A. V. Rode, and B. Luther-Davies, "Ablation of solids by femtosecond lasers: Ablation mechanism and ablation thresholds for metals and dielectrics," *Physics of Plasmas*, vol. 9, no. 3, 2002.

[29] S. H. B. C. Stuart and M. D. Perry, "Chirped-pulse amplification in Ti:Sapphire beyond 1 pm," *IEEE Journal of Quantum Electronics*, vol. 31, no. 3, 1995.

[30] B. C. Stuart, M. D. Feit, S. Herman, A. M. Rubenchik, B. W. Shore, and M. D. Perry, "Nanosecond-to-femtosecond laser-induced breakdown in dielectrics," *Physical Review B*, vol. 53, no. 4, pp. 1749–1761, 1996.

[31] Y. Siegal, E. Glezer, L. Huang, and E. Mazur, "Laser-induced phase transitions in semiconductors," *Annual Review of Materials Science*, vol. 25, no. 1, pp. 223–247, 1995.

[32] J. A. Kash, J. C. Tsang, and J. M. Hvam, "Subpicosecond time-resolved raman spectroscopy of LO phonons in GaAs," *Physical Review Letters*, vol. 54, no. 19, pp. 2151–2154, 1985.

[33] A. Ben-Yakar, A. Harkin, J. Ashmore, R. L. Byer, and H. A. Stone, "Thermal and fluid processes of a thin melt zone during femtosecond laser ablation of glass: the formation of rims by single laser pulses," *Journal of Physics D: Applied Physics*, vol. 40, no. 5, pp. 1447–1459, 2007.

[34] R. F. W. Herrmann, J. Gerlach, and E. E. B. Campbell, "Ultrashort pulse laser ablation of silicon: An MD simulation study," *Applied Physics A: Materials Science and Processing*, vol. 66, Compendex, pp. 35–42, 1998.

[35] E. Leveugle, D. S. Ivanov, and L. V. Zhigilei, "Photomechanical spallation of molecular and metal targets: molecular dynamics study," *Applied Physics A (Materials Science Processing)*, vol. A79, no. IEE, pp. 1643–55, 2004.

[36] D. Perez and L. J. Lewis, "Molecular-dynamics study of ablation of solids under femtosecond laser pulses," *Physical Review B (Condensed Matter and Materials Physics)*, vol. 67, no. 1, pp. 184102–1, 2003.

[37] B. Rethfeld, K. Sokolowski-Tinten, D. von der Linde, and S. I. Anisimov, "Timescales in the response of materials to femtosecond laser excitation," *Applied Physics A*, vol. 79, no. 4-6, pp. 767–769, 2004.

[38] M. Birnbaum, "Semiconductor surface damage produced by ruby lasers," *Journal of Applied Physics*, vol. 36, no. 11, p. 3688, 1965.

[39] J. E. Sipe, J. F. Young, J. S. Preston, and H. M. van Driel, "Laser-induced periodic surface structure I. Theory," *Physical Review B*, vol. 27, no. 2, pp. 1141–1154, 1983.

[40] A. Borowiec and H. K. Haugen, "Subwavelength ripple formation on the surfaces of compound semiconductors irradiated with femtosecond laser pulses," *Applied Physics Letters*, vol. 82, no. 25, pp. 4462–4464, 2003.

[41] D. Emmony, R. Howson, and L. Willis, "Laser mirror damage in germanium at 10.6 micrometer," *Applied Physics Letters*, vol. 23, no. 11, pp. 598–600, 1973.

[42] J. F. Young, "Laser-induced periodic surface damage and radiation remnants," *Applied Physics Letters*, vol. 41, no. 3, p. 261, 1982.

[43] J. Young, J. Sipe, and H. van Driel, "Laser-induced periodic surface structure. III. Fluence regimes, the role of feedback, and details of the induced topography in germanium," *Physical Review B*, vol. 30, no. 4, pp. 2001–2015, 1984.

[44] B. Tan and K. Venkatakrishnan, "A femtosecond laser-induced periodical surface structure on crystalline silicon," *Journal of Micromechanics and Microengineering*, vol. 16, no. 3, The Institution of Engineering and Technology, pp. 1080–5, 2006.

[45] A. Dalili, T. Bo, and K. Venkatakrishnan, "Silicon wafer surface patterning using femtosecond laser irradiation below ablation threshold," *Optics and Lasers in Engineering*, vol. 48, no. 3, The Institution of Engineering and Technology, pp. 346–53, 2010.

[46] Z. Guosheng, P. Fauchet, and A. Siegman, "Growth of spontaneous periodic surface structures on solids during laser illumination," *Physical Review B*, vol. 26, no. 10, pp. 5366–5381, 1982.

[47] J. Skolski, G. Romer, V. Mitko, J. Obona, V. Ocelik, and J. Hosson, "Modeling of laser induced periodic surface structures," *Journal of Laser Micro-Nanoengineering*, vol. 5, no. 3, 2010.

[48] J. Bonse, M. Munz, and H. Sturm, "Structure formation on the surface of indium phosphide irradiated by femtosecond laser pulses," *Journal of Applied Physics*, vol. 97, no. IEE, pp. 13538–1, 2005.

[49] J. Bonse, A. Rosenfeld, and J. Kruger, "On the role of surface plasmon polaritons in the formation of laser-induced periodic surface structures upon irradiation of

silicon by femtosecond-laser pulses," *Journal of Applied Physics*, vol. 106, no. 10, p. 104910, 2009.

[50] M. Huang, F. Zhao, Y. Cheng, N. Xu, and Z. Xu, "Origin of laser-induced near-subwavelength ripples: Interference between surface plasmons and incident laser," *ACS Nano*, vol. 3, no. 12, pp. 4062–4070, 2009.

[51] J. Wang and C. Guo, "Formation of extraordinarily uniform periodic structures on metals induced by femtosecond laser pulses," *Journal of Applied Physics*, vol. 100, no. 2, pp. 023511–023511–4, 2006.

[52] H. Raether, *Surface plasmons*. Springer-Verlag Berlin, 1988.

[53] G. Miyaji and K. Miyazaki, "Origin of periodicity in nanostructuring on thin film surfaces ablated with femtosecond laser pulses," *Opt. Express*, vol. 16, no. 20, pp. 16265–16271, 2008.

[54] G. A. Martsinovskii, G. D. Shandybina, D. S. Smirnov, S. V. Zabotnov, L. A. Golovan, V. Y. Timoshenko, and P. K. Kashkarov, "Ultrashort excitations of surface polaritons and waveguide modes in semiconductors," *Optics and Spectroscopy*, vol. 105, no. 1, pp. 67–72, 2008.

[55] F. Garrelie, J. Colombier, F. Pigeon, S. Tonchev, N. Faure, M. Bounhalli, S. Reynaud, and O. Parriaux, "Evidence of surface plasmon resonance in ultrafast laser-induced ripples," *Opt. Express*, vol. 19, no. 10, pp. 9035–9043, 2011.

[56] L. Qi, K. Nishii, and Y. Namba, "Regular subwavelength surface structures induced by femtosecond laser pulses on stainless steel," *Optics letters*, vol. 34, no. 12, pp. 1846–1848, 2009.

[57] J.-W. Yao, C.-Y. Zhang, H.-Y. Liu, Q.-F. Dai, L.-J. Wu, S. Lan, A. V. Gopal, V. A. Trofimov, and T. M. Lysak, "High spatial frequency periodic structures induced on metal surface by femtosecond laser pulses," *Opt. Express*, vol. 20, no. 2, pp. 905–911, 2012.

[58] L. Ran, Z. Guo, and S. Qu, "Self-organized periodic surface structures on ZnO induced by femtosecond laser," *Applied Physics A*, vol. 100, no. 2, pp. 517–521, 2010.

[59] T. Jia, H. Chen, M. Huang, F. Zhao, J. Qiu, R. Li, Z. Xu, X. He, J. Zhang, and H. Kuroda, "Formation of nanogratings on the surface of a ZnSe crystal irradiated by femtosecond laser pulses," *Physical Review B*, vol. 72, no. 12, 2005.

[60] X. D. Guo, R. X. Li, Y. Hang, Z. Z. Xu, B. K. Yu, Y. Dai, B. Lu, and X. W. Sun, "Coherent linking of periodic nano-ripples on a ZnO crystal surface induced by femtosecond laser pulses," *Applied Physics A*, vol. 94, no. 2, pp. 423–426, 2008.

[61] R. Le Harzic, D. Dorr, D. Sauer, M. Neumeier, M. Epple, H. Zimmermann, and F. Stracke, "Large-area, uniform, high-spatial-frequency ripples generated on silicon using a nanojoule-femtosecond laser at high repetition rate," *Opt. Lett.*, vol. 36, no. 2, pp. 229–231, 2011.

[62] B. Kumar and R. K. Soni, "Submicrometre periodic surface structures in InP induced by nanosecond UV laser pulses," *Journal of Physics D: Applied Physics*, vol. 41, no. 15, 2008.

[63] J. Reif, F. Costache, O. Varlamova, G. Jia, and M. Ratzke, "Self-organized

regular surface patterning by pulsed laser ablation," *Physica Status Solidi c*, vol. 6, no. 3, pp. 681–686, 2009.

[64] T. Tomita, K. Kinoshita, S. Matsuo, and S. Hashimoto, "Effect of surface roughening on femtosecond laser-induced ripple structures," *Applied Physics Letters*, vol. 90, no. 15, p. 153115, 2007.

[65] Y. Yuan, L. Jiang, X. Li, C. Wang, H. Xiao, Y. Lu, and H. Tsai, "Formation mechanisms of sub-wavelength ripples during femtosecond laser pulse train processing of dielectrics," *Journal of Physics D: Applied Physics*, vol. 45, no. 17, p. 175301, 2012.

[66] R. Le Harzic, D. Dorr, D. Sauer, F. Stracke, and H. Zimmermann, "Generation of high spatial frequency ripples on silicon under ultrashort laser pulses irradiation," *Applied Physics Letters*, vol. 98, no. 21, p. 211905, 2011.

[67] S. K. Das, D. Dufft, A. Rosenfeld, J. Bonse, M. Bock, and R. Grunwald, "Femtosecond-laser-induced quasiperiodic nanostructures on TiO2 surfaces," *Journal of Applied Physics*, vol. 105, no. 8, p. 084912, 2009.

[68] Y. Lu, J. Yu, and W. Choi, "Theoretical analysis of laser-induced periodic structures at silicon-dioxide/silicon and silicon-dioxide/aluminum interfaces," *Applied Physics Letters*, vol. 71, no. 23, pp. 3439–3440, 1997.

[69] J. Bonse, J. M. Wrobel, J. Kruger, and W. Kautek, "Ultrashort-pulse laser ablation of indium phosphide in air," *Applied Physics A (Materials Science Processing)*, vol. A72, no. IEE, pp. 89–94, 2001.

[70] T. Rublack, M. Muchow, S. Hartnauer, and G. Seifert, "Laser ablation of silicon dioxide on silicon using femtosecond near infrared laser pulses," *Energy Procedia*, vol. 8, pp. 467–472, 2011.

[71] T. Rublack, S. Hartnauer, P. Kappe, C. Swiatkowski, and G. Seifert, "Selective ablation of thin SiO2 layers on silicon substrates by femto and picosecond laser pulses," *Applied Physics A*, vol. 103, no. 1, pp. 43–50, 2011.

[72] T. Rublack and G. Seifert, "Femtosecond laser delamination of thin transparent layers from semiconducting substrates," *Opt. Mater. Express*, vol. 1, pp. 543–550, 2011.

[73] T. Rublack, M. Schade, M. Muchow, H. S. Leipner, and G. Seifert, "Proof of damage-free selective removal of thin dielectric coatings on silicon wafers by irradiation with femtosecond laser pulses," *Journal of Applied Physics*, vol. 112, no. 2, p. 023521, 2012.

[74] M. A. Green and M. J. Keevers, "Optical properties of intrinsic silicon at 300 K," *Progress in Photovoltaics: Research and Applications*, vol. 3, no. 3, pp. 189–192, 1995.

[75] M. Pessot, J. Squier, G. Mourou, and D. J. Harter, "Chirped-pulse amplification of 100-fsec pulses," *Optics Letters*, vol. 14, no. 15, pp. 797–799, 1989.

[76] C. Barty, T. Guo, C. Le Blanc, F. Raksi, C. Rose-Petruck, J. Squier, K. Wilson, V. Yakovlev, and K. Yamakawa, "Generation of 18-fs, multiterawatt pulses by regenerative pulse shaping and chirped-pulse amplification," *Optics Letters*, vol. 21, no. 9, pp. 668–670, 1996.

[77] K. Yamakawa, M. Aoyama, S. Matsuoka, H. Takuma, C. Barty, and D. Fittinghoff, "Generation of 16-fs, 10-TW pulses at a 10-Hz repetition rate with efficient Ti:sapphire amplifiers," *Optics Letters*, vol. 23, no. 7, pp. 525–527, 1998.

[78] D. Strickland and G. Mourou, "Compression of amplified chirped optical pulse," *Opt. Commun. 56, 219.*, 1985.

[79] S. Gavrilov, D. Golishnikov, V. Gordienko, A. Savel'Ev, and R. Volkov, "Efficient hard x-ray source using femtosecond plasma at solid targets with a modified surface," *Laser and Particle Beams-Pulse Power and High Energy Densities*, vol. 22, no. 3, pp. 301–306, 2004.

[80] C. G. Serbanescu, J. A. Chakera, and R. Fedosejevs, "Efficient Ka x-ray source from submillijoule femtosecond laser pulses operated at kilohertz repetition rate," *Review of Scientific Instruments*, vol. 78, no. 10, p. 103502, 2007.

[81] J. Yu, Z. Jiang, J. C. Kieffer, and A. Krol, "Hard x-ray emission in high intensity femtosecond laserctarget interaction," *Physics of Plasmas*, vol. 6, no. 4, p. 1318, 1999.

[82] B. Prade, J. Schins, E. Nibbering, M. A. Franco, and A. Mysyrowicz, "A simple method for the determination of the intensity and phase of ultrashort optical pulses," *Optics Communications*, vol. 113, no. 1, pp. 79–84, 1994.

[83] J.-C. M. Diels, J. J. Fontaine, I. C. McMichael, and F. Simoni, "Control and measurement of ultrashort pulse shapes (in amplitude and phase) with femtosecond accuracy," *Applied Optics*, vol. 24, no. 9, pp. 1270–1282, 1985.

[84] C. Yan and J.-C. Diels, "Amplitude and phase recording of ultrashort pulses," *J. Opt. Soc. Am. B*, vol. 8, no. 6, p. 1259, 1991.

[85] J. Peatross and A. Rundquist, "Temporal decorrelation of short laser pulses," *JOSA B*, vol. 15, no. 1, pp. 216–222, 1998.

[86] T. Watanabe and I. Ohdomari, "A kinetic equation for thermal oxidation of silicon replacing the Deal-Grove equation," *Journal of the Electrochemical Society*, vol. 154, no. 12, pp. G270–G276, 2007.

[87] E. Dassau, B. Grosman, and D. R. Lewin, "Modeling and temperature control of rapid thermal processing," *Computers and chemical engineering*, vol. 30, no. 4, pp. 686–697, 2006.

[88] E. Meyer, "Atomic force microscopy," *Progress in surface science*, vol. 41, no. 1, pp. 3–49, 1992.

[89] F. J. Giessibl, "Advances in atomic force microscopy," *Reviews of Modern Physics*, vol. 75, no. 3, p. 949, 2003.

[90] S. Ram, E. S. Ward, and R. J. Ober, "Beyond Rayleigh's criterion: A resolution measure with application to single-molecule microscopy," *Proceedings of the National Academy of Sciences of the United States of America*, vol. 103, no. 12, pp. 4457–4462, 2006.

[91] J. Liu, "Simple technique for measurements of pulsed gaussian-beam spot sizes," *Optics Letters*, vol. 7, no. 5, pp. 196–198, 1982.

[92] T. H. R. Crawford, A. Borowiec, and H. K. Haugen, "Femtosecond laser micromachining of grooves in silicon with 800 nm pulses," *Applied Physics A*, vol. 80, no. 8, pp. 1717–1724, 2005.

[93] M. Pessot, J. Squier, P. Bado, G. Mourou, and D. J. Harter, "Chirped pulse amplification of 300 fs pulses in an alexandrite regenerative amplifier," *Quantum Electronics, IEEE Journal of*, vol. 25, no. 1, pp. 61–66, 1989.

[94] J. P. McDonald, J. A. Nees, and S. M. Yalisove, "Pump-probe imaging of femtosecond pulsed laser ablation of silicon with thermally grown oxide films," *Journal of Applied Physics*, vol. 102, no. 6, p. 063109, 2007.

[95] G. Jellison and F. Modine, "Optical absorption of silicon between 1.6 and 4.7 eV at elevated temperatures," *Applied Physics Letters*, vol. 41, no. 2, pp. 180–182, 1982.

[96] H. Tada, A. E. Kumpel, R. E. Lathrop, J. B. Slanina, P. Nieva, P. Zavracky, I. N. Miaoulis, and P. Y. Wong, "Thermal expansion coefficient of polycrystalline silicon and silicon dioxide thin films at high temperatures," *Journal of Applied Physics*, vol. 87, no. 9, pp. 4189–4193, 2000.

[97] H. R. Shanks, P. D. Maycock, P. H. Sidles, and G. C. Danielson, "Thermal conductivity of silicon from 300 to 1400 K," *Physical Review*, vol. 130, no. 5, pp. 1743–1748, 1963.